LNGS P26/2000
CERN/SPSC 2000-031
SPSC/M657
August 15, 2000

Proposal

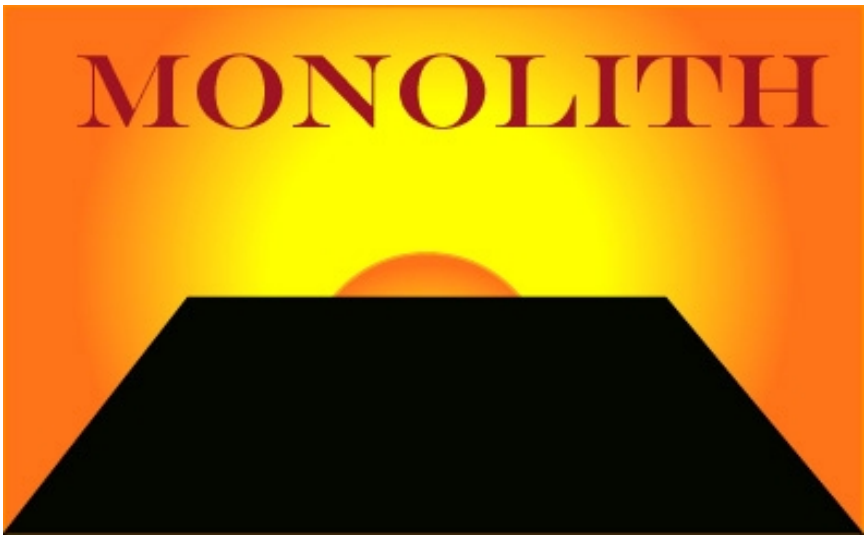

A Massive Magnetized Iron Detector for Neutrino Oscillation Studies

The MONOLITH Collaboration[§]

(**M**assive **O**bservatory for **N**eutrino **O**scillations or **LI**mits on **TH**eir existence)

N.Y. Agafonova[1] M. Ambrosio[2] M. Amelchakov[3] P. Antonioli[4] E. Aprile[5] V. Aynutdinov[3] C. Ballhausen[6] G. Bari[4] R. Benaceur[7] G. Bencivenni[8] L. Bergamasco[9,10] G. Bologna[8,9] M. Bonesini[11] G. Bruni[4] N. Bruski[12] F.W. Büsser[6] D. Chernov[3] N. Cicchetti[4] O. Cremonesi[11] A. Curioni[5] D. Frekers[12] P. Galeotti[9,10] A. Garfagnini[6] A. Geiser[6] F. Gharbi[7] D. Giugni[11] P. Giusti[4] V.I. Gurentsov[1] C. Gustavino[13] O. Gutsche[6] G. Heinzelmann[6] K. Hoepfner[6] T. Kellmann[12] V. Kindin[3] R. Klanner[6] B. Koppitz[6] R. Kokoulin[3] K. Kompaniets[3] A. Konovalov[3] A. Kovzelev[1] J. Kückmann[12] A.S. Malgin[1] G. Mannocchi[8,14] A. Margotti[4] R. Maschuw[15] H. Menghetti[4] P. Monacelli[‡,16,13] O. Morra[10,14] F. Murtas[8] G.P. Murtas[8] R. Nania[4] B. Naroska[6] P. Negri[11] M. Paganoni[11] A. Pesci[4] L. Periale[10,14] V. Peskov[17] A. Petrukhin[3] P. Picchi[8,14,9] A. Pullia[11] O.G. Ryazhskaya[1] S. Ragazzi[*,11] N. Redaelli[11] F. Ronga[8] G. Sartorelli[4] L. Satta[8,18] W. Schmidt-Parzefall[6] M. Selvi[4] C. Souga[7] T. Tabarelli de Fatis[11] F. Terranova[11] A. Trabelsi[7] G. Trinchero[10,14] R. van Staa[6] B. Villone[14] K. Winter[19] V.F. Yakushev[1] E. Yanson[3] I. Yashin[3]

[§] subject to final approval by the respective institutions and funding agencies

[*] spokesperson [‡] Gran Sasso contact person

---

[1]Institute for Nuclear Research (INR), Moscow, Russia

[2]INFN, Sezione di Napoli, Napoli, Italy

[3]Moscow Engineering Physics Insitute, Moscow, Russia

[4]Bologna University and INFN, Bologna, Italy

[5]Physics Department and Columbia Astrophysics Laboratory, Columbia University, New York, NY 10027, USA

[6]Hamburg University, Hamburg, Germany

[7]Laboratoire de Physique Nucléaire et de Physique des Particules, Faculté des Sciences de Tunis, Tunis, Tunisia

[8]Laboratori Nazionali di Frascati and INFN, Frascati, Italy

[9]University of Torino, Torino, Italy

[10]INFN Sezione di Torino, Torino, Italy

[11]Dipartimento di Fisica, Università di Milano Bicocca and INFN, Milano, Italy

[12]Münster University, Münster, Germany

[13]Laboratori Nazionali di Gran Sasso and INFN, Assergi, Italy

[14]Istituto di Cosmogeofisica, CNR, Torino, Italy

[15]Bonn University, Bonn, Germany

[16]Physics Department University of L'Aquila and INFN, L'Aquila, Italy

[17]Physics Department in Frescati, Royal Institute of Technology, Stockholm, Sweden

[18]Rome University, Rome, Italy

[19]Humboldt University Berlin, Berlin, Germany

This is an open Collaboration and other groups are being invited to join

Groups that have already expressed their interest in this Proposal

M. Chmeissani[20] E. Fernandez[20] C. Rolfs[21]

[20] Universitat Autonoma de Barcelona and IFAE, Barcelona, Spain
[21] Bochum University, Bochum, Germany

In addition to the INR group listed in the author list, members of the INR NOMAD group are also interested in this Proposal.

Abstract

MONOLITH is a proposed massive (34 kt) magnetized tracking calorimeter at the Gran Sasso laboratory in Italy, optimized for the detection of atmospheric muon neutrinos. The main goal is to establish (or reject) the neutrino oscillation hypothesis through an explicit observation of the full first oscillation swing. The Δm^2 sensitivity range for this measurement comfortably covers the complete Super-Kamiokande allowed region. Other measurements include studies of matter effects, the NC up/down ratio, the $\bar{\nu}/\nu$ ratio, the study of cosmic ray muons in the multi-TeV range, and auxiliary measurements from the CERN to Gran Sasso neutrino beam. Depending on approval, data taking with part of the detector could start towards the end of 2004.

Contents

Chapter 1

Introduction

1.1 Executive Summary

The question whether neutrinos are massive, and hence the question of the existence of neutrino oscillations, is currently one of the main unsettled challenges in physics. All experiments measuring the flux of solar neutrinos observe a deficit compared to the prediction of solar models [4]. The ratio of muon to electron events observed in atmospheric neutrino interactions is measured by most experiments to be less than expected from models of cosmic ray interactions in the atmosphere [5]. The measurement of the up/down asymmetry of this ratio by the Super-Kamiokande collaboration [6] is generally considered to be the strongest evidence for neutrino oscillations so far. Furthermore, possible oscillation signals in the $\bar{\nu}_\mu - \bar{\nu}_e$ and $\nu_\mu - \nu_e$ channels were observed by the LSND experiment [7]. Finally, massive neutrinos could play an important role in the missing dark matter problem [8] if at least one mass eigenstate lies in the eV range. All these observations make the study of neutrino oscillations a very worthwhile endeavor.

While the cumulative evidence for neutrino oscillations is very striking, a definitive proof that the observed anomalies are actually due to neutrino oscillations is still missing. In particular, the current observations of atmospheric neutrinos are all consistent with the hypothesis of maximal ν_μ oscillations, but do not yet exclude some alternative unconventional explanations [9, 10, 11, 12].

The main physics goal of the MONOLITH experiment is to establish the occurrence of neutrino oscillations in atmospheric neutrinos through the explicit observation of the full first oscillation swing in ν_μ disappearance [13], and to investigate and presumably exclude alternative explanations. This also yields a significantly improved measurement of the oscillation parameters with respect to previous measurements. The experimental design, a massive iron calorimeter, has been inspired by earlier detector studies [14, 15]. The strong magnetic field, adopted in the detector design to extend the sensitivity to the full parameter range allowed by current experiments, is a novel feature among atmospheric neutrino detectors. The charge and momentum measurement of muons from charged current (CC) events also allows unique systematic studies of the atmospheric neutrino flux, and the search for potential matter effects in neutrino oscillations. The measurement of the oscillation pattern can be usefully supplemented by measurements in the CERN to Gran Sasso neutrino beam.

Provided that the neutrino oscillation hypothesis is confirmed, another goal of the experiment is to further investigate the nature of these oscillations. Depending on the oscillation parameters, oscillations into active (ν_τ) or sterile (ν_s) neutrinos can be distinguished through their different effects on the up/down ratio of neutral current (NC)-like events, and/or through the presence or absence of matter effects yielding a distortion of the observed oscillation pattern as a function of energy and/or muon charge. Particularly large effects can be expected in the case of hybrid solutions [16] with significant but non-maximal contributions from sterile neutri-

nos. A particularly interesting option in the context of the standard 3-neutrino scenario would be the measurement of the sign of Δm^2 via an MSW resonance in $\nu_\mu - \nu_e$ oscillations, along the same line as currently studied for Neutrino Factory beams [17].

Due to its ability of in situ measurement of the energy of every muon in the multi-TeV range, MONOLITH will also be a unique facility for pioneer investigations of cosmic ray muons in the unexplored 100 TeV energy region. The results of these studies should give information which is relevant for the solution of the problem of the knee in the cosmic ray energy spectrum.

For this experiment we have designed a detector which has been optimized for the detection of atmospheric neutrinos (with additional substantial sensitivity to the neutrino beam from CERN) and can achieve these physics goals. While the detector has somewhat evolved with respect to our earlier baseline design [1], its main features and performance remain the same. Part of the progress has already been documented in refs. [2, 3].

This document is intended as a physics proposal which points out the physics case and the feasibility of the detector. It is meant as a basis for the project to be accepted in view of proceeding with the final technical detector studies, Additional collaborators are welcome to join. Based on these studies, a full technical design report is foreseen by the end of 2001. If promptly approved, a first part of the detector could be operational by the end of 2004. The physics results discussed in the following chapters correspond to a 4 years exposure of the full detector.

1.2 Historical overview

In 1997 P. Picchi and F. Pietropaolo [18] pointed out that a method based on the upward/downward ratio of atmospheric ν_μ flux could yield a precise measurement of Δm^2, almost insensitive to the precise knowledge of the flux, provided that an adequate resolution on L/E was obtained. They remarked that the adequate resolution had to be provided by a detector

"able to reconstruct energy and direction of the interacting neutrino both for contained and for partially contained events".

They also remarked that the sensitivity of the method would increase for decreasing values of Δm^2, thus providing a search for oscillations complementary to the search performed with long baseline beams.

In a subsequent paper [13] it was shown how appropriate selection criteria could be applied to obtain the required L/E resolution with detectors providing tracking capability, muon momentum measurement and coarse measurement of hadronic energy. A first design of a dedicated detector, of 30 kton mass, was reported in ref. [14].

On November 3rd, 1998, a joint meeting of the SPS and LNGS Scientific Committees was held, where several Letters of Intent were presented. Two of them concerned experiments on atmospheric neutrinos using combined tracking and calorimetric techniques [14, 15]. In one [14] an experiment dedicated to atmospheric neutrinos was proposed. The experimental goals were the detection of the oscillation pattern in ν_μ disappearance, following the method and techniques outlined in ref. [18, 14], and the discrimination between $\nu_\mu - \nu_\tau$ and $\nu_\mu - \nu_s$ oscillations. In the other letter [15] an experiment combining disappearance measurements on atmospheric neutrinos and on a long baseline beam was proposed. The experimental set-up combined a fine grain calorimeter with a magnetic spectrometer.

A combined programme of an experiment on atmospheric neutrinos with a tau-appearance experiment on a long baseline beam was encouraged by the Committees. In particular, the following goal was envisaged [19]:

"An independent check of neutrino oscillation with a massive atmospheric neutrino experiment having a good resolution in neutrino angle and energy. Such a detector would be sensitive to the mass range 2×10^{-4} *to* 5×10^{-3} eV^2*."*

In January 1999 a joint meeting of people interested in the atmospheric neutrino programme was held to compare the different ideas and identify possible common strategies. Working groups were formed in March 1999 with the aim to identify the physics items, the detector techniques for active elements, and a detector design optimized to exploit the high energy component of the atmospheric neutrino flux.

The main achievements of these studies were discussed in the MONOLITH Progress Report [1].

In particular, the detector concept of ref. [14] was extended in order to make it sensitive to the full parameter range allowed by current experiments. This was essentially achieved through the addition of a strong magnetic field, a novel feature among atmospheric neutrino detectors.

As we shall discuss in Chapter 4 (see figure 4.6), a magnetization of 1.3 T of the detector produces a relevant increase of efficiency for medium-low values of L/E. The efficiency is increased by 50% at $L/E = 5 \times 10^2$ and by 100% at $L/E = 2.2 \times 10^2$ km/GeV. This L/E range corresponds to the position of the first oscillation minimum according to most recent Super-Kamiokande reports. The magnetization of the detector is thus expected to increase the efficiency by more than a factor two over the first semiperiod of the oscillation. The detection of the oscillation minimum and the precision on Δm^2 mainly rely on statistics in this region. The cost specific to magnetization of the detector is below 10% of the total cost (see Chapter 8).

In the Progress Report two options were considered for sensitive elements: GSC (glass RPCs) and scintillator bars read out by optical fibers. Two options for the detector layout were also considered: one with horizontal plates and one with only vertical plates. They both yielded similar performances. The horizontal plates option was considered as a baseline reference design. In fact it turned out to be technically easier to realize, and more robust on the rejection of background from downward going cosmic ray muons.

The MONOLITH Progress Report was received as a Letter of Intent by the LNGS Scientific Committee in August 1999. The Committee was

"... favourably impressed by the progress of the Collaboration"

and wished

"... to reemphasize the role of an atmospheric neutrino experiment in the low Δm^2 *region".*

Most of the progress since then has been stimulated by our interactions with the LNGS Scientific Committee, in particular with the referees appointed by the Committee, and with the referees appointed by the INFN Commissione Scientifica Nazionale II. Part of the progress has already been documented in ref. [2].

In December 1999, the CERN Council approved the construction of a long baseline beam from CERN to Gran Sasso.

As a consequence of this decision some of the groups which contributed to the Progress Report decided to concentrate on the appearance experiment and left the atmospheric working group.

The working group on atmospheric neutrinos has then been re-organized as MONOLITH collaboration, with an executive committee formed by A. Geiser, P. Giusti, G. Mannocchi, P. Monacelli and S. Ragazzi, with S. Ragazzi as Spokesman, G. Mannocchi as Project Leader and P. Monacelli as Contact Person with LNGS. Working groups on simulation and analysis and on physics are convened by T. Tabarelli de Fatis and F. Ronga respectively.

The MONOLITH collaboration took note of the decision of the CERN Council and started a dedicated study of the MONOLITH capabilities to exploit the CNGS beam. Already before this decision, a detector layout, with horizontal planes, having a modular structure and a magnetization scheme with field lines perpendicular to the beam direction had been considered, at variance with the baseline detector design of the Progress Report. The direction of the magnetic field perpendicular to the CNGS beam is very helpful in the reconstruction of beam events. An end-cap of vertical planes has been added to further improve the reconstruction of high-momentum muons.

Further studies led to the finalization of the detector configuration and of physics goals.

GSCs have been chosen as main sensitive elements: they provide a better time response with respect to scintillator bars in the proposed configuration. The time resolution is essential in the reduction of cosmic ray background. A dedicated test combined with a simulation has shown that the resolution of GSCs provide a high rejection of the cosmic background. An outer counter, made of scintillators, provides an additional safety margin and/or results in a relevant increase of the fiducial volume.

The main physics goal of the experiment is the detection of the oscillation pattern in ν_μ disappearance and the consequent precise measurement of Δm^2. This is also the item which benefited of the highest attention since the early detector concepts. The study of ν_μ disappearance is thus the key issue of this Proposal.

The possibility of distinguishing oscillations of ν_μ into ν_τ or sterile neutrino (ν_s) has also had a constant attention over the years. However the variety of scenarios which are introduced by the hypothesis of a mixing with a sterile neutrino complicates predictions on the performance of MONOLITH on this issue. Further improvements are to be expected from a more extensive analysis.

The study of the performance of MONOLITH on the CNGS beam is quite recent. In this case the main future efforts should concentrate on the understanding of beam related systematics. Further studies and the collaboration with experts working on the beam design are envisaged in order to reach conclusive results on this issue.

1.3 Organization of the Proposal

Chapter 2 treats the physics goals and motivation outlined above in more detail. The experimental setup is described in chapter 3. Details of the simulation and analysis strategies are documented in chapter 4, chapters 5 and 6 describe the corresponding expected analysis results, and chapter 7 outlines the measurement technique for high energy cosmic ray studies. Finally, cost estimates and time scales are reviewed in chapter 8, chapter 9 describes the collaboration structure, and chapter 10 summarizes the general conclusions.

Chapter 2

Physics Motivation

2.1 Physics context

Although the cumulative evidence for neutrino oscillations is very striking, the final proof that the observed anomalies are actually due to neutrino oscillations is still outstanding. Moreover, a single coherent picture of neutrino masses and mixings has not emerged yet from the available experimental evidence. A precise determination of mixings and masses in the neutrino sector ("neutrino stoichiometry") is one of the most important topics to be covered by future experiments.

In this context, the main motivation for the design of the MONOLITH experiment is to clarify some of the questions left open by the current and planned atmospheric and long baseline neutrino experiments. The current measurement of the atmospheric neutrino anomaly by Super-Kamiokande [6], supported by other atmospheric neutrino measurements, yields *"evidence for oscillation of atmospheric neutrinos"* [6]. However, the experimental resolution is too poor to clearly resolve the oscillation pattern, such that alternative explanations like neutrino decay [10], the influence of large extra dimensions [11], or potential decoherence effects [12] can not be excluded. Furthermore, while the pure $\nu_\mu \to \nu_e$ oscillation hypothesis is strongly disfavoured both by the atmospheric neutrino data [6] and by the results of the CHOOZ reactor experiment [20], the question whether the main effect is due to $\nu_\mu \to \nu_\tau$ or $\nu_\mu \to \nu_s$ oscillations only just starts to be settled. Here, ν_s is a hypothetical "sterile" neutrino, which is relevant for atmospheric neutrinos in many oscillation models [21] and might be needed to simultaneously explain all known neutrino anomalies. This point will be developed further in section 2.2.3.

Promising new insights are expected from new long baseline neutrino beam programs. K2K [22], the first long baseline accelerator neutrino experiment, started last year in Japan. The sensitivity for ν_μ disappearance expected after 3 years at nominal intensity extends down to between 2 and 3×10^{-3} eV^2 (figure 2.1). First indications [23] of a disappearance signal do not yet yield a conclusive result. With the small envisaged statistics (170 events without oscillations in 5 years), and the small L/E reach, the oscillation pattern is unlikely to get fully resolved.

The construction of the American long baseline programme NUMI [24] started last year. MINOS is a 5.4 kton (3.3 kton fiducial mass) detector dedicated to ν_μ disappearance. The beam is scheduled to be commissioned in the last quarter of 2003, and the detector is planned to be partially operational in 2003, and fully completed in 2004. The Soudan-2 detector [25] will also be running in the NUMI beam, with a mass of less than a kiloton but a very fine granularity.

The expected performance of MINOS for 10 kty is outlined in figure 2.1. The experimental sensitivity reaches 2×10^{-3} eV^2 in Δm^2 with the reference beam ($< E_\nu > \sim$ 17 GeV), and 6×10^{-4} eV^2 with a low energy version of the beam called PH2(low) ($< E_\nu > \sim$ 5 GeV); the corresponding discovery contour (4 σ) goes down to 1×10^{-3} eV^2.

Finally, the CERN neutrino beam to Gran Sasso (CNGS) [29] was approved in december

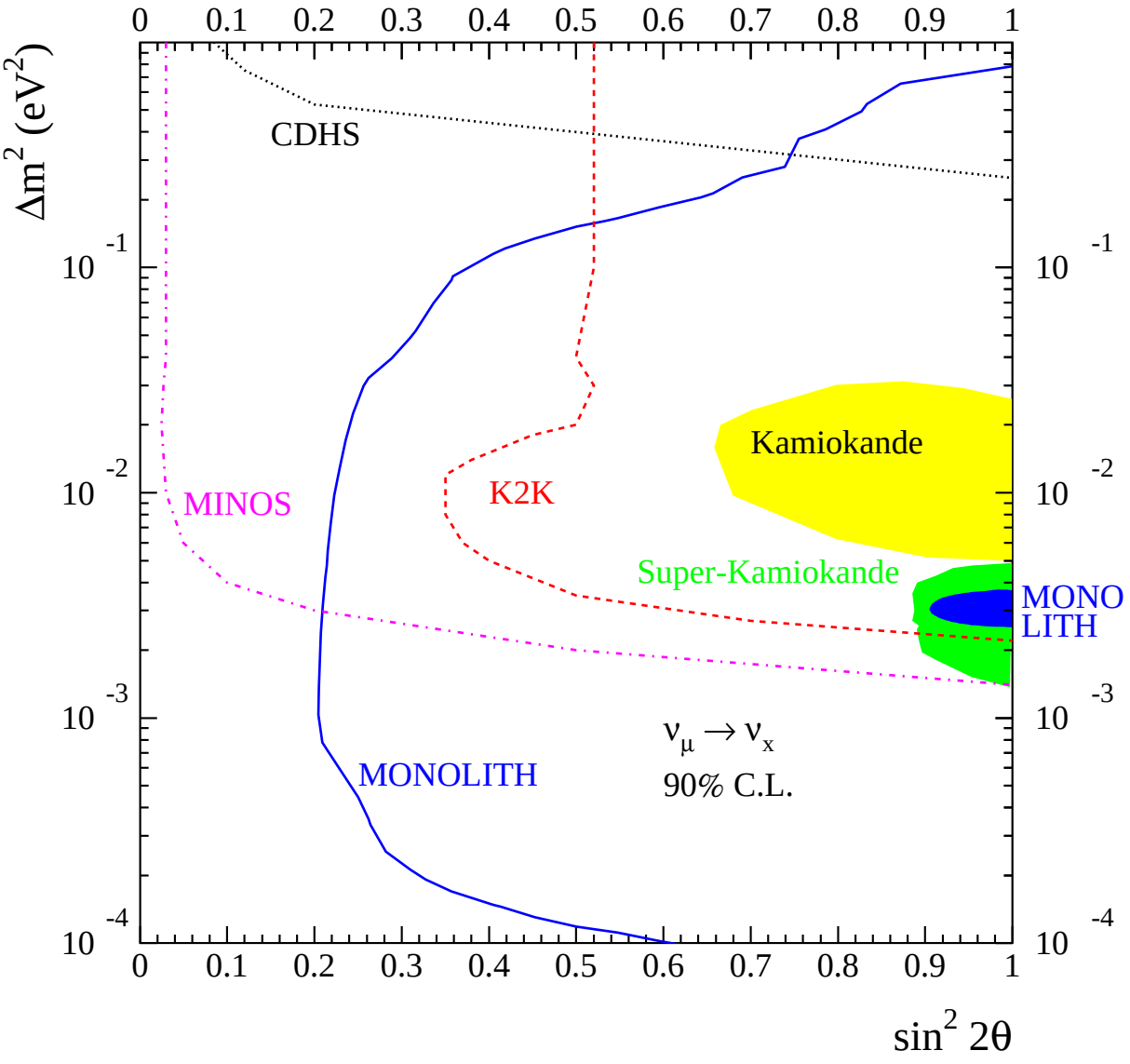

Figure 2.1: Expected sensitivity contours for ν_μ disappearance for K2K [22, 23] (5 years), MINOS [24] (3 years reference beam, for low energy beam see text) and MONOLITH (4 years). Also shown are the exclusion contour from CDHS [26], the recent allowed areas from Super-Kamiokande [27] and Kamiokande [28] and the expected allowed area of MONOLITH for the current Super-Kamiokande central value (4 years).

last year, to become operational in 2005. The main physics goal of the CNGS project is the experimental observation of τ appearance. This could be achieved either directly through the detection of the τ decay kink in nuclear emulsion [30] " à la CHORUS [31]", or indirectly through τ detection using kinematical criteria [32] " à la NOMAD [33]". Furthermore, the expected event rate is small since at L=730 km and E$\sim$15 GeV ν_μ oscillations, which are found to be maximal in atmospheric neutrinos, are not yet fully developed. Combining this with the τ detection threshold, it is impossible to observe an oscillation pattern in ν_τ appearance. The physics issues addressed by MONOLITH are therefore fully complementary to this program. Earlier considerations of this complementarity have led to the suggestion of a detector concept which would combine the two physics programmes [34].

However, beam ν_μ disappearance measurements with MONOLITH can yield a useful complement to the atmospheric neutrino measurements. In the long term, MONOLITH could also serve as a detector for a very long baseline neutrino factory beam.

2.2 "Neutrino stoichiometry" with atmospheric neutrinos

MONOLITH is a massive magnetised tracking calorimeter, explicitely designed to significantly contribute in elucidating the pattern of neutrino masses and mixings, by exploiting the as yet poorly explored high energy component of the atmospheric neutrino fluxes. The main physics goals of the experiment are to firmly establish/disprove the neutrino oscillation interpretation of the up/down asymmetry reported by the Super-Kamiokande collaboration [6], clarify the nature of the oscillation mechanism and precisely measure the oscillation parameters involved ("neutrino stoichiometry"). In this context, the following techniques have been mainly considered:

- explicit observation of an oscillation pattern in the L/E spectrum from the comparison of upward and downward rates of charged current interactions of high energy muon neutrinoss;
- comparison of upward and downward rates of muon-less events of high energy;
- study of earth induced matter effects on upgoing neutrinos.

The first technique ("ν_μ disappearance"), already investigated in [13, 14], requires the capability to reconstruct in each event the L/E ratio of the neutrino path-length to its energy. Oscillations of muon neutrinos would manifest themselves in a modulation of the L/E spectrum, from which the oscillation parameters can be measured. We shall demonstrate that this technique, formerly suggested in [18], has sensitivity to ν_μ oscillations for $\Delta m^2 > 6 \times 10^{-5}$ eV^2 up to a few 10^{-1} eV^2 and mixing near to maximal and fully covers the region of oscillation parameters suggested by the Kamioka results (fig. 2.1).

The second ("ν_τ appearance") technique can shed light on the nature of the oscillation mechanism, by discriminating between the hypothesis of oscillations into a sterile or a tau neutrino. It consists in searching for the appearance of ν_τ interactions contributing to muon-less events of high energy can be searched for. This method is effective for $\Delta m^2 > 3 \times 10^{-3}$ eV^2. Additional or complementary information on the oscillation mechanism can be obtained from the study of potential matter effects related to the propagation of upgoing neutrinos through the Earth, resulting in a distortion of the oscillation pattern as a function of the energy and/or of the lepton number of the neutrino. As we shall discuss, this method is effective in discriminating the $\nu_\mu - \nu_s$ scenario for small values of Δm^2 (below 3×10^{-3} eV^2), thus complementing the previous technique.

2.2.1 Why atmospheric neutrinos?

Atmospheric neutrino experiments offer several advantages over currently operational or planned long baseline neutrino beam programs.

- A very large L/E range (from about 1 km/GeV to 10^5 km/GeV; a typical long baseline beam covers only one or two orders of magnitude). Therefore, a very large range of oscillation parameters can be studied simultaneously.
- Two identical sources for a single detector: a near (downgoing neutrinos) and a far (upgoing neutrinos) one.
- For some of the measurements, e.g. the confirmation of the oscillation pattern, there is currently no alternative to atmospheric neutrino detectors if the atmospheric Δm^2 is low. The pattern measurement is competitive even at high Δm^2.
- During the next decade large matter effects with high energy neutrinos can only be observed in atmospheric neutrino experiments, since the current long baseline distances of 250 and 730 km are too short for a significant effect. Matter effects already yield discrimination between the pure 2-flavour $\nu_\mu - \nu_\tau$ and $\nu_\mu - \nu_{sterile}$ oscillation scenarios in Super-Kamiokande and MACRO. Adding muon charge discrimination in future large mass detectors allows the search for MSW-like resonances in subdominant contributions to 3 or more flavour oscillations. In particular, some sensitivity to the determination of the sign of the atmospheric Δm^2 and to complicated hybrid oscillation scenarios can be obtained.

Future new atmospheric neutrino experiments are therefore an important complement to current and future long baseline neutrino programs.

2.2.2 Observation of neutrino oscillation pattern

In the two flavour approximation, the survival probability for neutrino oscillations in vacuum can be expressed by the well known formula

$$P(L/E) = 1 - \sin^2(2\Theta)\ \sin^2(1.27\ \Delta m^2\ L/E) \tag{2.1}$$

where L is the distance travelled in km, E is the neutrino energy in GeV, Θ is the neutrino mixing angle, and Δm^2 is the difference of the mass square eigenvalues expressed in eV^2.

However, none of the experiments which have yielded indications for neutrino oscillations have so far succeeded to measure an actual sinusoidal oscillation pattern. Figure 2.2 shows the L/E distribution published by Super-Kamiokande [6] compared to the expectation for neutrino oscillations and to a functional form suggested by a recent neutrino decay model [10]. Once the detector resolution is taken into account, the two hypotheses are essentially indistinguishable [10]. Even though the current evidence is very suggestive of neutrino oscillations, a more precise measurement of the oscillation pattern is the only way to actually prove the oscillation hypothesis for atmospheric neutrinos. The crucial issue here is to prove that muon neutrinos do not only disappear, but actually reappear at some larger L/E.

The proposed MONOLITH experiment is explicitly designed to fill this gap. Having a similar mass as Super-Kamiokande, significantly larger acceptance at high neutrino energies and better L/E resolution, the experiment is optimized to observe the full first oscillation swing, including ν_μ "reappearance". Therefore, the oscillation hypothesis can be clearly distinguished from other hypothesis which yield a pure disapperance threshold behaviour (figure 2.2).

Furthermore, the sensitivity is almost independent of the oscillation parameters (chapter 5). This is in contrast to MINOS, which can do a similar measurement at the highest allowed Δm^2

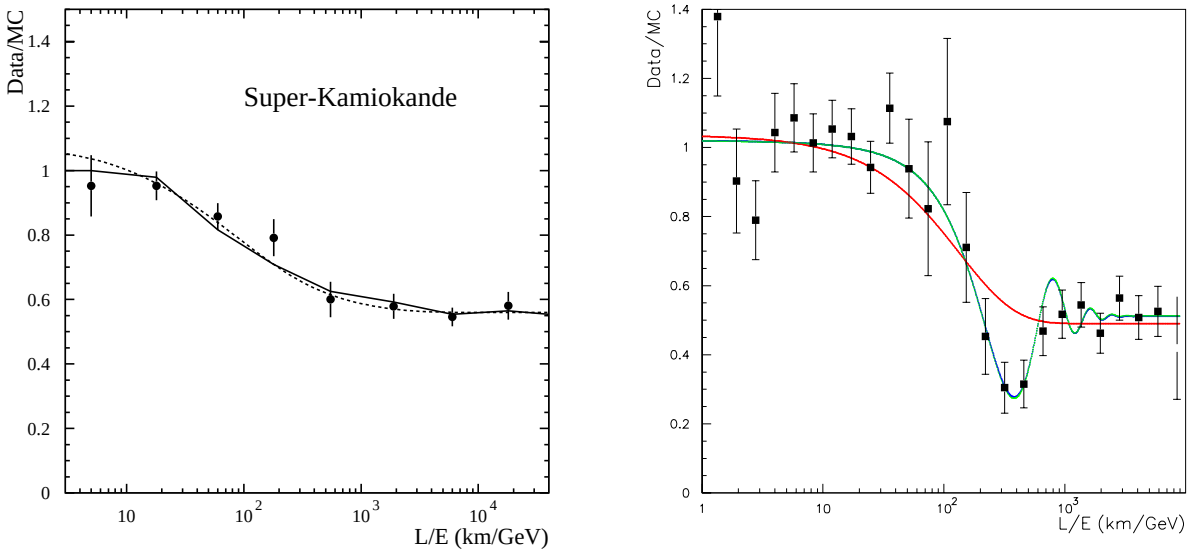

Figure 2.2: *Left*: L/E distribution from Super-Kamiokande [6, 27] compared to the best fit oscillation hypothesis (continous line), and to a parametrization corresponding to the neutrino decay model of ref. [10] (dashed line). The oscillations are smoothed out by detector resolution. *Right*: L/E distribution to be expected from MONOLITH (see Chapter 5) for $\Delta m^2 = 3 \times 10^{-3}$ eV^2 compared to the best fit oscillation hypothesis (oscillating line) and to the corresponding best fit of the neutrino decay model of ref. [10] (smooth threshold effect).

if the low energy beam is used [35], but has a hard time to observe a reappearance signal in the lower Δm^2 range.

Finally, the better L/E resolution can be used to significantly improve the measurement of the oscillation parameters over the full allowed range (fig. 2.1 and chapter 5).

2.2.3 Distinction of $\nu_\mu \to \nu_\tau$ vs. $\nu_\mu \to \nu_s$

If the current indications for three independent Δm^2 are confirmed, the only way out is the introduction of at least a fourth neutrino. Taking into account the LEP results [36] on the number of neutrinos, any extra neutrinos must be either very massive ($m_\nu > M_Z/2$) or sterile with respect to weak interactions (e.g. a right-handed neutrino or left-handed antineutrino). Present experiments are only now starting to distinguish oscillations with sterile neutrinos from standard flavour oscillations for either atmospheric [37] or solar [4] neutrinos. Significant $\nu - \nu_s$ oscillation contributions are therefore allowed in both cases [16, 38].

Since the existence of one or more light sterile neutrinos would be evidence for new physics, proving or disproving the $\nu_\mu - \nu_\tau$ oscillation hypothesis for atmospheric neutrinos is a crucial issue. Furthermore, it would exclude or confirm a large class of neutrino oscillation models (see e.g. [39] and references therein). The observation of τ appearance in long baseline beams would be the most direct evidence for $\nu_\mu - \nu_\tau$ oscillations, but potentially leaves some loopholes for the interpretation of the atmospheric neutrino results [40]. These loopholes would be closed by a direct $\nu_\mu \to \nu_\tau$ vs. $\nu_\mu \to \nu_s$ distinction in atmospheric neutrino experiments.

The Super-Kamiokande experiment is starting to disentangle the ν_s and ν_τ oscillation hypotheses using several approaches. The current measurement [41] of the double ratio of "π^o"

events [42]

$$\frac{(\pi^0/e)_{data}}{(\pi^0/e)_{MC}} = 1.00 \pm 0.06(stat) \pm 0.23(syst) \tag{2.2}$$

is compatible with both solutions (the expected ratio is 1 for ν_τ and ≈ 0.76 for ν_s). This measurement is mainly limited by systematic uncertainties on the cross section (currently 20%). The K2K experiment, with the near detector, will allow to reduce this systematic error, but even reducing the total uncertainty to 10% is unlikely to yield a 3σ evidence [40]. Also the study of the π^o up/down asymmetry [43] is unlikely to reach a 3σ significance on its own in the discrimination between the two hypotheses.

The second approach is based on potential matter effects affecting $\nu_\mu \rightarrow \nu_s$ oscillation inside the Earth. Matter effects can radically modify the neutrino oscillation pattern with respect to oscillations in vacuum [44]. These effects occur for oscillations involving neutrinos having different interactions with matter. So matter effects are absent for $\nu_\mu \rightarrow \nu_\tau$ oscillations and present for $\nu_\mu \rightarrow \nu_e$ and $\nu_\mu \rightarrow \nu_s$ oscillations. Due to these effects, the expected shape of the zenith distribution of up-going muons is different for $\cos(\theta) \leq$ -0.4, as pointed out in [45]. The same is true for high energy semi-contained events.

The Super-Kamiokande collaboration [27] presented an analysis disfavoring the pure $\nu_\mu \rightarrow \nu_s$ hypothesis at the 99% confidence level by combining this approach with the neutral current up/down asymmetry. Using upward going muons only MACRO has found a similar, but somewhat less significant indication [46]. More complicated scenarios with 3 flavour oscillations can not be excluded with the existing data. [16].

The MONOLITH experiment can exploit the spirit of both approaches to improve on these measurements. The first technique, based on τ appearance, consists in measuring the up/down asymmetry of "NC-like" events (muon-less events) as a function of the visible energy. For $\Delta m^2 \leq 10^{-2}$ eV^2, oscillations of ν_μ into ν_τ would in fact result in an excess of muon-less events produced by upward neutrinos with respect to muon-less downward, since charged-current ν_τ interactions would contribute to the muon-less event sample, due to the large τ branching ratio into muon-less channels. Moreover, due to threshold effect on τ production, this excess would be important at high energy. Oscillations into a sterile neutrino would instead result in a depletion of upward muon-less events. Discrimination between $\nu_\mu \rightarrow \nu_\tau$ and $\nu_\mu \rightarrow \nu_s$ is thus obtained from a study of the asymmetry of upward to downward muon-less events.

Because this method works with the high energy component of atmospheric neutrinos, it becomes effective for relatively large values of Δm^2 ($\geq 3 \times 10^{-3}$ eV^2). Depending on Δm^2, a separation of the ν_τ and ν_s hypotheses of up to 3 σ is within the reach of the experiment (see chapter 5). This up/down study will be much less affected by systematic uncertainties on cross sections and/or detector acceptance than NC/CC studies.

For the second technique, based on potential matter effects, an analysis similar to the one recently performed by Super-Kamiokande [27] can be carried out on the sum of the neutrino and antineutrino components of the atmospheric neutrinos, using the fact that $\nu_\mu - \nu_s$ oscillations get suppressed at high energies. In MONOLITH, the significance of the result can be improved by the higher acceptance for high energy contained and semi-contained events, and its capability to measure the momenta of upward through-going muons. Furthermore, the predicted shape and position of the first oscillation minimum (section 2.2.2) becomes energy and angle-dependent, yielding an additional handle for the $\nu_\tau - \nu_s$ discrimination.

Moreover, with the exception of the special case of maximal mixing ($\sin^2(2\Theta) = 1$), neutrinos and antineutrinos have different oscillation parameters in matter. The effective mixing in matter becomes maximal when the resonance condition [47] is satisfied. This is possible for antineutrinos (neutrinos) when Δm^2 is positive (negative). Additional resonance effects are possible if the matter density varies along the neutrino path [48]. So in the case of non-maximal oscillations with matter effects we expect a change in the observed $\nu_\mu/\bar{\nu}_\mu$ ratio. This phenomenon could

be used to measure the sign of Δm^2. In this context we can use the MONOLITH capability to separate the ν and $\bar{\nu}$ component and to measure muon momenta up to several hundred GeV. The corresponding analysis is still ongoing and will be described in a later version of this document.

2.2.4 Three flavour oscillations

Even in the absence of sterile neutrinos, matter effects are present in the case of a small contribution from $\nu_\mu - \nu_e$ oscillations at the "atmospheric" Δm^2. The CHOOZ limit [20] constrains the size of this contribution, and the expected effects are mostly small. However, if the $\nu_\mu - \nu_e$ mixing angle would be close to the CHOOZ limit, the corresponding MSW resonance might be observable [49] as a localized ν_μ rate suppression either in ν_μ or in $\bar{\nu}_\mu$, yielding a measurement of the sign of Δm^2. This possibility is currently being investigated further. Another possible exception could be the observation of a large neutrino/antineutrino asymmetry predicted by tri-maximal mixing models [50], which are currently not yet completely excluded. Furthermore, fits of the solar neutrino results leaving out Homestake allow the solar Δm^2 to be as high as a few 10^{-4} eV^2. If the mixing is nonmaximal, differences in the ν and $\bar{\nu}$ rates could again be observed.

2.3 Measurements with neutrino beams

2.3.1 Complementary measurements with CNGS beam neutrinos

The MONOLITH detector design is not optimal for events from the CNGS beam [29] due to the horizontal orientation of the detector planes. However, in the adopted modular design, the magnetic field is oriented perpendicular to the beam direction, and stopping muons are deflected out of the horizontal plane, and therefore well measured. The addition of a vertical downstream end cap yields improved performance for partially contained muons.

One of the strengths of a 34 kt detector is its high event rate: with the upgraded CNGS beam performance [29], about 300.000 CC events with energies in the range 10-30 GeV could be expected in 4 years of running. Ideally, the presence of a near detector would allow to carry out the equivalent of the full physics programme discussed in [15] and [24]. Since a near detector pit is not forseen, the initial beam normalization is poorly known, and the remaining physics possibilities are limited to measurements of the beam *shape*, for which the systematic error is smaller and the effects are potentially much larger.

Based on the experience from previous beam simulations [51] we assume uncertainties of order 10-20% in the absolute beam flux prediction. This makes any significant measurement of ν_μ disappearance from the rate measurement alone impractical. Reversing the argument, the high event rate could be used to precisely *measure* the beam flux (modulated by oscillations). Once the oscillation parameters are known, for instance from the MONOLITH atmospheric neutrino measurements, this could reduce the beam uncertainties for τ appearance experiments.

However, the error on the *relative* beam shape as a function of energy is known from WANF studies [51] to be under much better control. Although ambitious, a relative error of order 5% over a suitably chosen energy range does not seem to be out of reach, and could be verified by comparing measured neutrino and antineutrino spectra. An error of this size is also usually assumed for the shape of the atmospheric neutrino spectrum. Measurements of the modification of the beam *shape* are therefore much less affected by the absence of a near detector. Preliminary estimates indicate that the somewhat reduced performance due to the non-beam-optimized detector design is compensated to a large extend by the large event rate (7 times the mass of MINOS), such that the overall performance for *shape* measurements above $E_\nu = 5$ GeV is competitive with MINOS. If MINOS chooses the low energy beam option, these measurements might even be unique. For instance, LSND-inspired oscillations at a Δm^2 of 0.2 eV^2 could induce an *additional* short period modulation in the high energy end of the beam spectrum, which would be detectable, or could be excluded. Corresponding studies are in progress.

Another interesting topic is a *combined* analysis of atmospheric and beam neutrino data for ν_μ disappearance (beam) and reappearance (atmospheric). At high Δm^2, the complementarity of the samples makes the combined data set more robust against random fluctuations in the critical dip region. Fig. 2.3 shows the result of such a simulation for 2 years of atmospheric neutrino data taking, and 1 year in the beam, for $\Delta m^2 = 5 \times 10^{-3}$ eV^2.

Depending on the size of the associated systematic error, indirect measurements of τ appearance through the measurement of the NC/CC ratio might also offer some possibilities. Previous measurements of this ratio for other purposes in high density calorimeters [96] have achieved systematic errors in the 0.5-1% range. However, all these results were obtained at neutrino energies of typically 50-100 GeV. Detailed studies are needed to establish the performance in the 10-30 GeV range, including the possibility to use the high event rate to study some of the systematic errors from the data themselves. Contrasting the expected error of a few % with the expected apparent NC/CC enhancement for $\nu_\mu - \nu_\tau$ oscillations ($\sim 1 - 20\%$ depending on Δm^2), it seems likely that a meaningful measurement can only be achieved if Δm^2 is large.

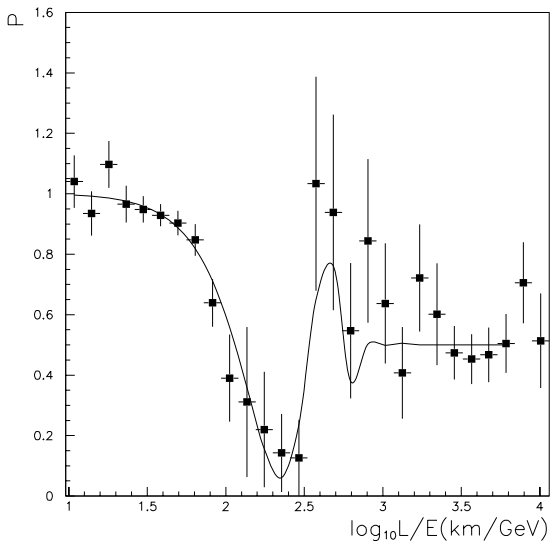

Figure 2.3: Example for the expected L/E distribution (ν_μ survival probability) in MONOLITH with 2 years of data taking of atmospheric neutrinos and 1 year with the CERN-Gran Sasso neutrino beam for $\Delta m^2 = 5 \times 10^{-3}$ eV^2 (points). Also shown is a fit of the expected oscillation hypothesis (continous line). Beam neutrinos dominate the L/E region below 10^2 km/GeV. For L/E $> 10^2$ km/GeV only atmospheric neutrinos contribute. Only statistical errors are shown.

2.3.2 Physics with beams from muon storage rings

Neutrino beams from future muon storage rings [52] (neutrino factories) will be essentially pure beams of either $\nu_\mu + \bar{\nu}_e$ or $\bar{\nu}_\mu + \nu_e$. The occurence of $\nu_e - \nu_\mu$ or $\nu_e - \nu_\tau$ oscillations would therefore manifest itself via the appearance of wrong sign muons. A massive magnetized iron detector like MONOLITH, with good muon charge separation and momentum measurement, could therefore be well suited [53] for the observation of such oscillations. As pointed out in [54, 55] this kind of beam will in particular offer the possibility to measure the θ_{13} mixing angle, currently only constrained by the Super-Kamiokande and CHOOZ results, and the sign of Δm^2 through matter effects. Depending on which of the solar neutrino solutions is correct it might also open the way for the study of CP violation in the neutrino system.

Interestingly, the optimization of detectors for the neutrino factory, focusing on wrong sign muon appearance measurements, has yielded a detector [53] whose basic parameters are very similar to those of MONOLITH. This is true in particular when the source is far enough away to impinge at a sizeable angle from below (horizontal geometry of MONOLITH). For instance, a beam from Fermilab (L=7300 km) would impinge at an angle of 35^o, and be almost aligned with the Gran Sasso hall axis, and therefore perpendicular to the magnetic field axis. The results obtained in the physics studies of ref. [17] concerning the measurements of θ_{13}, sign of Δm^2, and CP violation therefore qualitatively *apply to MONOLITH* used as a neutrino factory detector. Of course the potential timescale of a neutrino factory is quite different from the one of the current atmospheric neutrino program. Nevertheless, it might be interesting to consider that such a facility might become reality within the lifetime of the MONOLITH project, and that its useful life might be extended accordingly.

2.4 Cosmic ray muon studies

MONOLITH is also well suited for the study of very high energy cosmic ray muons. Using a so-called "pair meter" technique explained in chapter 7, the energy of each muon in the multi-TeV range can be directly measured. The resulting measurement of the cosmic ray muon spectrum yields the opportunity to test potential extensions of the standard model which would affect the shape of this spectrum.

The spectrum of primary cosmic ray particles measured by means of extensive air shower (EAS) observations is well described by a power law over many decades in energy. However, it exhibits a well known change in slope (the so-called knee) between 10^{15} and 10^{16} eV (1-10 PeV). In nucleon-nucleon collisions, PeV energies in the laboratory frame correspond to centre-of-mass energies in the TeV region, where new physics and new (heavy) particles are predicted by various theoretical models. Above 2 TeV, these energies are out of the reach of existing accelerators.

There are two main possibilities for the explanation of the knee: a change of the primary spectrum (and/or composition), or the appearance of new processes in very high energy interactions. Currently, most investigators support the first point of view. However, the second option remains possible (see for example [56]). To explain the knee in this way, one should assume that the primary spectrum is not changed, but part of the primary energy (above the knee) is carried away by particles which are not or incompletely detected by EAS arrays (Fig. 2.4). This

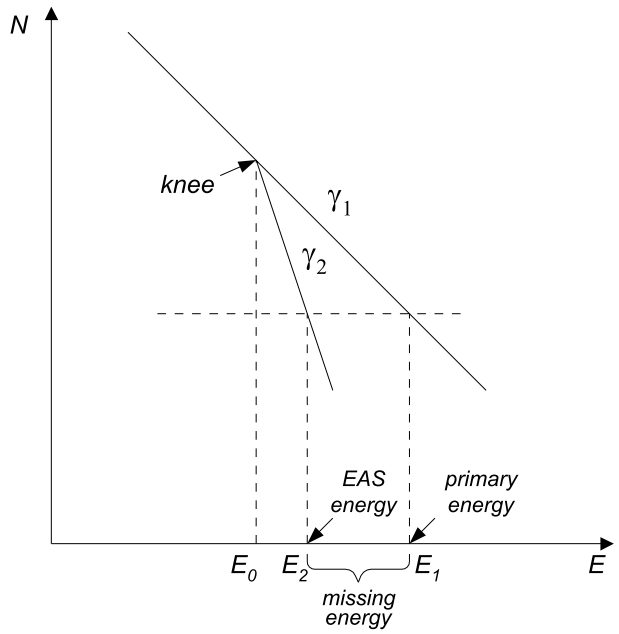

Figure 2.4: Explanation of missing EAS energy (see text).

missing energy ΔE may be estimated as [57]

$$\frac{\Delta E}{E_1} = 1 - \left(\frac{E_0}{E_1}\right)^{\Delta\gamma/\gamma_2} \tag{2.3}$$

where γ_1 and γ_2 are the power indices of the primary spectrum and of the EAS spectrum above the knee, E_1 and E_2 are the primary particle energy and the detected EAS energy, $\Delta\gamma = \gamma_2 - \gamma_1$, and E_0 is the knee position. Among the known particles only neutrinos and very high energy muons can carry this missing energy. Neutrinos remain undetected, and usual EAS setups do

not measure the muon energy but only estimate their number. In turn, these leptons could originate from the decay of new particles in the several TeV mass region or from a new state of matter (supersymmetry, compositeness, technicolor, quark-gluon plasma, superstrings, etc.). To have the necessary impact, such particles or states should be produced with a large cross section (of the order of tens of mb). As was pointed out recently [57], a good possibility to find such new particles in cosmic rays is to perform a direct measurement of the muon energy spectrum in the region of 100 TeV and higher.

The expected fluxes of very high energy (VHE) muons which are needed for the explanation of the knee within the frame of the above model are shown in Fig. 2.5, together with the rate of standard cosmic ray muons (origination from π, K decays). In 3 years the MONOLITH detector will allow to register about 100 events with surface muon energies exceeding 100 TeV for conventional muon production mechanisms, whereas about 2-3 times higher statistics may be expected in the case of the appearance of the "new" muons. At 1 PeV, the expected rate could be increased by more than an order of magnitude. This drastic change of the muon energy spectrum around 100 TeV would be an excellent signature of new processes.

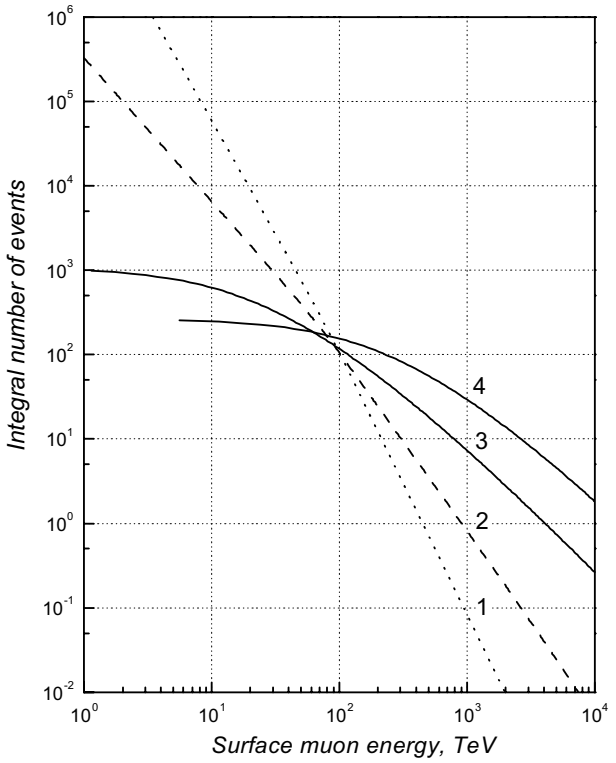

Figure 2.5: Expected integral spectra of muons from various processes crossing MONOLITH in 3 years: 1 - muons from π, K decays; 2 - "prompt" muons for a ratio $R_{\mu/\pi} \sim 10^{-3}$; 3 and 4 - lower and upper estimates for muons from new VHE sources to explain the "knee" (see text).

Some evidence for the presence of VHE muons in the cosmic ray flux exists [58, 59]. However, it should be stressed that the necessary condition for the separation of the flux of new muons from the usual ones is the measurement of individual muon energies at 100 TeV and higher. None of the existing methods and experimental setups allow to reach these energies. For example, the biggest magnetic spectrometers operated so far had an acceptance of only about 0.1 m^2 sr and a maximum detectable momentum less than 5 - 20 TeV. The derivation of the muon energy spectrum from the depth-intensity curve has a fundamental upper limitation, since at depths

corresponding to effective surface muon energies of about 50 - 70 TeV the intensity of atmospheric muons becomes less than that of muons produced in local neutrino interactions. Another indirect method - detection of cascades originated from muon bremsstrahlung - is statistically limited due to the relatively low value of the corresponding cross section. Horizontal air shower observations give only marginal upper limits of the VHE muon flux.

The structure of the MONOLITH detector allows to utilise a new method of muon spectrometry (pair meter technique) which provides the possibility of muon energy measurements in the 100 TeV range. Thus, in the case of a positive result, muon energy spectrum studies with MONOLITH may lead to the discovery of new physical processes of muon generation in the TeV (centre-of-mass) energy region. On the other hand, the absence of an excessive muon flux in this energy range would reinforce the evidence in favour of a cosmophysical origin of the knee.

Along with the search of new sources of very high energy muons, MONOLITH will provide unique opportunities of traditional investigations related to the primary spectrum, composition, and production mechanisms of cosmic ray muons in the energy range 10 - 100 TeV. Available data in this energy region are incomplete and often controversial, due to the smaller size of the setups and/or limitations of the used spectrum measurement techniques.

The inclusive spectrum of cosmic ray muons carries information about the primary spectrum (at about 10 times higher energy per nucleon), and studies of the muon energy distribution in this domain will help to fill in the gap between direct primary spectrum measurements in balloon-based and space-based experiments, and air shower observations. Detection of multi-muon events (muon bundles) allows to study the primary spectrum and composition at even higher energies, around and above the knee ($10^6 - 10^7$ GeV). A detailed analysis of muon bundles from the view-point of cosmic ray mass composition in this energy range has been recently presented by the MACRO Collaboration [60]. This analysis is based on bundle multiplicity and muon decoherence parameters. The introduction of a new important observable, the individual particle energy, with statistics comparable to the MACRO experiment, will significantly increase the robustness of the analysis results relative to variation of EAS development models, and thus allow to obtain more definite conclusions about the characteristics of the primary cosmic ray flux.

Another long-standing problem of atmospheric muon studies is related to so-called "prompt" muons, which presumably arise from the decays of charmed hadrons. Due to the short life time of the parent particles, these muons should exhibit a harder energy spectrum (difference of about one unit in the power spectrum index compared to muons from π, K decays) and a nearly isotropic distribution in zenith angle. Because of a lack of reliable extrapolations of the charm production cross section in the forward region at high energies, theoretical predictions of the prompt muon contribution differ by more than a factor 10. Experimental data on this component are also controversial. Measurements of muon energy and angular distributions with the MONOLITH detector operated as a pair meter will allow either to reliably confirm the existing evidence for prompt muon observation [59], or to significantly improve upper limits for the contribution of this process. New quantitative estimates of the charm production cross section at high energies can thus be obtained in a kinematic region which cannot be explored in collider experiments.

2.5 Other physics topics

Other potential physics topics, which have not yet been studied in detail, include the study of the primary atmospheric neutrino/antineutrino flux ratio, studies of the shadow of the sun and the moon (verification of the angular resolution), the search for astrophysical neutrino point sources, and the search for a neutrino line (in E_ν) from WIMP annihilation in the center of the earth.

Chapter 3

Experimental Setup

3.1 Introduction

To explicitly detect an oscillation pattern in the L/E spectrum of atmospheric muon neutrinos, the energy E and direction θ of the incoming neutrino have to be measured in each event. The latter can be estimated, in the simplest experimental approach, from the direction of the muon produced from the ν_μ charged-current interaction. The neutrino energy E can be obtained by means of energy measurements of the muon and of the hadrons produced in the interaction. In order to make the oscillation pattern detectable, the ratio of the neutrino path-length to its energy L/E have to be measured with a FWHM error smaller than half of the modulation period. The energy and angular resolutions of the detector or, more generally, the experimental approach are constrained by this condition. The L/E resolution improves at high energies, mostly because the muon direction gives a better estimation of the neutrino direction. Thus the ability to measure high momentum muons (in the multi-GeV range), which is rather limited in the on-going atmospheric neutrino experiments, is particularly rewarding.

These arguments previously led some of us to consider as a suitable detector a large mass and high-density tracking calorimeter [14]. A large mass is necessary to provide the necessary number of neutrino interactions at high energy, while the high density allows high energy muon containment (i.e. muon momentum determined by range). A sizeable increase in sensitivity for Δm^2 larger than 3×10^{-3} eV^2 can be achieved with the addition of a magnetic field. This improves the efficiency at small L/E as a consequence of the increased muon acceptance at high momenta. Moreover a high-density detector allows to select a pure ν_μ-CC sample providing good π/μ separation. The measurement of the muon energy and direction can be obtained with good precision. On the other hand the overall low energy neutrino sample L/E resolution can be controlled, even with a coarse resolution to hadrons, by selecting interactions of limited inelasticity. This is shown in the expression of the relative L/E resolution:

$$\frac{\sigma^2_{L/E}}{(L/E)^2} = \frac{\sigma^2_E}{E^2} + \frac{\sigma^2_L}{L^2} \tag{3.1}$$

$$\simeq \frac{\sigma^2_{E_\mu}}{E^2_\mu}(1-y)^2 + \frac{\sigma^2_{E_h}}{E^2_h}y^2 + \tan^2\theta\sigma^2_\theta; \tag{3.2}$$

where E, E_μ and E_h are the neutrino, muon and hadronic energies respectively, $y = E_h/E$ is the inelasticity of the interaction and θ is the zenith angle of the incoming neutrino. Events of limited inelasticity have both a good resolution on the neutrino energy, dominated by the resolution on the muon energy, and on the neutrino direction estimate from the muon direction. As shown in equation (3.2) the acceptance at small L/E can only be achieved by recovering events of high energy, since near the horizontal (at small L) the L/E resolution is intrinsically

limited by the knowledge of the neutrino direction. Therefore the detector does not need to be fully isotropic. Improvement of the L/E resolution through better hadron reconstruction would only be possible by using a calorimeter of much higher granularity, which increases cost, reduces muon containment and conflicts with the requirement of a large mass.

In addition to these requirements on the L/E resolution, the experimental apparatus should guarantee the identification of the neutrino flight direction. In case the interaction vertex is not identified, this condition turns out to be very stringent and requires the identification of the muon flight direction with high efficiency. Different techniques based on the increase of curvature along the track in the magnetic field, on multiple scattering along the track or on time-of-flight measurements can be used. The latter technique is more effective and allows almost perfect up/down discrimination of the relevant ν_μ-CC events for timing resolution of the order of 1 ns. A precise time-of-flight along the muon track will be also of utmost importance in the rejection of the cosmic muon background in the sample of partially contained ν_μ-CC events.

A high-density detector, optimized for the "ν_μ disappearance" method, also fulfills most of the requirements needed for the analysis of "ν_τ appearance" in atmospheric neutrinos, discussed in section 2.2. In order to make the ν_τ appearance method effective, a detector of large mass is necessary, due to the small expected rate of ν_τ events. Good discrimination of muon-less events from the residual background of ν_μ and ν_e charged current interactions is also needed. A coarse-grain calorimeter guarantees a reasonable rejection of events with penetrating tracks (muons), while its poor response to electromagnetic energy shifts the ν_e-CC interactions towards low visible energies, thus reducing the background of these events in the muon-less sample.

A detector with a relatively poor resolution to the hadronic energy could still be effective in the measurement of the up/down asymmetry of high energy muon-less events integrated over a wide energy range (although the sensitivity could benefit from an improved resolution).

The main experimental challenge is represented by the detector capability of discriminating upgoing from downgoing muon-less events. This discrimination can be based on the analysis of the event topology and could also benefit from timing information.

In summary, a detector performing the measurements discussed in the previous chapter has to provide NC/CC discrimination, muon momentum and charge measurement, some hadronic energy reconstruction capability, and up/down discrimination for muons above 1 GeV. Moreover it has to provide an event sample, with the requested L/E resolution, large enough to observe the modulation produced by ν_μ oscillations. A rejection power against incoming stopping muons better than 10^{-5} is needed in the Gran Sasso underground laboratory. Finally the detector has to fit into an existing hall of the LNGS and it must have a reasonable cost.

It should be noted that all this can be achieved by choosing a high-mass tracking detector with a coarse structure and magnetic field.

3.2 Detector structure

A large modular structure has been chosen for the detector (figure 3.1). One module consists in a stack of 125 horizontal 8 cm thick iron planes with a surface area of 15.0×14.5 m^2, interleaved with 2.2 cm gaps housing sensitive elements. The height of the detector is thus 13.1 m including anti-seismic mechanical supports. Thinner plates, 2 and 4 cm thick, were also considered in the past. However, the 8 cm plate thickness resulted to be the best compromise between physics results and detector cost. The magnetic field configuration is also shown in figure 3.1; iron plates are magnetized at a magnetic induction of ≈ 1.3 T.

The detector consists of two modules. Optionally, the downstream module could be complemented by an end cap of vertical planes (see figure 3.2) to improve the performance for non-contained muons from the CNGS beam (see section 2.3.1). The total mass of the detector

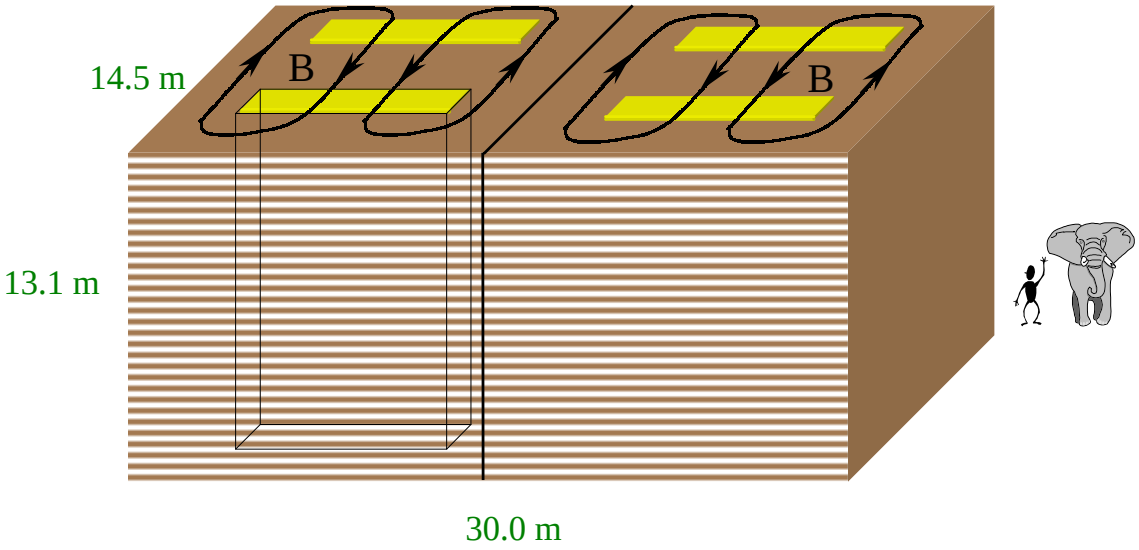

Figure 3.1: Schematic view of the MONOLITH Detector. The arrangement of the magnetic field is also shown.

exceeds 34 kt. The sensitive elements provide two coordinates with a pitch of 2.8 cm, and a time resolution of 2 ns.

A detector option with only vertical plates had also been considered in ref. [1], yielding similar performance. The horizontal plate option was chosen because it was both technically easier to realize and more efficient in rejecting the background from downward going cosmic ray muons. Nevertheless, an additional external veto made of scintillator planes has recently been added to the design (see section 3.3). It will provide redundancy in this background rejection, and might eventually be used to increase the effective fiducial volume.

Extensive studies, including power consumption and cost, have been performed for iron magnetization. A magnetic induction of about 1.2–1.4 T turned out to be affordable at reasonable cost and power consumption (see Appendix *A*).

Glass Spark Counters (i.e. Glass RPC) have been chosen as active detector elements.

Their performance and feasibility will be discussed in section 3.5.

The alternative option of scintillator bars with wave length shifter (WLS) read-out [1] was not pursued further due to the difficulty to achieve the required timing performance for 12 or 15 m long scintillator bars at reasonable cost.

The full detector is 30.0 m long, 14.5 m wide and 13.1 m high, which is consistent with construction and operation in the Gran Sasso Hall C. It is also possible to configure the detector for installation in Hall B. Specific studies will be performed if requested by committees. With the envisaged modular structure, we anticipate that the first module could be ready for operation 4 years after experiment approval.

3.3 External veto counters

The whole MONOLITH detector, as described in section 3.2, is foreseen to be surrounded by an external layer of scintillation counters. The function of these external "veto"-counters is twofold:

- to recognize muons that enter from outside the detector to reduce the corresponding background of muons of cosmic radiation and/or increase the useful fiducial volume.

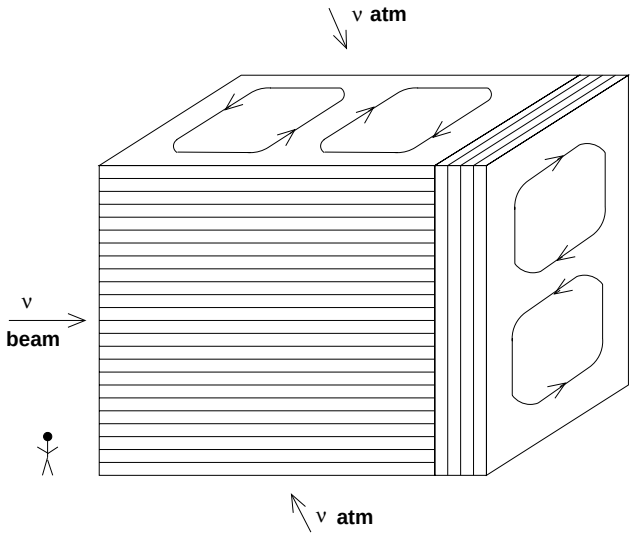

Figure 3.2: Sketch of the MONOLITH downstream module. The arrangement of the end cap option is shown.

- to contribute to the distinction of the contained and semi-contained event samples, and therefore to the optimization of the corresponding cuts.

The counters will therefore be used as a veto device for contained events and as an additional detection device for semi-contained events. The front and back faces can also be used to obtain an online measurement of the CNGS beam intensity via the rate of muons from both MONOLITH and the preceding rock.

Unless explicitly stated otherwise, all physics analyses presented in this document have been performed *without* using the veto information. The veto therefore provides partially redundant *additional* information which allows to further reduce the background, cross-check detector efficiencies, and increase the useful fiducial mass.

Most of the events recorded in MONOLITH will be caused by cosmic ray muons. The large majority of these muons cross the complete detector, or at least a large part of it, and are effortlessly identified using the tracking and timing information of the GSC's. Occasionally, some muons enter the detector without being recognized by the outmost GSC layers due to the non-perfect efficiency and because of geometrical gaps. Such muons travel a certain distance in the detector before they are detected and could be mistaken for downward neutrino-events. This background can be reduced to an almost negligible level by imposing certain fiducial cuts (see chapter 4).

As an alternative way to eliminate this remaining background, the whole detector (except some part of the floor) is surrounded by a hermetic layer of scintillation counters. These counters have to fulfill the following requirements:

- detection probability of more than 99% for minimum-ionizing particles (including geometrical efficiency).
- random coincidences with neutrino events (spatial and temporal misassignment) at most in the per mille range.
- a direct contribution to the time-of-flight measurement is not necessary (upward/downward event discrimination is obtained from the GSC's).

In addition to its good performance concerning efficiency and hermeticity, the scintillator technology has been chosen to allow independent cross-checks of detector efficiencies.

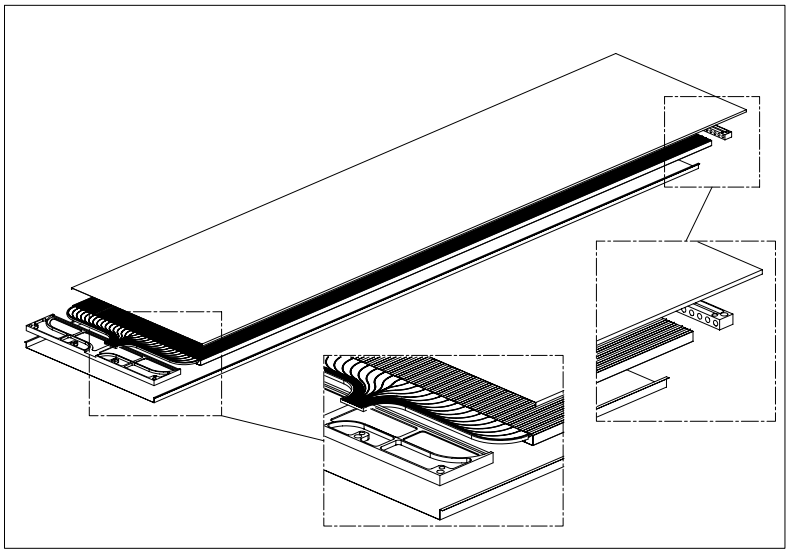

Figure 3.3: Basic scintillation counter element [72].

The corresponding detector design is not yet fully completed. The current preliminary design is based on scintillator elements similar to the ones which have been developed by the I216/P311 collaboration [72] (figure 3.3). Each basic element (extruded scintillator) of 51×4 m^2 is read out by 32 wavelength-shifting fibers, whose light is bundled and fed into a single photo-tube. The time resolution is of order 10 ns. In contrast to I216, the scintillator plate can be continuous. About 750 of such elements and the same number of TDC channels are necessary to cover the whole detector, including an overlap of neighboring counters in critical detector regions. To allow access to the GSC electronics, the counters are foreseen to be mounted on mobile supports on the long sides of the detector.

3.4 Magnetization of the iron plates

A layout in which each field line lays entirely inside an individual iron plate has been chosen in order to avoid huge power consumption and stray field. As shown in figure 3.1, to obtain this, a *vertical* slot crossing all the stack is needed, through which the currents generating the field have to pass (see Appendix A of this document and Appendix A of ref. [1] for more details).

In these Appendices it is also shown that this layout allows to create a field of the order of $1.2 \div 1.4$ T, with a power consumption not exceeding 200 kW and a cost of the windings not exceeding 500 kEuro. Other layout which were also considered in [1] did not offer any significant advantages over the chosen option.

3.5 Glass Spark Counters

3.5.1 Basic structure and operation

Taking into account the overall dimensions of the apparatus outlined in section 3.2 (125 planes 30.0 m long and 14.5 m wide) the total active detector area is ~ 54000 m^2. The large active area requires a low cost detector, suitable for a fast mass production.

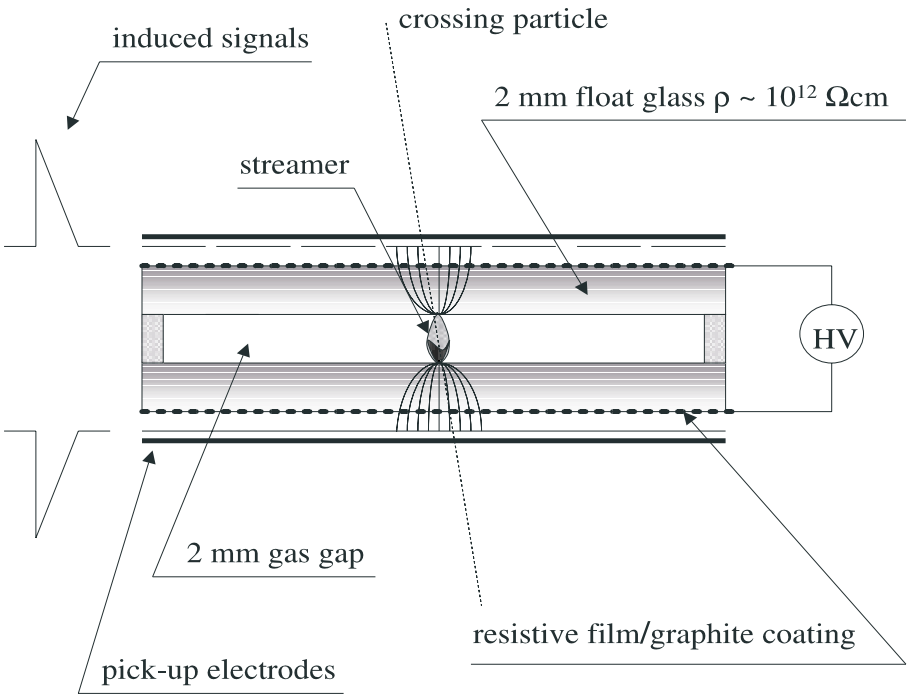

Figure 3.4: GSC: principle of operation.

For these reasons Glass Spark Counters (GSC) [61, 62, 63, 64, 65, 66, 67] have been chosen as active elements. They are derived from resistive-plate chambers by substituting the bakalite by commercial float glass of high resistivity (10^{12} Ωcm); for this reason they are sometimes called Glass RPC. Moreover they provide a timing of the order of 1-2 ns, and therefore excellent up-down discrimination of muons.

The GSC (figure 3.4) is a gaseous detector composed by two parallel electrodes made of glass with a volume resistivity of about 10^{12} Ωcm. The two electrodes, 2 mm thick, are kept 2 mm apart by means of suitable spacers. The gap between the two glass electrodes defines the gas volume where the particle detection occurs. Under particular gas mixture and electric field configurations (typically ∼48% Argon + ∼4% isobutane + ∼48% R134A and ∼4÷5 kV/mm) the detector is operated in spark mode. Typical signal amplitudes of the order of 100÷200 mV/50 Ω are observed, corresponding to a charge of about 100÷200 pC (depending on the intensity of the applied electric field).

The use of highly resistive material as electrodes ensures that the spark discharges just a limited area around the spark location. The time to recover the electric field, depending on the electrode resistivity ($\tau \sim \rho\varepsilon$, where ρ is the glass volume resistivity and ε is its dielectric constant), avoids self-sustaining sparking.

The read-out of the detector is performed with external pick-up electrodes, allowing a bi-dimensional localization of the crossing particles together with time information.

The details of the current GSC design and the proposed arrangement for the apparatus plane will be discussed in the next section.

3.5.2 GSC and apparatus design

A sketch of the GSC design is shown in figure 3.5 [66]. It consists of a couple of float glass

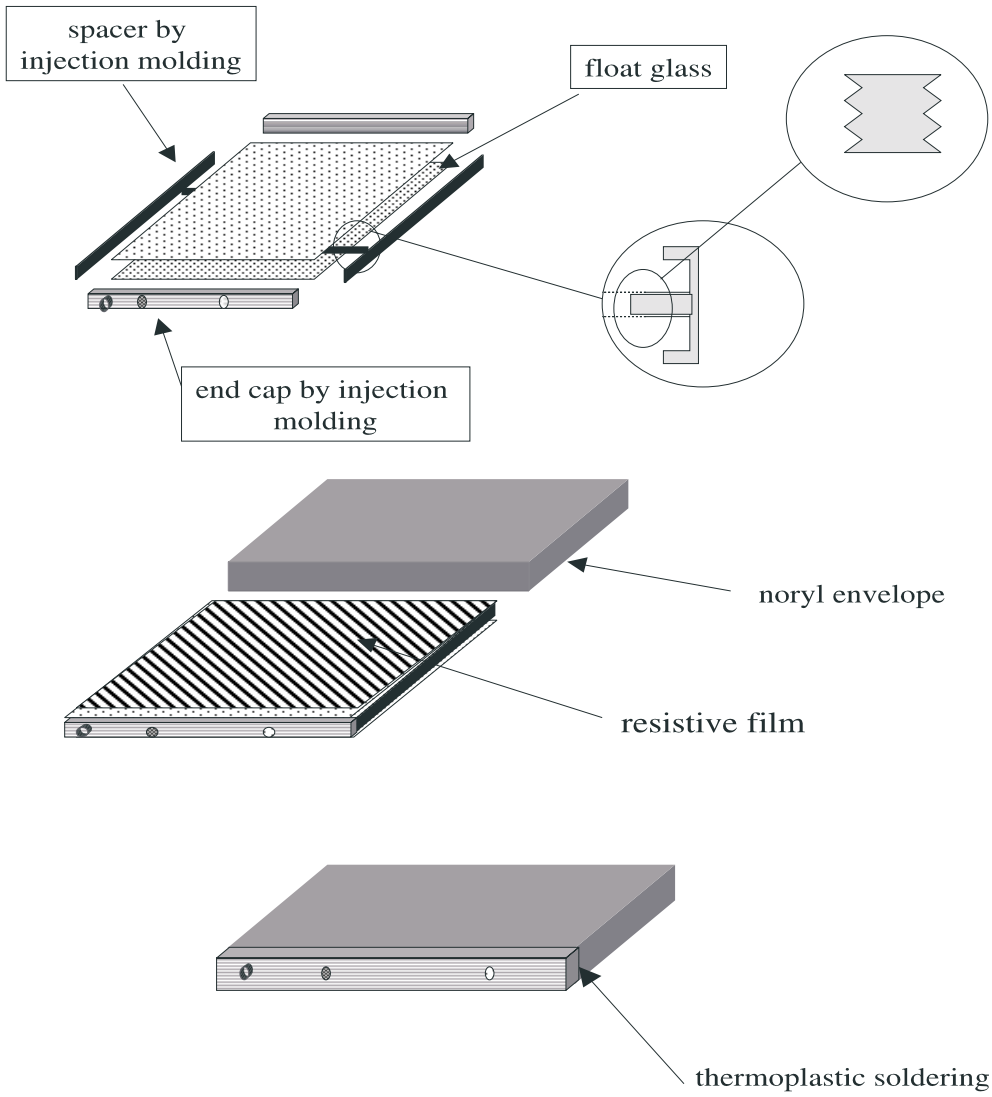

Figure 3.5: Schematic view of the GSC.

electrodes. The 2 mm distance between the electrodes is ensured by NORYL spacers clamping the edges of the glass plates. These spacers sustain both electrodes, ensuring a gap tolerance at the level of a few microns, for uniform working conditions in a such large apparatus. The high voltage is applied to the electrodes by means of resistive adhesive film with a surface resistivity of about 200 kΩ/square. The detector is inserted into an extruded NORYL envelope, that ensures the gas containment. In such a way a possible variation of gas pressure does not change the distance between the electrodes. The HV connections to the resistive film are located in one of the two end caps that close the GSC module. External pick-up strips (not shown in figure 3.5) are used to detect the induced pulses. All the materials used are commercially available, while the manpower is essentially due to film application on the glass surface and to the detector module assembling. This detector is conceived for the use in a underground laboratory. In fact all the

materials are halogen free (PVC has been replaced by NORYL), the gas mixture is ecological and not flammable (Freon has been replaced by R134A, the isobutane percentage is well below the flammability level). During the last 10 years the performance, life-time and reliability of the GSC detector has been extensively studied by some of us. GSCs have been successfully employed in the K_L and muon detection subsystem (KLM) of the BELLE experiment. [67].

Further detailed studies have been also performed on the glass properties [64], [65] and on the detector design optimization and engineering in order to make its construction easy and fast [66].

Extended GSC performance tests have been performed using an 8 t prototype. The corresponding results are reported in section 3.9.

For the MONOLITH apparatus (figure 3.6) the GSCs will be equipped with X and Y pick-up strip electrodes, both with a pitch of $\sim$ 3 cm (2.8 cm), mounted on the opposite side of the detector planes. The pulses are induced on the strips and then discriminated by the electronics directly connected on the strip ends. The electronics should also provide a fast discriminated signal for timing purposes.

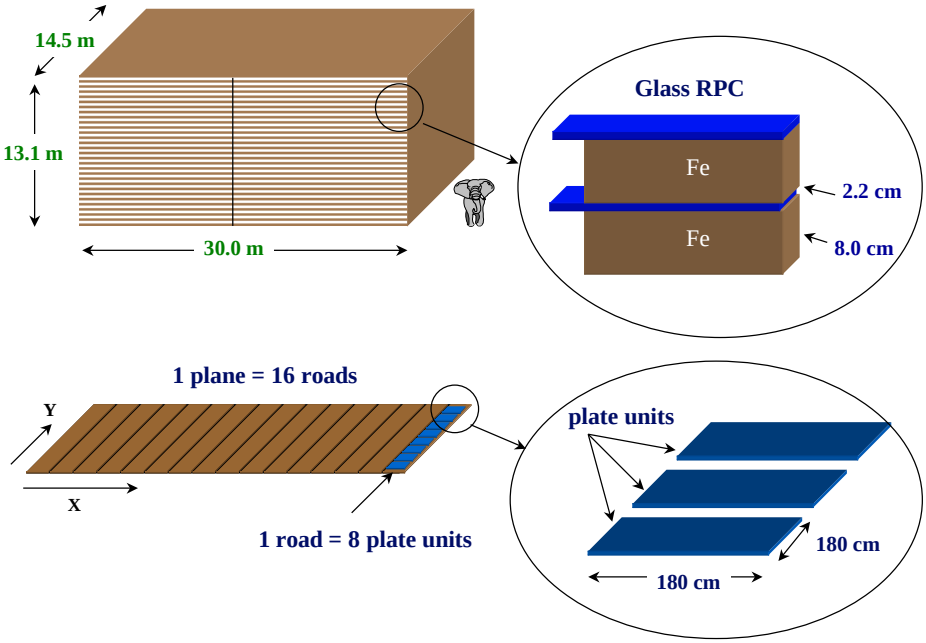

Figure 3.6: Schematic view of the MONOLITH apparatus.

This type of readout system will provide a three-dimensional tracking of particles inside the apparatus with a time resolution of $\sim$ 1 ns and a spatial accuracy of $\sim$ 1 cm on both views.

In figure 3.6 the GSC plane arrangement is shown. The detector plane insertion is along the Y direction. The mechanical construction of the iron structure should not interfere with the detector installation. The dimension of the underground hall permits a maximal length of the detector module of $\sim$ 1.8 m to allow module insertion. In this case, each detector plane is composed by 16 *roads*, 1.80 m wide and 14.4 m long, realized with 8 *plate units* 1.80 m long (figure 3.6).

Two different pick-up strip solutions, described in the following subsections, are presently under investigation.

3.5.3 Flat cable strips

Commercial flat cables are used as pick-up elements instead of the usual copper strips. The measurements reported in section 3.9 have been performed with this innovative pick-up system [68, 3, 66]. Four Glass RPCs placed on the readout plane are shown in figure 3.7. This prototype consists in flat cables glued to a PCB fiberglass sheet coppered on one side. The pick-up strip width of 2.8 cm is determined by the Front End Electronics (FEE) cards. In fact, each channel input stage is connected to 22 short circuited flat cable conductors. The flat cable strips are connected to the LNGS card [70] using commercial wiremount socket connectors, as sketched in figure 3.8. Full custom shielded flat cables are under development by the LNGS and the 3M Corporation [71]. Presently, flat cable strips 30 m long 25 cm wide (i.e. 192 conductors) and 3 mm thick, have been realized. The characteristic impedance for the "22 conductors" (i.e. 2.8 cm) strips is about 12 Ω and the propagation constant is 5.7 ns.

Due to the flexibility of this approach, two pick-up layouts, which are being studied for MONOLITH, are described in the following. Sketches of the two configurations for one 15.0 $\times$ 14.5 m^2 module plane are shown in figure 3.9 (please note that for the sake of clarity only 4 roads instead of 8 are reported, as well as only 4 Glass RPC units for each road instead of 8).

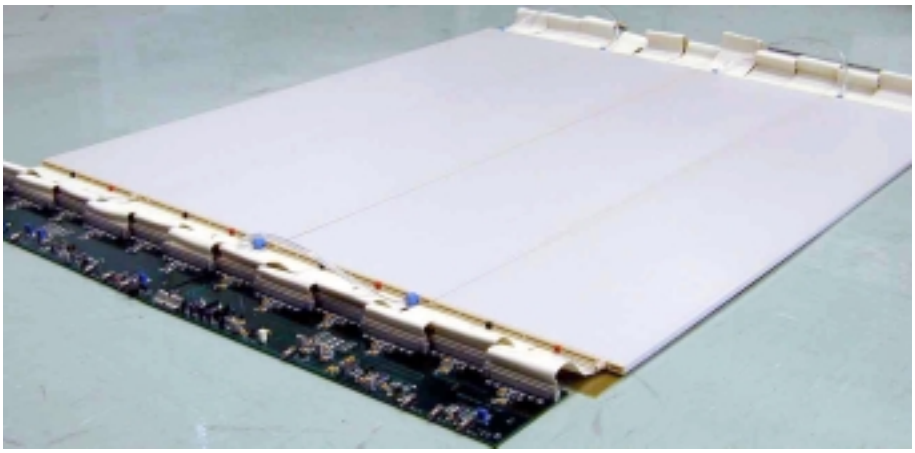

Figure 3.7: Picture of 4 Glass RPCs coupled to the readout plane.

The first configuration is shown in figure 3.9 a. The X coordinate readout system is based on 14.5 m long and 2.8 cm wide pick-up strips, faced to all 8 Glass RPC units along the road. The X-strips are connected to the FEE outside the apparatus. These FEE cards provide the digital strip pattern, the analog output and the fast digital output for time-of-flight measurement and triggering. The other end of the flat cable strips is terminated with 12 Ω to get a uniform response along the strips. The second coordinate cannot be read out by using long pick-up elements because of the mechanical constraints. Therefore, the readout system for the Y coordinate is based on a lay-out successfully used in the MACRO experiment [69]. For the MONOLITH apparatus, 1.8 $\times$ 1.8 m^2 readout planes are placed on the Glass RPC units as shown in figure 3.9a. The 1440 conductors of each readout plane are sent to interconnecting cards that rearrange the flat cable wires into 64 strips 2.8 cm wide. These cards are connected to a flat cable acting as a bus line for the analog signals. The bus line is thus composed by 64 signal + 64 ground flat cable conductors. The connection of the cards to the bus can be obtained by means of flat cables and wiremount socket connectors. With this configuration, signals coming from different 180 cm long strips along the same Y coordinate are sent to the same FEE channel by means of the bus line. The FEE Y cards provide the digital pattern of the Y strips. The other end of the

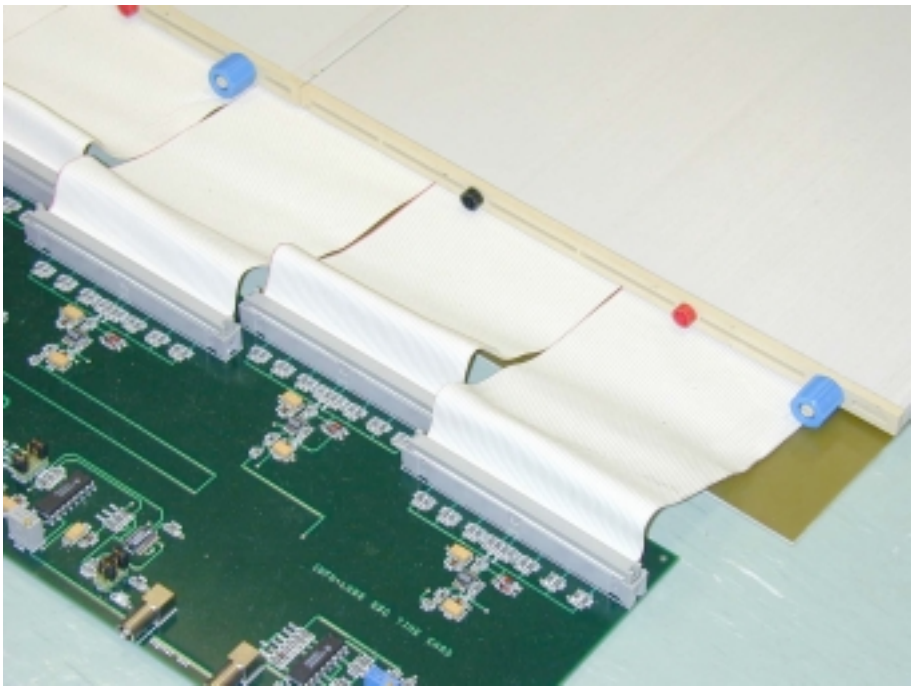

Figure 3.8: Magnification of the flat cable strip connection to the LNGS card.

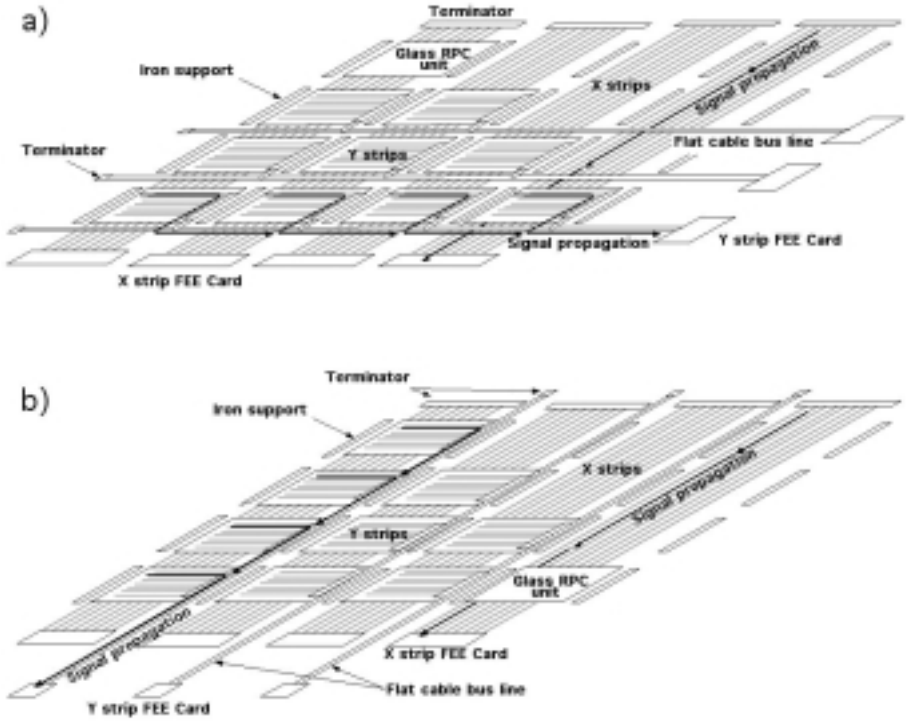

Figure 3.9: Sketch of two possible readout system configurations using the flat cable strips (see text for details).

bus line is properly terminated to get a uniform response.

The second possibility is shown in figure 3.9b. The X coordinate readout system is equal to the one described above while the bus lines send Y strips of the same road to the same FEE electronic channel, as shown in figure 3.9b. In this option, a time measurement is needed in order to know the Glass RPC unit crossed by the particle . If necessary, the separation in time of the pulses coming from different Glass RPC units can be easily increased, by increasing the bus line length and increasing the connection pitch of the Glass RPC units along the bus. The advantage of this option with respect to the previous one is that a decoupling between the iron structure assembling and the detector insertion is conceivable. In conclusion, the flat cable strip system presents the following important characteristics:

- No electronics inside the apparatus.
- Minimization of the number of FEE channels.
- No soldered elements inside the apparatus.

3.5.4 Self-supporting modular strip boards

The major advantage of this option is to allow the decoupling between the iron structure assembling and the detector insertion. In this scheme the GSCs are assembled one to each other in a plate unit of 1.8 x 1.8 m^2. The plate units are composed of 6 GSC detectors 0.3 x 1.8 m^2 equipped with X and Y strip readout (64 strips 2.8 cm pitch, see figure 3.10).

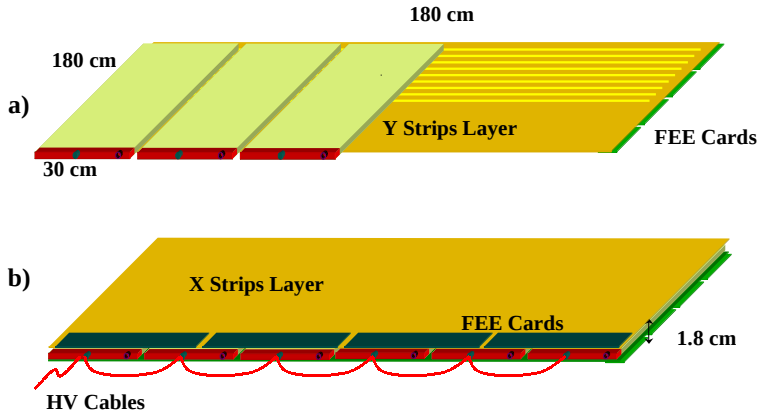

Figure 3.10: A plate unit is composed of 6 Glass RPCs 30x180 cm^2: a) the chambers are placed on top of the Y strip plane; b) the plate is completed by superposing the X strip plane. Both X and Y plane are equipped with Front End Electronic (FEE) cards.

The strip plane (see figure 3.11) is realized by gluing a grooved copper foil (35 μm thick) on one side of a plastic honeycomb support (3.5 mm thick). The strip ground is realized with a continuous copper sheet glued on the opposite side. With this choice the impedance of the strip line is about 50 Ω.

The 6 GSC detectors are coupled with the two honeycomb strips planes through a bi-adhesive tape resulting in a very stiff and self-supporting sandwich (see figure 3.10).

The front end electronics is mounted directly on the edge of each X and Y strip plane as shown in figure 3.12.

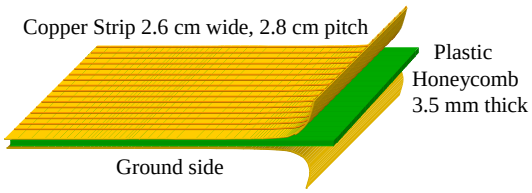

Figure 3.11: The grooved copper foil glued on the honeycomb support.

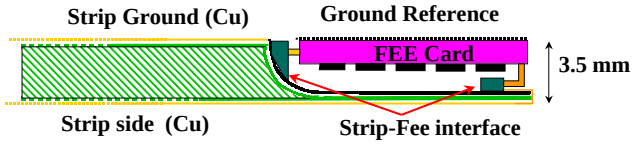

Figure 3.12: A detail of a plate with the electronic cards inserted on the couche of the strip plane.

The electronic cards (4 cards, 16 channels each for each view) are placed in a 4 cm wide couche realized by machining the edge of the strip plane on the ground side, without introducing any additional geometrical dead space and thickness. The variation of the strip impedance near the electronic card does not affect the operation of the strip itself. Indeed, the ground reference of the card takes the place of the strip ground, keeping the pickup efficiency unaffected.

Such a detector assembly defines the basic unit of the MONOLITH apparatus. Each plate is therefore supplied with:

6 gas inputs ;
6 gas outputs;
1 HV input;
2 fast digital signal outputs for timing and trigger purposes;
1 analog signal output ;
1 flat cable (16 wires each) for the X+Y digital strip pattern;

Eight basic units are connected one to each other to realize a 14.5 m long road through fast mechanical connections. Two GSC detectors belonging to contiguous plate units are connected through a double male gas fitting, as shown in figure 3.13 making 6 gas lines per road, 14.5 meters long. Each plate unit is powered with a High Voltage line that connects, through a daisy chain, the 6 GSCs for a total of 8 HV cables for each road.

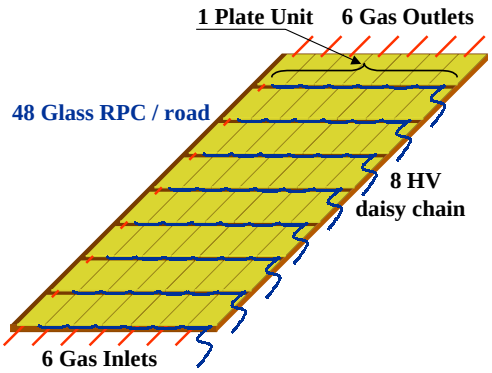

Figure 3.13: Each road is composed by 8 plate units supplied with 6 gas line and 8 HV cables.

The fast signal coming from the Y strips is used to perform timing measurements while the X one is used for trigger purposes. One HV channel (10 kV/1 mA) supplies 4 roads through a passive distributor.

Each detector plate is assembled and tested outside the cavern, without interference with the iron assembly that can proceed in parallel. The plates fully equipped with their electronics and cables are brought into the cavern and inserted inside the iron gap, one after the other, while making the gas and mechanical connections. In the hypothesis of 2 roads completed per day we estimate a total assembly time of about 2 years per super-module.

Cost and time estimates are presented in chapter 8.

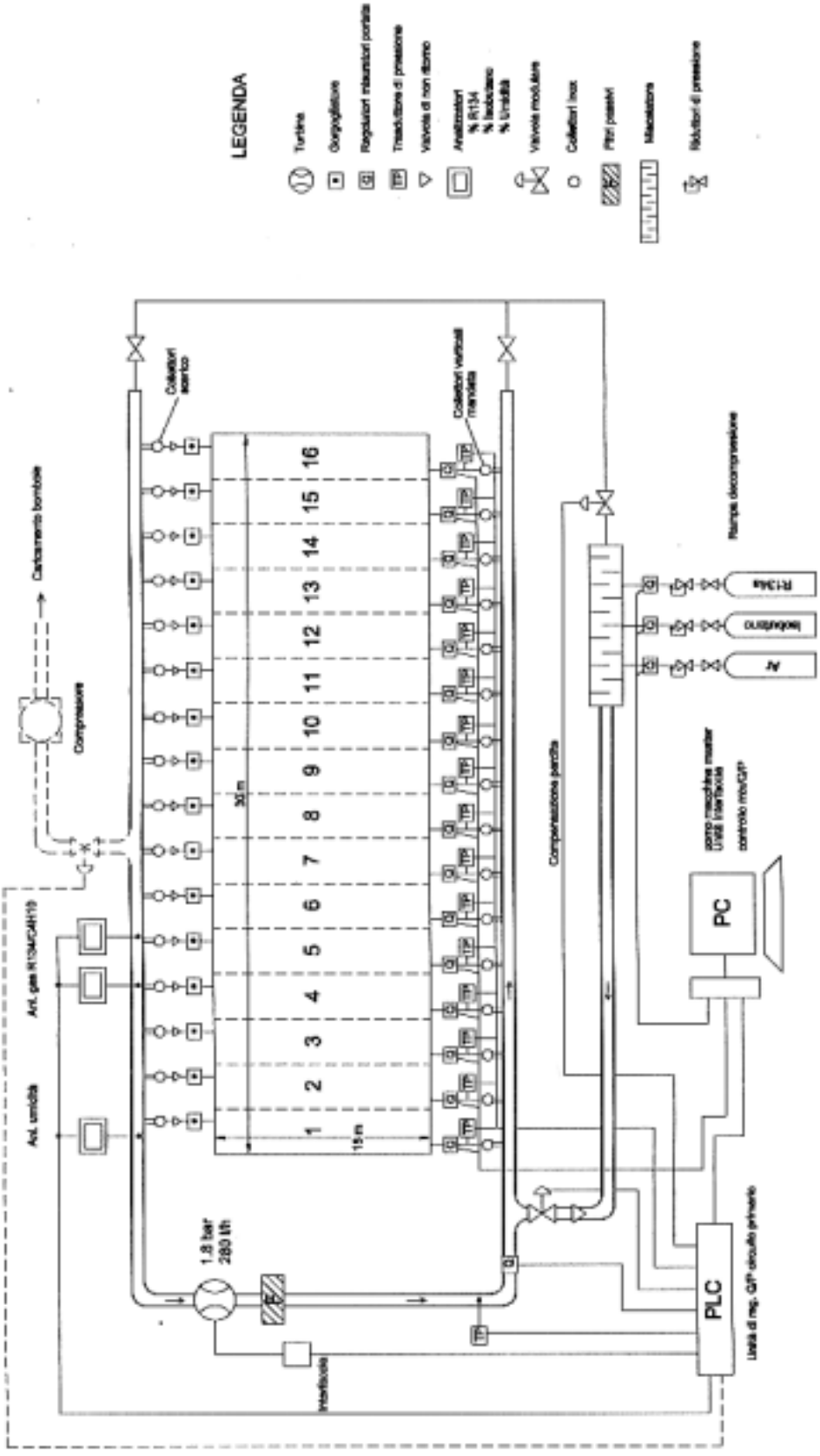

Figure 3.14: Schematic view of the MONOLITH Gas System.

3.6 Gas System

As shown in figure 3.14, the gas distribution system will be a recycling system that must ensure a flux corresponding to two detector volumes per day, i.e. 216,000 liters/day. The premixed gas (Argon 48%, Isobutane 4%, Freon R134A 48%), will circulate inside stainless steel tubes electrically cleaned. The whole apparatus will be divided into 16 x 10 = 160 detector groups, each of them being fluxed separately. The gas flow velocity is controlled for each group by means of a mass flow meter. The pressure difference of 1.8 bar between inlet and outlet manifold necessary to ensure a regular flow in each detector group will be ensured with a gas turbine. All systems will be controlled via a PC computer. The gas mixture will be fixed in the inlet stage by means of mass flow meters, and checked in the outlet stage by means of isobutane and freon gas analyzers. Humidity will also be measured. At the start of operations the air will be removed from each detector group and compressed into bottles to be emptied in open air.

3.7 The trigger system

The GSC signals are read out digitally. In addition, the signals of 16 or more channels are summed and sent to a TDC via a discriminator. These discriminator signals are also available for trigger purposes. As every spark provides both an x- and y-coordinate, the processing of only one coordinate is sufficient for triggering. This leads to about 9000 trigger channels for the flat cable design. A VME trigger board processes groups of 120 of these trigger channels with a programmable local trigger logic. This results in 76 VME boards for all trigger channels.

The logic allows to trigger on certain track patterns, such as 2 or 3 hit layers out of 5 consecutive layers. This results in a trigger efficiency near 100% for the relevant atmospheric neutrino events (energy > 1.5 GeV). Through a combination of signals from different trigger boards on an additional logic level, a global multiplicity trigger is also possible. The signals of the veto counters are read out by TDC's and are also available for trigger purposes.

The expected trigger rate (mainly originating from cosmic ray muons and random coincidences of radioactive decays) is expected to be much less than 1 Hz. The trigger initiates the readout of the digital and TDC information, which is collected and further processed via VME CPU modules. The complete events are then fed into an online computer, which performs a preliminary event reconstruction. At this "2nd level trigger" stage, events can be filtered and/or distributed to several output streams.

3.8 The DAQ system

The MONOLITH DAQ system will be VME based.

DAQ electronics will be located on the top of the detector, along the hall axis in 4 points (spaced ~ 7.5 m), two for each detector module.

Since VME crates and their read-out are the major DAQ cost, a big effort has to be done to minimize their number: STAS (control and readout) units serving 32 digital chains will be developed (the current commercial STASs serve 8 digital chains) and 64 chs/unit TDC modules will be used.

In this way every DAQ station will provide the readout of 4 roads (16 digital chains and 32 TDC channels) for all the 120 detector layers. The 60 STAS and TDC modules needed will be stored in 6 crates (3 9U and 3 6U). Every crate will serve 40 layers. In every DAQ point 2 VME crates devoted to trigger and slow control systems are foreseen.

Front end data read-out will be performed using Motorola MVME CPUs. To minimize software cost, the Linux option, as operating system of VME embedded CPUs, will be investigated.

Disk-less CPU booting, event building and monitoring will be performed using a Linux PC for each DAQ station.

3.9 Detector performance

The measurements reported here have been performed with a prototype made of 20 iron plates (100×100 cm^2) 5 cm thick, 2 cm apart, interleaved with 20 detector planes.

The readout system, developed at the LNGS, is based on the use of halogen-free flat cables acting as pick-up strips (see section 3.5.3for more details). The strips are coupled to the detector plane and are referred to ground by means of a 100×100 cm^2 FR4 vetronite foil acting as a shield. The other side of the detector plane faces a 100×100 cm^2 aluminum sheet referred to ground. The digital readout system of the ALEPH hadron calorimeter has been used for the event pattern in one view. The flat cables are connected on one side to the front end discriminators to obtain 96 1 cm wide strips. The other side is connected to cards developed at LNGS that perform charge and time measurements. The Glass RPCs are operated with an Argon + isobutane + R134A = 48% + 4% + 48% gas mixture and the applied voltage is 8.2 kV. The above described prototype module has been exposed on CERN PS T7 beam and used for a test on up/down discrimination. Results are reported in the following sections and in ref. [3],[68].

3.9.1 The CERN PS beam test

A test of the MONOLITH prototype has been performed on the CERN PS T7 beam facility to study the hadronic energy resolution and the reconstruction capability of the shower direction. This beam provides particles (mainly pions) in the range between 2 and 10 GeV. Figure 3.15 shows the typical pattern for a 4 GeV pion taken from the online event display.

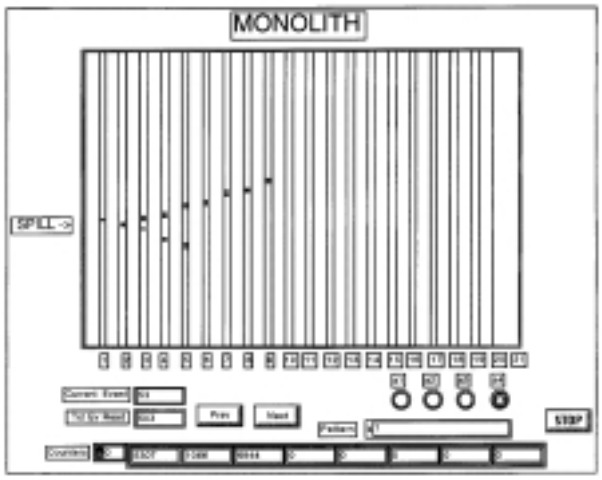

Figure 3.15: 4 GeV pion interacting in the 8 ton calorimeter prototype.

The shower energy can be measured by hit counting, because the hit number is proportional to the total track length and therefore to the energy released. The mean number of hits produced by pions as a function of the energy is given in figure 3.17; no saturation effects were found in the investigated energy range and a calibration value of 4.4 hits/GeV was obtained. As shown in figure 3.18 the energy resolution can be parameterized as $68\%/\sqrt{\mathrm{E(GeV)}}$ +2%. The shower resolution for different sampling densities was obtained offline by appropriately selecting

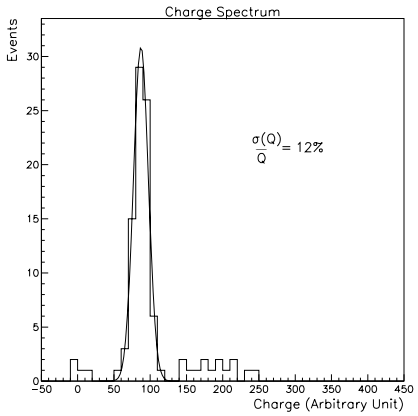

Figure 3.16: Induced charge distribution for 10 GeV muons crossing a plane.

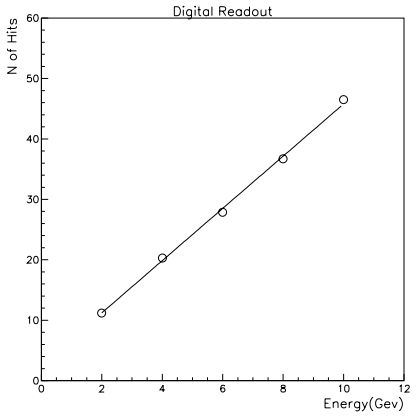

Figure 3.17: Digital response for pions.

the detector planes. Figure 3.19 shows that the resolution is better than $100\%/\sqrt{\mathrm{E(GeV)}}$ up to a shower sampling of 20 cm of iron. In the MONOLITH detector, 20 cm sampling corresponds to showers developing at a 66^0 zenith angle.

It is worth observing that, in a digital calorimeter, a good linearity and resolution is possible only if the probability to have more than one track on the same strip is negligible. A high track density (due to high energy and/or e.m showers) determines a loss of linearity with the worsening of the resolution. The same effect occurs when using wide pick-up strips.
For what concerns the analog readout, the total charge is proportional to the total number of streamers and therefore to the total track length. Thus the charge collected can be used to measure the energy released by the shower. The energy resolution obtained with the analog readout follows a $96\%/\sqrt{\mathrm{E(GeV)}}$ law. It is worse than expected mainly because the analog method strongly depends on the precision of the coupling between pick-up and detector planes, while the intrinsic charge spread of the single streamer (see figure 3.16) gives a negligible effect on the resolution.

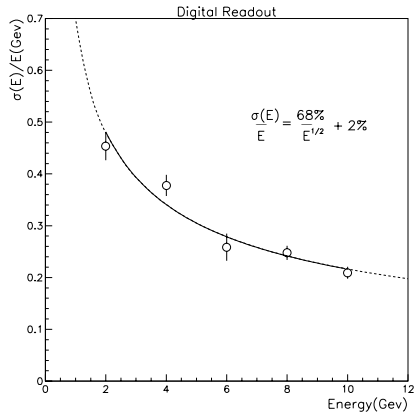

Figure 3.18: Digital resolution for pions.

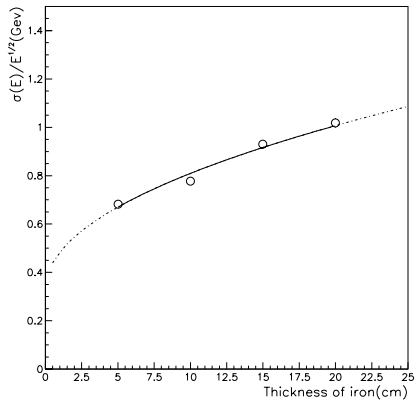

Figure 3.19: Digital hadronic resolution as a function of the iron thickness.

In conclusion, the digital readout is weakly dependent on the working conditions, but it suffers effects of saturation at high track density. On the contrary, the analog readout is linear up to higher energies, but presents more difficulties when used in a large apparatus (gas mixture stability, precision in construction, etc.).

3.9.2 The test for up/down discrimination

A second test was performed on the prototype at the Laboratori Nazionali del Gran Sasso to study its time of flight performances. Vertical through-going muons are selected with two scintillators defining the acquisition trigger. Events are reconstructed in one view by using 1 cm pick up strips. The prompt signal of the even planes is recorded for the time-of-flight measurement, while all planes are used for tracking the crossing particles. Results of one month of data taking are reported.

The efficiency of one plane as a function of the strip position, measured with the digital cards, is shown in figure 3.20. The efficiency along the muon tracks has been calculated considering hits within 3 cm from the straight line fit. The drop every 25 cm is due to the geometrical dead

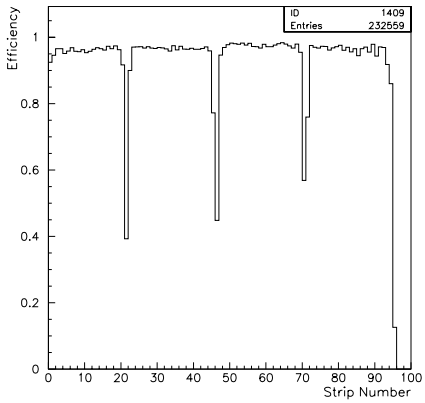

Figure 3.20: Efficiency of a plane as a function of the strip number.

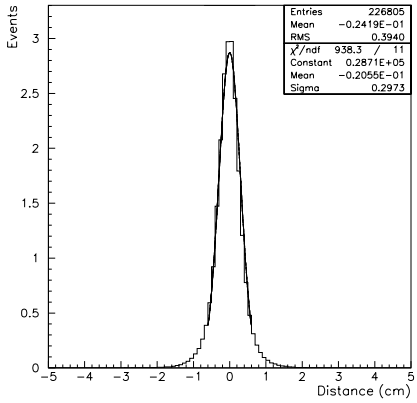

Figure 3.21: Distribution of the distance between the center of the cluster in the even planes and the track reconstructed with the odd planes.

zone between adjacent detectors. The dead area inferred from the plot is about 7 mm wide, in agreement with the mechanical characteristics of the Glass RPC prototypes (glass width is 243 mm, while the envelope one is 250 mm). Far from the chamber edges, the measured efficiency is about 97%, including the $\approx 1\%$ geometrical inefficiency due to the spacer sticks. The average plane efficiency is thus 94%. We are confident that this value can be increased by improving the mechanical tolerance of detector components and readout electronics. To measure the spatial resolution we used the distance between the hit position (e.g. the center of the cluster) and the muon impact point reconstructed with a straight line fit. The resolution has been calculated for even planes, while odd planes are used for track reconstruction. The obtained distribution is reported in figure 3.21; the Gaussian fit has a σ resolution of 3 mm. The tails are mainly due to multiple scattering of the crossing cosmic ray muons.
Figure 3.22 shows the time difference distribution of the signals coming from two planes crossed by the same particle. Assuming that the two planes have the same time resolution, the RMS of each plane turns out to be 1.3 ns. The distribution is not Gaussian because of the tails due

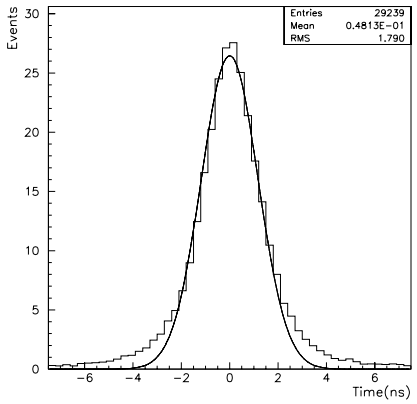

Figure 3.22: Distribution of the time difference between two planes.

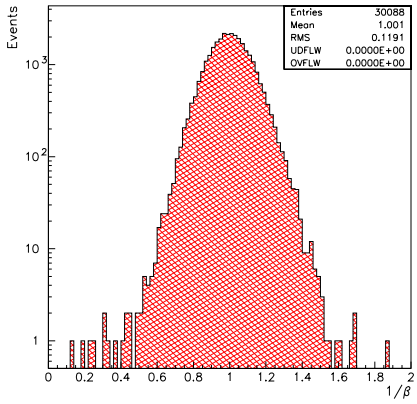

Figure 3.23: $1/\beta$ distribution for tracks 4.0 m long.

to the delayed signals, which make up about 10% of the total events. All planes show the same time resolution, stable over one month measurement period. Measurements to test long term stability are in progress.

A full discussion of the use of results of this test in the estimate of the up/down discrimination of MONOLITH is reported in chapter 4.

During the test a first estimate of the up/down discrimination on 4 m long tracks (the minimum length required for partly-contained muons in the physics analysis) was obtained as follows.

An algorithm was developed which discards *bad hits* and fits the time measurements of each plane with a straight line in the t-z plane:

$$t(z) = \frac{1}{\beta} z + c \qquad z = \textit{vertical coordinate of plane}, \qquad \beta = v/c$$

With our sample of about 30000 cosmic rays crossing the whole prototype for a total length of 1.4 m, we obtained a $1/\beta$ distribution with 0.28 % of the events in the negative region. The extrapolation to a track length of 4.0 m produces no events in the negative $1/\beta$ region, as shown

in figure 3.23.

Chapter 4

Experiment simulation and performance

4.1 Detector simulation

The simulations described in this chapter were performed before some of the technical details of the detector were finally adjusted (changes at the level of a few %, e.g. exact external dimensions). The simulated detector is therefore at slight variance with respect to chapters 3 and 8. These small differences result in negligible effects on the performance. The reader should also be aware that a different coordinate system is used here.

The simulation of the detector is based on the GEANT package [73]. A detailed description of the detector geometry with dead zones, of the detector media and of the the magnetic field configuration has been implemented. The GEANT package has then been used to follow particle propagation through and interactions with the detector media. An approximate description of the digitisation process is implemented, based on the present knowledge of the behaviour of the active elements of the detector (Glass Spark Chambers).

In the experiment simulation, the detector consists of a stack of 121 horizontal iron planes 8 cm thick and 15×30 m^2 surface, interleaved by 120 planes of sensitive elements. The detector is divided in two super-modules of 15×15 m^2 surface, resulting in a mass of about 17 kt each. The iron planes of each super-module are magnetised as shown schematically in figure 4.1 (see appendix A for details). A detailed description of the field map is implemented in the simulation. Simulations at different field strength have been performed. The results discussed hereafter are referred to an average magnetic induction of 1.3 T. The optimisation of the magnetic field strength is discussed appendix A.

The sensitive elements for tracking and timing (Glass Spark Chambers) are assumed to be housed in a 20 mm gap between the iron planes. The GSC are described as made of 18 mm of material with an average density of 1 g/cm^3 (water) and a gas gap of 2 mm (active element) in their center. Orthogonal readout strips of 30 mm pitch placed on both sides of the chambers provide the X and Y coordinates of the event, the Z coordinate being identified by the layer number[1]. The X and Y strips are supposed to be continuous in each super-module all along the X (15 m) and Y (15+15 m) directions, without any longitudinal segmentation. This choice corresponds to the most conservative option among the ones considered for signal readout.

The description of detector inefficiencies and time response is important in the evaluation of the experiment sensitivity and, particularly, of the rejection power against externally produced background events entering the detector.

In order to account for iron supports of layers and coil housings, dead zones 30 mm wide at

[1] In the MONOLITH reference system, Y is along the Hall axis.

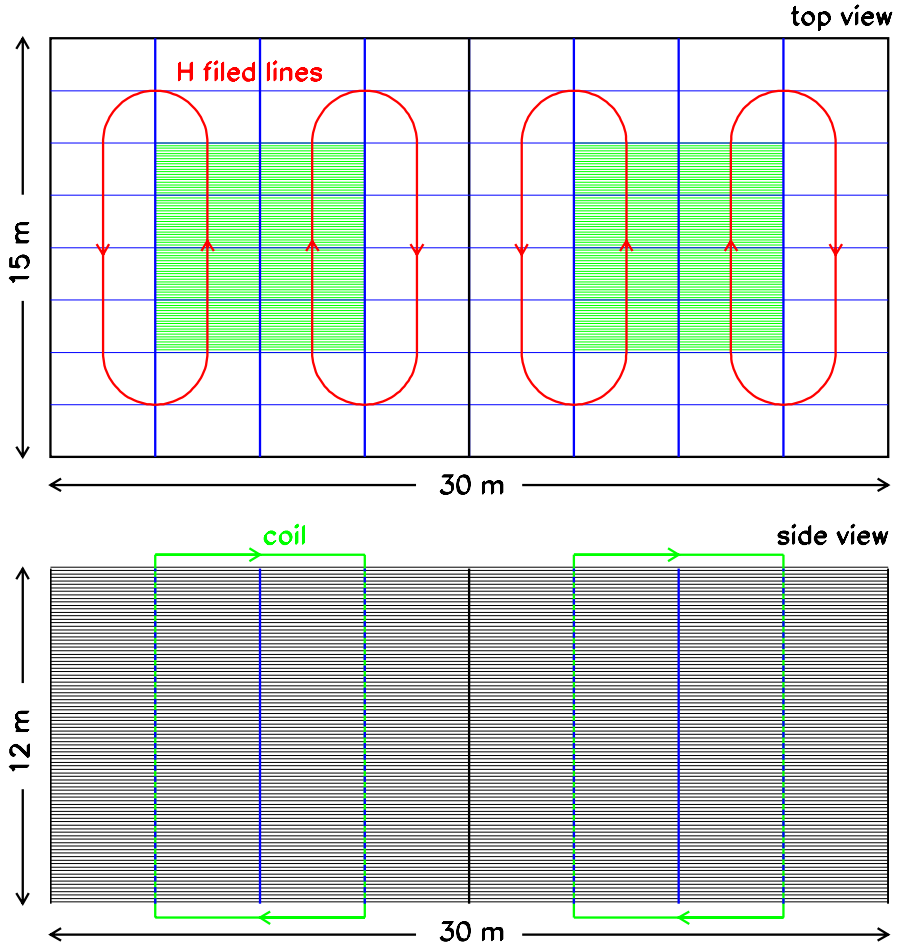

Figure 4.1: Simplified view of MONOLITH showing the magnetisation scheme: the shaded area in the top view represents the coil and lines represent dead zones due to iron supports of layers, coil housings and chamber modularity (see text).

the edges of the super-modules along the Y direction and 60 mm wide every 3750 mm along Y (see figure), are simulated. In these regions, the gap between two adjacent iron planes is filled with iron, while the detailed structure of the coil is not simulated. Additional dead regions related to the chamber structure and modularity are described as 30 mm dead every 1875 mm along X and 5 mm dead every 250 mm along Y. Chambers in the uppermost four layers, which are used as a veto against incoming muons (see below), are staggered along X, to prevent the 30 mm wide dead regions from being vertically aligned.

A part from these dead zones, the GSC are assumed to be evenly efficient. They are described by a lattice of 3×3 cm^2 elementary cells, corresponding to the readout pitch of the detector, in which sparks can be generated by ionising tracks. The signal induced on the readout strips by these sparks is collected assuming, as a rough approximation, that only the strips in front of the spark are fired and that there is no induction on the nearby strips. A digital readout of the strips is considered.

The time response of the detector is simulated as follows: the arrival time of each individual spark is smeared according to a set of resolution functions, giving a conservative representation of the results obtained in the test of the Baby-Monolith prototype on cosmic rays (see figure 4.2). These resolution functions have been measured in Baby-Monolith after selection of almost vertical muons and are therefore suited to describe the time spread of single sparks. The time distribution sampled is randomly chosen and the relative offset between the different TDC channels is calibrated to zero in the simulation. This is achievable in MONOLITH using cosmic muons crossing the detector. It is moreover assumed that only the time information relative to the hit with the earliest arrival time (including resolution effects) is recorded in each layer, i.e. only one TDC channel per layer is assumed in the simulation (120 TDC channels in total).

4.2 Event reconstruction

4.2.1 Muon reconstruction

At the reconstruction stage, the muon direction is obtained by a best fit procedure to the muon track, which accounts for effects of detector resolution, multiple scattering, energy loss along the track and magnetic field. The muon energy is mainly determined by range for stopping muons and by track curvature for outgoing muons.

The procedure is based on the work discussed in ref. [78]. Z is used as independent coordinate and a best fit of the track to hits recorded in the XZ and YZ independent projections is performed. Track parameters $\{X_0, Y_0, dX/dZ_0, dY/dZ_0, 1/p_0\}$ giving the X and Y coordinates, the directions on the XZ and YZ planes and the muon momentum at the vertex are determined after an iterative χ^2-minimisation. The flight direction of the muon is known from time of flight measurements along the track (see section 4.2.3) and the position of the track vertex along Z is fixed at the first layer fired along the flight direction. No pattern recognition is applied yet and muon hits are taken from the simulation truth. The χ^2 function is defined as:

$$\chi^2 = \sum_{i=1}^{N}\sum_{j=1}^{N}(x_i^{track} - x_i^{meas})w_{ij}(x_j^{track} - x_j^{meas}) + (y_i^{track} - y_i^{meas})w_{ij}(y_j^{track} - y_j^{meas}) \qquad (4.1)$$

where the labels "*track*" and "*meas*" indicate the expected and the measured positions along the track, while w_{ij} are elements of the weight matrix which include measurement errors and multiple scattering effects in the diagonal elements and correlations due to multiple scattering in off-diagonal elements. The multiple scattering contribution is estimated at each step along the track and depends on the local momentum and angle to the iron layers of the track[2]. Details

[2]Correlations between the two projections, also due to multiple scattering, are neglected.

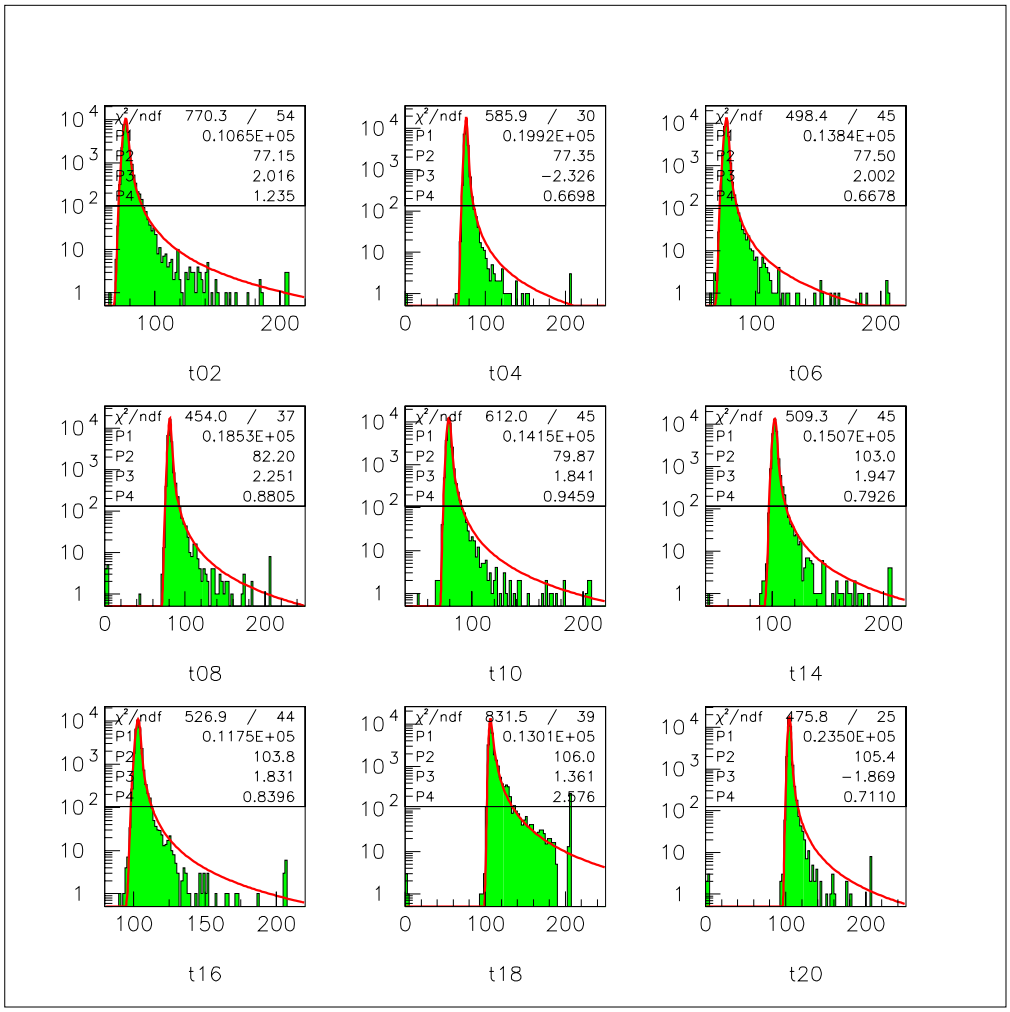

Figure 4.2: Resolution functions measured with the Baby-Monolith prototype (histograms) and sampled in the simulation (continuous lines). The continuous lines are best-fits to data assuming a Gauss distribution on the left sideof the peak and a Cauchy on the right side: P3 (P4) is the sigma (HWHM) of the Gauss (Cauchy) distribution in nanoseconds. The relative offset in the TDC was calibrated to zero in the simulation.

on the computation of these weights may be found in ref. [78]. The expected trajectory of the track as a function of track parameters at the vertex is calculated using the GEANT libraries.

At present two separate procedures are used to measure the momentum of contained and semi-contained muons. For contained muons, the module of the momentum $|p_0|$ is determined from the measurement of the range alone, while the muon direction is obtained from a track fit with four free parameters $\{X_0, Y_0, dX/dZ_0, dY/dZ_0\}$, being $1/p_0$ fixed from the range. For semi-contained muons, a complete five-parameters fit is performed, with a lower bound on the estimated momentum set by the track range observed in the detetctor. The track-fitting also provides an estimate of parameter errors.

The optimisation of the track-fitting procedure is still in progress. In particular, no special treatment is yet implemented for tracks bent by the magnetic field to cross more than once the same layer. This mainly occurs for low-energy muons near the horizon, which have their momentum underestimated by the present track-fitting procedure. However, these muons are of marginal interest in the measurement of the oscillation pattern – and indeed mostly rejected in the anlysis of atmospheric neutrino events – since near the horizon and at small energies the L resolution is poor (see discussion in section 3.1). On the other hand, events induced by neutrinos from the CNGS beam are mainly developed along the horizontal direction and requires a special treatment. On these events, an approach to the track fitting similar to the one discussed here, but working on the ZY and XY projections, has been introduced (see chapter 6 for details). An upgrade of the procedure with a 3-D reconstruction of the tracks is under way.

The energy resolution on the sample of stopping muons produced by ν_μ-CC interaction is on average better than 6%, with the sole quality request that the muon track span at least seven layers. With this same selection and the additional request – explained in section 4.3.2 – that the track length inside the calorimeter be larger than 4 m, the average resolution on outgoing muons is found to be $\sigma(1/p)/(1/p) \simeq 22\%$ at H = 1.3 T, essentially limited by multiple scattering in iron. An improved resolution is achieved at higher field intensity. The dependence of the momentum resolution on the track length, the pitch angle to the field and the strength of the magnetic induction has been found to agree with expectations.

From the analysis of the track curvature, the identification of the muon charge is possible. Due to the field configuration the charge identification is best achieved near the vertical direction, perpendicular to the field lines. On average 95% of the muons with a track length of at least seven layers have their charge correctly assigned. For very long tracks, as they occur for upward throughgoing muons (typically about 12 m) charge discrimination is better, and momenta can be measured up to several hundred GeV. For specific studies, charge discrimination could be significantly improved by selecting only unambigous candidates.

The direction of the muon at the vertex, from which the neutrino direction is estimated, is reconstructed with an average resolution of about 10 mrad. This has a negligible effect on the resolution on the neutrino direction, which is limited by the μ-ν scattering angle (see below).

4.2.2 Hadron reconstruction

The hadronic energy is estimated from the hit multiplicity in the calorimeter (digital information). The detector has a coarse hadronic energy resolution and, at low energies, a limited capability of reconstructing the hadronic energy flow. According to the simulation the dependence of the energy resolution on the hadronic energy can be parametrised as $\sigma(E)/E = 90\%/\sqrt{E\ (\mathrm{GeV})} \oplus 30\%$, averaged over all shower directions. This is shown in figure 4.3, together with the calibration curve of the hadronic energy response obtained form a sample of simulated neutrino events. As explained by equation (3.2) of Chapter 3 and discussed in the next section, the overall resolution on the neutrino energy, which enters in the measurement of the L/E and is generally dominated by the fluctuations in the hadronic shower, can be controlled by proper

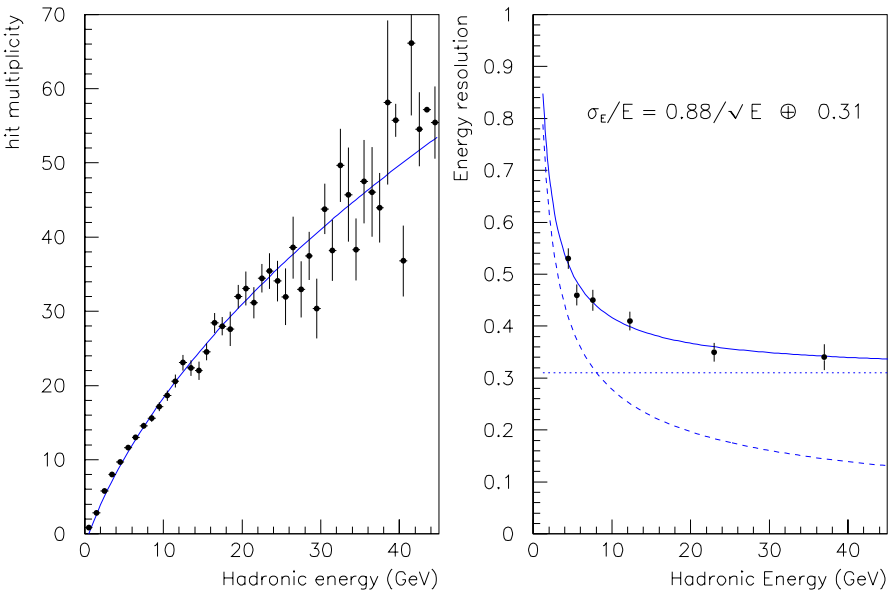

Figure 4.3: Hit multiplicity and energy resolution averaged over all shower directions as a function of the hadronic energy in atmospheric ν_μ-CC events.

selection criteria, related to the in-elasticity of the event.

The reliability of this simulation of the MONOLITH response to hadrons depends on the description of hadronic interactions embodied in the GEANT package and on the assumption made in the description of the digitisation at the readout stage. This is being studied by comparing the results on hadronic energy resolution obtained with the MONOLITH prototype (Baby-Monolith) exposed to test beams during July/August 1999 (see section 3.4.3 and ref. [3]) to the results of a GEANT simulation of Baby-Monolith. A direct comparison to MONOLITH has not been possible since Baby-Monolith had a geometry somewhat different from MONOLITH: the 20 iron planes were 5 cm thick, the readout strip were only on one side of the chambers and had a pitch of 1 cm. A part form these differences in the detector layout, the simulation is run under the same assumptions adopted in the description of MONOLITH: a digital readout of the fired strips is considered, without induction on adjacent strips. Preliminary results show that the simulation of Baby-Monolith predicts a lower average multiplicity and a worse resolution than the ones measured with test beam data. These differences can be ascribed to the simplified model adopted, since induction on nearby strips is expected to linearise the detector response and improve resolution. A detailed study is under progress and will also benefit from new test beam data. An extrapolation to MONOLITH of the results of this comparison is not straightforward, due to the different geometries and readout-strip pitch of the two detectors. Nonetheless, this study corroborates our expectation that our neglecting of induction results in a conservative description of the energy response of MONOLITH to hadrons.

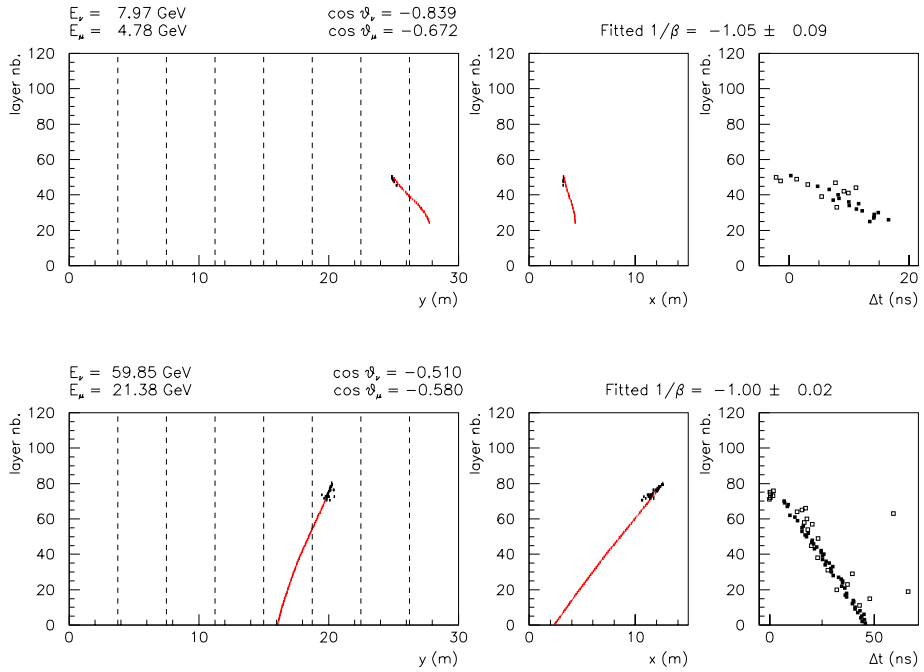

Figure 4.4: Display of fully contained (*top*) and partially contained (*bottom*) high-energy events induced by atmospheric muon neutrino interactions. From left to right the YZ, XZ and TZ view are shown. On the TZ view, black (white) hits are retained (rejected) by the time-of-flight fitting procedure.

4.2.3 Identification of the flight direction

By taking advantage of the timing capabilities of the sensitive detectors (of order 1 ns), the flight direction is determined in each event from a least-square fit of the timing in each layer versus the layer number.

An "event length" as a function of Z (layer coordinate) is reconstructed by combining the hits in the XZ and YZ projections. A least-square fit of a straight line to the time-of-flight recorded in each layer as a function of the "event length" up to that layer is then performed, from which $1/\beta$ is determined. Positive (negative) values of $1/\beta$ indicate down-going (up-going) events.

In order to filter "out-of-time" hits, occurring in the tails of the resolution function (see figure 4.2), which could bias the estimate of $1/\beta$, a pre-selection of the layers to enter the fit is applied, by comparing the time difference among layers to the differences expected for $\beta = 1$ particles. Moreover, the least-square fit is performed iteratively and layers giving the largest contribution to the χ^2 are trimmed. This procedure stops when either a χ^2 probability larger than 5% is found or less than 80% of the pre-selected layers are retained.

This procedure, although developed on isolated tracks, is applied to all events without any prior pattern recognition. The performance and the limitations of this algorithm on the ν_μ-CC and on the cosmic muon samples are discussed below. Two examples of ν_μ-CC events are shown in figure 4.4.

4.3 Atmospheric neutrino event studies

In this section, only the reconstruction and performance on ν_μ-CC events induced by atmospheric muon neutrinos inside MONOLITH is addressed. The MONOLITH capability to detect a clear oscillation pattern will rely on these events. A discussion of the background sources to ν_μ-CC events is given in section 4.4. The performance of MONOLITH on other samples of events, also relevant for the experimental programme (muon-less events and up-going muons induced by up-going neutrino interactions in the Earth) will be described in the presentation of the MONOLITH sensitivity (see next Chapter). The performance on the CNGS beam is addressed in Chapter 6.

4.3.1 Event generator

Neutrino interactions in iron have been kindly provided by G. Battistoni and P. Lipari: the differential distribution of the atmospheric neutrino fluxes at Gran Sasso is described by the Bartol model [74]; neutrino interactions are calculated with GRV94 parton distributions [75] with explicit inclusion of the contribution of quasi-elastic scattering and of single pion production to the neutrino cross-sections [76]. The height of production of neutrinos in the atmosphere, relevant in the evaluation of the L/E resolution is parameterised according to Bartol model calculation as in ref. [77].

The Bartol model, similarly to the simulation of Honda et al. [79] used by the SK collaboration, assumes that atmospheric neutrinos produced in the cascade process are collinear with the parent cosmic ray particle. This 1-D approach is expected to be valid in the limit of high energies. Recently, efforts in improving the calculations of atmospheric neutrino fluxes have been made by several authors, in particular introducing full 3-D calculations of the neutrino fluxes [80, 81]. These simulations show that the main features of the neutrino fluxes at high energy are reproduced by the collinear approximation. All the differences are mainly located near the horizon and below 3 GeV [82], where the acceptance of MONOLITH is purposely limited (see discussion in sections 3.1 and 4.3.2).

Besides these computational approximations, uncertainties on the neutrino fluxes are related to our ignorance of the hadronic interactions and of the spectra and compositions of primary cosmic rays. However, as we shall discuss in the next chapter, an up/down symmetry in the high-energy neutrino fluxes follows from geometry and isotropy of flux of parent cosmic rays [83, 84]. This is exploited by MONOLITH to perform measurements with the *near* and *far* source comparison technique, which is therefore to a large extent independent of predictions atmospheric neutrinos event rates.

4.3.2 ν_μ-CC interactions: selections and performance

The selection of a pure and "high resolution" sample of ν_μ-CC events induced by atmospheric neutrinos is crucial to enable MONOLITH to detect a clear oscillation pattern. Moreover, since oscillation parameters are not precisely known *a priori*, a unique set of event selections and a unique analysis method have been defined in order to make the oscillation pattern detectable for every possible experimental outcome.

In order to select a pure ν_μ charged current sample, only events with a reconstructed track corresponding to a muon of at least 1.5 GeV are retained in the analysis. This energy cut also ensures a good up/down symmetry in absence of oscillations. In order to reject – in a real experiment – the background due to incoming cosmic ray muons, a further selection requires the events to be either fully contained in a fiducial volume, corresponding to about 87% of the detector and defined by requiring no hits in the first/last 4 layers and no hits in the first/last 10 strips in X and Y, or to have a single outgoing track (muon) with a reconstructed range

greater than 4 metres. For partially contained events, the requirement of a track length of at least 4 m corresponds to an up/down separation of about 10^{-6} for 2 ns timing resolution, which should be sufficient to guarantee the rejection of the residual cosmic muon background in the Gran Sasso laboratory. The combination of these selections results in efficiency of about 75% and practically energy independent, corresponding to an effective fiducial mass of about 26 kt. It reduces the contamination of ν_e and ν_μ-NC events in the sample of ν_μ-CC events below 1% and removes the bulk of cosmic muon background events. The remaining background is due to muons entering MONOLITH through detector dead zones and can be suppressed by specific selections based on the event topology and/or by an external veto (see section 4.4 for a detailed discussion).

In addition, in both fully and partially contained samples, the muon is required to hit at least seven layers. This selection has been optimised to guarantee a good performance of the reconstruction programme and remove muons very near to the horizon, whose L/E resolution is poor.

Further selections, based on the quality of the muon track fit and on event kinematics, are then applied in order to guarantee that the final sample has the required L/E resolution (better than 50% Full Width Half Maximum (FWHM)) over the whole L/E range. These selections have been tuned according to the discussion given in Chapter 3 (see equations 3.1 and 3.2) and essentially consist in a tight requirement on the estimated precision in the reconstruction of the incoming neutrino direction. At low muon energies only events of small in-elasticity and far from the horizon are retained, while for large muon energies deep-inelastic events even rather near to the horizon can be selected. For contained events, and given the detector characteristics, this is achieved by requiring $y \tan^2\theta_\nu < 0.75 E_\nu$, where $y = E_h/E_\nu$, θ_ν and E_ν are the interaction in-elasticity, the zenith angle and the energy of the neutrino. The sample of events with outgoing muons is populated by events of high energy, thus the only requirement is that the energy of the muon be estimated from the track fit with a relative error smaller than 30%. The MONOLITH performance on the events surviving these selections is shown in figure 4.5. The average angular resolution on the neutrino direction is about 11 (4.5) degrees for contained (semi-contained) events and is dominated by the μ–ν scattering angle; the energy resolution is around 20% (27%) for contained (semi-contained) events. The resulting L/E resolution is about 50% FWHM in both samples, with an asymmetric tail, which should be ascribed to the nonlinear relation between L and θ_ν.

Altogether, these selections reduce the charged-current interaction rate of "unoscillated" down-going muon neutrinos to around 7.8 per kt y, about 20% of which is due to partially contained neutrino events. The impact of the magnetisation of MONOLITH, which allows to reconstruct events with an outgoing muon, is best evaluated from figure 4.6, showing the overall selection efficiency as a function of L/E. The gain in acceptance at small L/E is noteworthy: the magnetic field increases the MONOLITH efficiency by more than 50% in the region where the first semi-period of the oscillation is expected, according to the most recent Super-Kamiokande reports. The detection of the oscillation minimum and the precision on Δm^2 mainly rely on the available statistics in this region.

The event rate expected in MONOLITH and the effect of the selection criteria discussed are summarised in table 4.3.2. A summary of the efficiencies and resolutions as a function of the neutrino energy is given in figure 4.7. MONOLITH will have an effective threshold on atmospheric ν_μ charged current events around 3 GeV and a practically constant efficiency of about 50% (including selection and fiducial cuts) up to high energies. The L/E resolution is independent of the neutrino energy and is dominated by the angular resolution on the neutrino direction at small neutrino energies and by the energy resolution at high energies.

The same figure also shows the MONOLITH capability to identify the leptonic charge of the neutrino, from the measurement of the muon sign in the magnetic spectrometer, and the

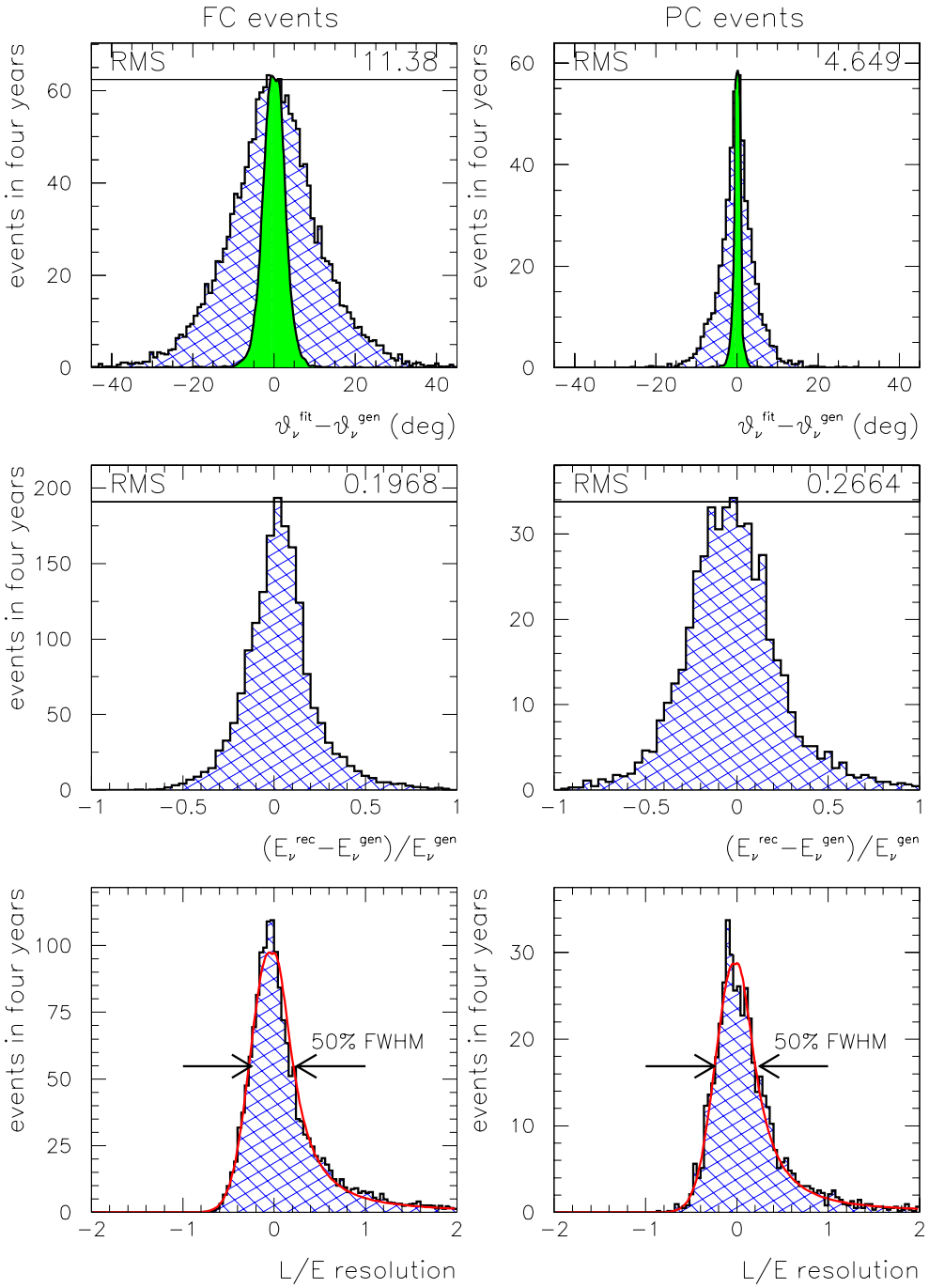

Figure 4.5: *Top:* Resolution on the neutrino zenith angle for contained (left) and partially contained (right) events after the selections discussed in the text. The dark histogram superimposed shows the contribution to the resolution on the neutrino zenith angle due to the precision of the muon track fit: the precision on the neutrino angle is dominated by kinematic effects. *Middle:* Neutrino energy resolution on contained (left) and partially contained (right) events selected. *Bottom:* L/E resolution for contained (left) and partially contained (right) events.

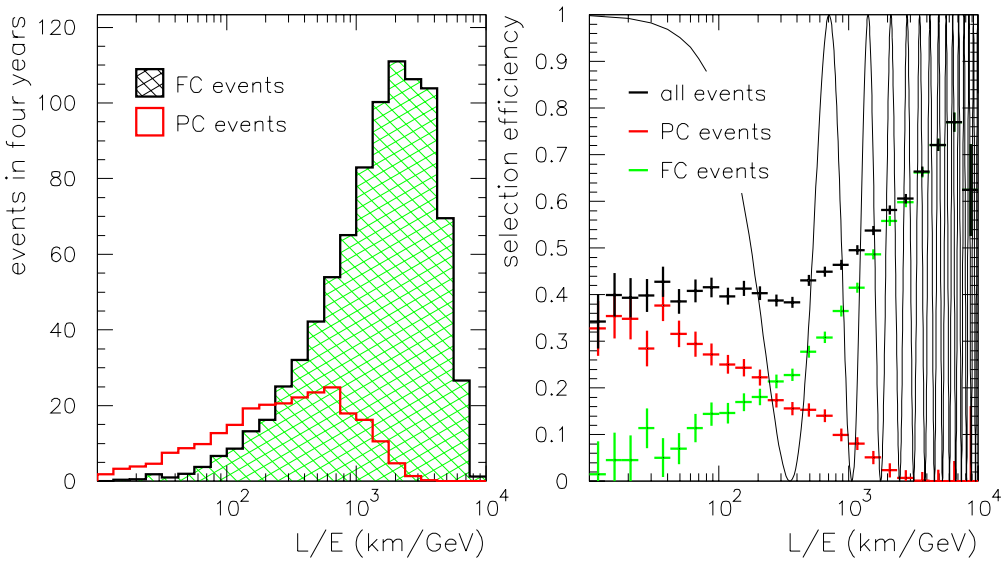

Figure 4.6: *Left:* L/E spectra of fully contained (FC) and partially contained (PC) events surviving the selection discussed in the text. *Right:* Overall selection efficiency and selection efficiency to fully contained and partially contained events as a function of L/E. The ν_μ survival probability for $\Delta m^2 = 3.5 \times 10^{-3}$ eV^2, the present best-fit value of Super-Kamiokande [41], is superimposed.

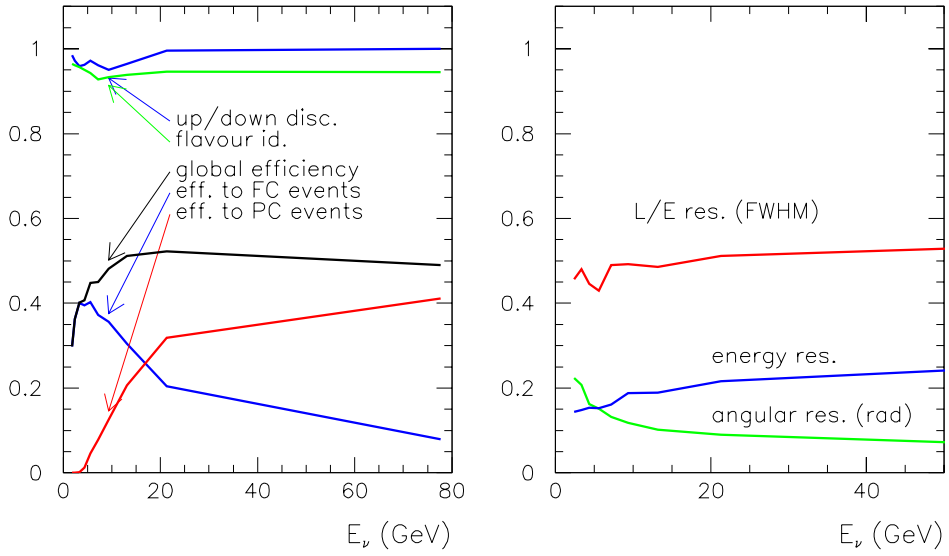

Figure 4.7: *Left:* Overall selection efficiency (black) and selection efficiency to fully contained (green) and partially contained (red) events as a function of E_ν. The up/down discrimination and charge identification in neutrino events are also shown. *Right:* Neutrino zenith angle, energy and L/E resolution as a function of the energy.

FC events		PC events		Total
Event in the fiducial volume		Vertex in the fiducial volume		
.AND. $E_\mu > 1.5$ GeV	1317	*.AND.* muon range > 4 m	384	1701
Number of layers ≥ 7	1023	Number of layers ≥ 7	331	1354
$y \tan^2 \theta_\nu < 0.75 E_\nu$	931	$\Delta p/p \leq 30\%$	259	1190

Table 4.1: Expected number of downgoing ("un-oscillated") ν_μ-CC events in four years of MONOLITH exposure to atmospheric neutrinos. Event selections are discussed in the text.

sense of direction of the neutrino. As discussed in section 4.2.3, by taking advantage of the timing capabilities of the sensitive detectors, the flight direction is determined in each event from a least-square fit of the timing in each layer versus the layer number. The up/down discrimination capability mostly rely on the muon hits and improves in events with long muon tracks. No attempt to filter hits not belonging to the muon track has been made, nor has the identification of the event vertex from the hadronic activity been tried yet. The up/down discrimination of this method is in excess of 95% at all neutrino energies, the residual confusion being due to events of low energy and near the horizon in which the muon track has a vertical extension comparable to the one of the hadronic shower. These latter events are easily resolved by hand scanning. Advances in pattern recognition will probably achieve this by automatic means. If not, the event sample is relatively small and it can be done by hand scanning. In the discussion of the MONOLITH sensitivity (see next chapter) a perfect up/down discrimination is assumed.

4.4 Backgrounds

Cosmic muons represent the main background source to the sample of atmospheric muon neutrino events of high energy. The flux of cosmic muons in underground sites as a function of the rock depth has been studied for several years. Direct measurements at the LNGS have also been performed by MARCO and LVD collaborations [87, 88]. A rate of about 4 (2.6) $\times 10^6$ y^{-1} muons above an energy threshold of 1 GeV is expected to impinge on the top (sides) of the MONOLITH detector. Only a fraction of these events, corresponding to stopping muons or to muons entering from dead zones, is however a potential source of background. These background sources have been studied in a dedicated simulation, in which we have adopted a Monte Carlo generator, developed inside the LVD collaboration [89], to describe the differential flux as a function of zenith, azimuth and energy at the LNGS underground location. A sample of several 10^8 muons has been processed with the MONOLITH simulation and reconstruction programme.

In order to save CPU time, events have been pre-scaled and weighted at the generation level and the full track-fit in the magnetic field has not been performed. The direction of the track at the vertex has been estimated from a straight line fit to track points over the first two meters of range. As a consequence, selections on the quality of the track fit have not been applied on the simulated cosmic muon samples. Events have been retained as fake ν_μ-CC if they hit at least 7 layers and if they passed the fiducial selections discussed in the previous section, i.e. if they were either fully contained in the fiducial volume or had a single outgoing track more than 4 m long. The time-of-flight analysis of has been performed on all muons surviving these selections.

Misidentified down-going muons can be classified into three main categories:

1. μ-stop to which a wrong flight direction is assigned, which are then misidentified as partially contained up-going muon neutrino events;

2. μ-stop entering from a dead zone, which are misidentified as down-going fully contained ν_μ interactions[3];

3. through-going muons entering from a dead zone; which fake partially contained down-going ν_μ events.

The identification of events belonging to the first class is mainly based on the identification of the time-of-flight direction; events in the other two categories are reduced by fiducial cuts complemented by an external veto.

The flight direction is determined in each event from a least-square fit of the timing in each layer versus the layer number. As discussed in section 4.2.3, an automatic procedure has been developed, which is used to identify "out-of-time" hits (not to enter the fit), occurring in the tails of the resolution function (see figure 4.2), and to fit $1/\beta$ of the track on the good ones. The present procedure leaves a background of 11 events/year, after requiring that at least 7 layers are hit and that the measured range of the track is at least 4 m. This remaining background is to be ascribed to tracks entering the detector near the horizon and being either bent upward by the magnetic field so to appear as truly up-going muons (about half of them), or misidentified by a residual inefficiency of the algorithm on short tracks with a small number of hits.

For comparison, the above-mentioned selections retain about 82 y^{-1} upgoing ν_μ-CC events in absence of oscillations, which are reduced to 65 y^{-1} after the additional requirement that the estimated resolution on the momentum fit be better than 30% (see discussion in the previous section and table 4.3.2). The analysis of the track curvature in the magnetic field and the requirement that a good track fit is obtained (not yet performed on muon samples) should provide an additional handle to reduce the cosmic muon background, since stopping tracks show an increased curvature at their end. The remaining background events are indeed easily recognised by hand scanning. Since the total number of events expected in a year is small, hand scanning is affordable. Alternatively we have considered a tighter selection by combining the number of fired layers and the visible muon range: we require at least 10 layers, if the range is below 5.5 m; 9 layers, if it is between 5.5 m and 7.5 m, 8 layers between 7.5 m and 9.5 m and 7 layers otherwise. This selection obviously reduces short tracks near the horizon and leaves 3.1 events/year of background, while reducing the efficiency to PC neutrino events by about 5%.

With the fiducial cuts described several thousand events entering through dead zones, from top and from sides, contribute to classes 2 and 3, if no additional high-efficiency veto is adopted. These events, however, can also be sizeably reduced by additional fiducial selections based on event topology, which marginally affect the overall MONOLITH efficiency to ν_μ-CC events. A summary of the topological selections we have considered is given in table 4.2 and discussed hereafter. The basic idea relies on the identification of the track vertex and on muon back-tracking. Indeed, muons belonging to Classes 2 and 3 should appear around dead zones and back-point to them.

Figure 4.8 shows a top view of MONOLITH with the distribution of the reconstructed vertex of cosmic muon tracks of both Classes.

About 6000 events/year entering from the top of MONOLITH are expected, 97% of which are clustered around the seven 6 cm wide iron supports of layers and the remaining 3% is spread over the MONOLITH surface and enters through 5 mm dead gaps between Glass Spark Chambers, which have not been staggered along the Y direction in the simulation[4]. This latter events (about 150 y^{-1}) can be rejected by shifting the dead zones in two of the four uppermost layers also along Y. The events entering trhough iron supports are efficiently rejected requiring

[3]Events of this class to which a wrong flight direction is assigned may fake up-going fully contained ν_μ events, but are negligible.

[4]Staggering along X on the first four layers has been considered instead (see section 4.1 for a discussion of the simulated layout).

	Class 2: μ-stop (FC-like)	Class 3: μ-through (PC-like)
impinging on top	704.0	5356.5
after s-cut	5.6	39.4
impinging on sides	20719.4	33361.9
after s-cut	19887.6	29342.0
after s and p-cut	12.9	88.4
total surviving	18.5	127.8

Table 4.2: Rate of cosmic background events/year entering from dead zones of MONOLITH and faking ν_μ-CC events with a vertex inside the fiducial volume (see text). The background reduction achievable by means of topological selections is shown. Each selection is discussed in the text. The overall reduction in ν_μ-CC efficiency due to these selections is less than 10%.

the vertex not in the strips adjacent to them. This would give a 5% reduction in effective mass for ν_μ CC events, if not correlated to the track direction. If a combined cut on the angle at the entry point in MONOLITH and on the vertex position is applied ("s-cut" in table 4.2), the events entering from the top are reduced to around 50 y^{-1} without substantially affecting the fiducial mass. The remaining events are still mainly located around the iron supports and can be reduced by an external veto counter.

Events entering from sides are also somewhat reduced requiring the vertex not adjacent to iron supports (see table). The bulk of this background however is due to muons at relatively small angles which enters through the 8 cm thick iron layers and travel undetected several tens of centimeters (see the bottom panel of figure 4.8). This background is asymmetric and on the Teramo side is about 30 times higher than on the Assergi side, due to the lower rock overburden.

A clear signature of these events is given by the correlation between the distance from the muon vertex to its entry point in MONOLITH and its direction, which can be exploited to reduce this background as shown in Fig. 4.9–*Left*. The distributions of muon events and ν_μ-CC are compared: at small angles near the horizon, where background events are clustered, only a few ν_μ-CC events survive the selection criteria discussed in the previous section. An additional fiducial selection, defined by the continuous line in the figure ("p-cut" in the table), would reduce the background by two orders of magnitudes, while retaining more than 95% of ν_μ-CC events.

Muons surviving the selections discussed have an hard momentum spectrum (practically flat up to beyond 100 GeV) and no hadronic activity at the muon vertex, at clear variance with ν_μ-CC events selected (see figure 4.9–*Right*). This and the fact that hard muons will have their momentum determined with large uncertainty could provide further discrimination capability between incoming muons and neutrino interactions.

What remains should be removed by an external veto. This veto could be designed to be highly efficient around the detector dead zones. A continuous veto, like the one considered in the previous Chapter, however, would reduce the intrinsic uncertainties of the procedure described and enables to save around 10% of fiducial volume.

In summary, we have shown that the muon background can be reduced to a negligible level by exploiting the timing resolution of the Glass Spark Chambers and by additional fiducial selections which will only marginally affect the overall efficiency to neutrino events. This procedure can be complemented by an external veto. The optimal balance between selection criteria and veto efficiency is still under study.

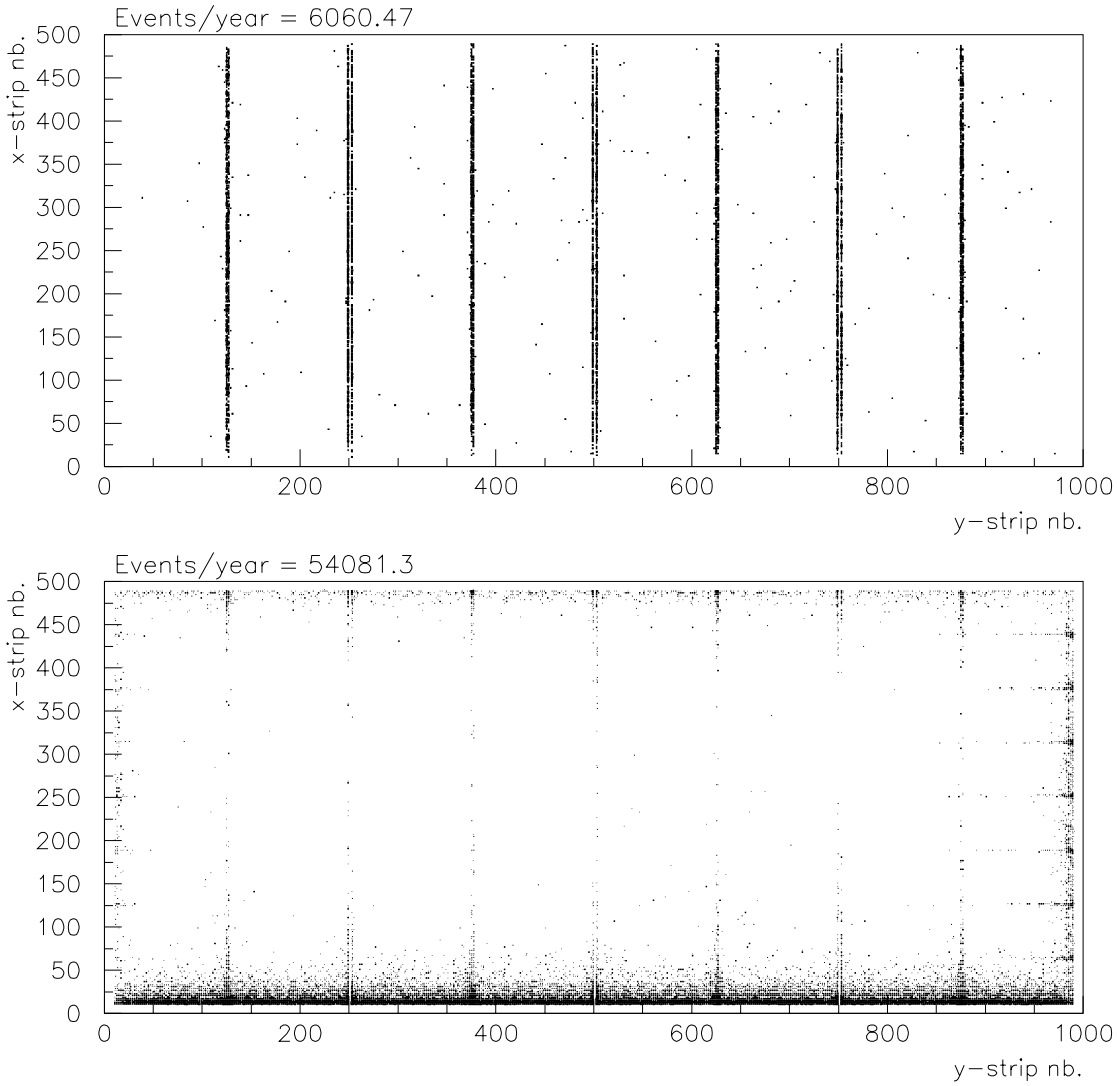

Figure 4.8: Top view of MONOLITH displaying the vertex coordinates of cosmic muon events of class 2 and 3 (see text). Events entering from the top (sides) of the detector are shown in the top (bottom) panel. Only the fiducial cut at the edges of the detector is applied

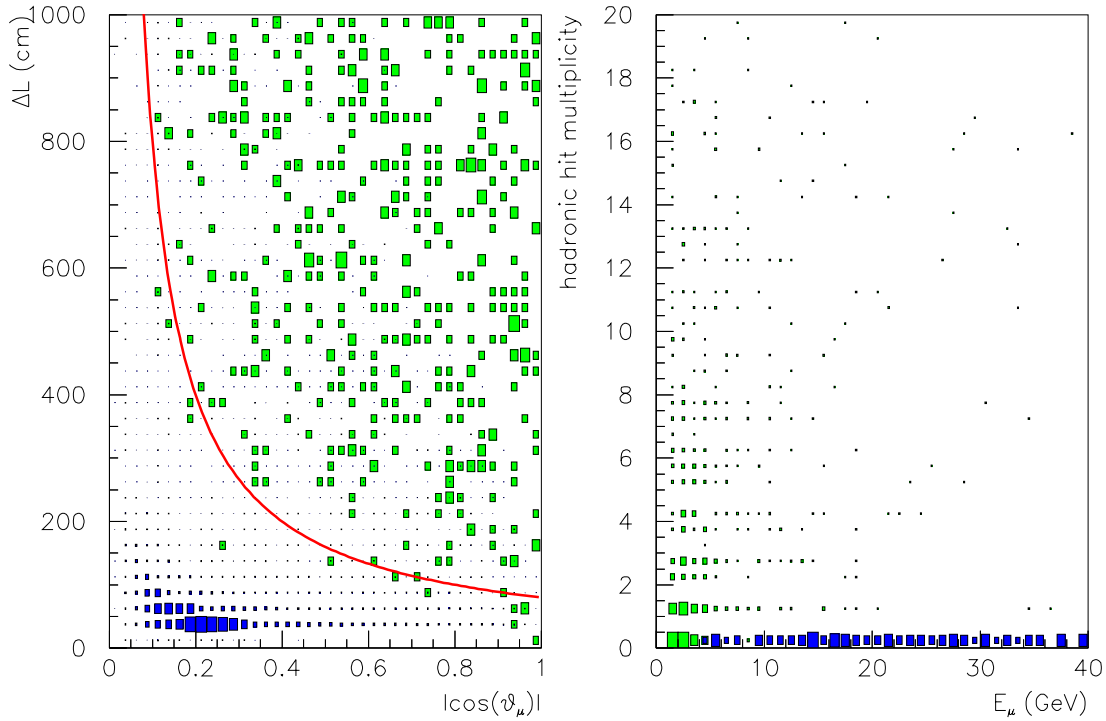

Figure 4.9: *Left:* The distance between the muon vertex and its entry point in MONOLITH as derived from muon back-tracking is plotted versus $\cos\theta_\mu$ obtained from the track fit. The distribution of muon events (clustered in left-bottom corner) and ν_μ-CC are contrasted. The continuous line in the figure defines the "p-cut" of table 4.2. *Right:* Distribution of the muon energy and hit multiplicity at the track vertex for the residual cosmic background and for neutrino events.

Chapter 5

Physics with atmospheric neutrinos

5.1 Introduction

In this Chapter, the sensitivity of MONOLITH to oscillations using atmospheric neutrinos is discussed. We shall give results on the MONOLITH capability to detect an oscillation pattern, discriminate alternative hypotheses to oscillations and measure oscillation parameters (section 5.2). The MONOLITH potential to discriminate between ν_μ oscillations into a sterile or a τ neutrino, by means both of a ν_τ appearance search (section 5.3.1) and of a study of Earth induced matter effects (section 5.3.2), is also presented.

5.2 Disappearance of muon neutrinos

5.2.1 Far/Near sources comparison

Atmospheric neutrino fluxes are not in general up/down symmetric. However, the up/down asymmetry, which is mainly due to geomagnetic effects, is reduced to the percent level for neutrino energies above 1.5 GeV [83, 84] [1]. At these energies, for $\Delta m^2 < 10^{-2}$ eV^2, as indicated by Super-Kamiokande results, downward muon neutrinos are almost unaffected by oscillations. Thus, they may constitute a *near* reference source. Upward neutrinos are instead affected by oscillations, since the L/E ratio of their path length over the energy ranges up to 10^4 km/GeV. Atmospheric neutrinos therefore represent an ideal case for a disappearance experiment, since one may study oscillations with a single detector and two sources: a *near* and a *far* one. The effects of oscillations are then searched comparing the L/E distribution for the upward neutrinos, which should be modulated by oscillations, with a reference distribution obtained from the downward neutrinos. For upward neutrinos the path length L is determined by their zenith angle as $L(\theta)$, while the reference distribution is obtained replacing the actual path length of downward neutrinos with the mirror-distance $L'(\theta) = L(\pi - \theta)$ (see Fig. 5.2.1).

According to the figure and given symmetry properties of the cosine, the neutrino path-length can therefore be estimated as $L(\theta) = R_{Earth}(\sqrt{1 - k^2 \sin^2\theta} - k|\cos\theta|)$, where $k = R_{Earth}/(R_{Earth} + \Delta R) \simeq 0.995$ and ΔR represents an average neutrino production height in the atmosphere. The ratio $N_{up}(L/E)/N_{down}(L'/E)$ will then correspond to the survival probability given, in case of oscillations, by eq. (2.1) (section 2.2.2). A smearing of the modulation is introduced by the finite L/E resolution of the detection method as discussed in the following.

Some remarks are in order:

i) results obtained by this method (known as Picchi & Pietropaolo's [18]) are to a large extent insensitive to systematic effects arising from uncertainties in the knowledge of atmospheric

[1] As discussed in section 4.3.2, MONOLITH has an effective threshold around 3 GeV on ν_μ-CC events.

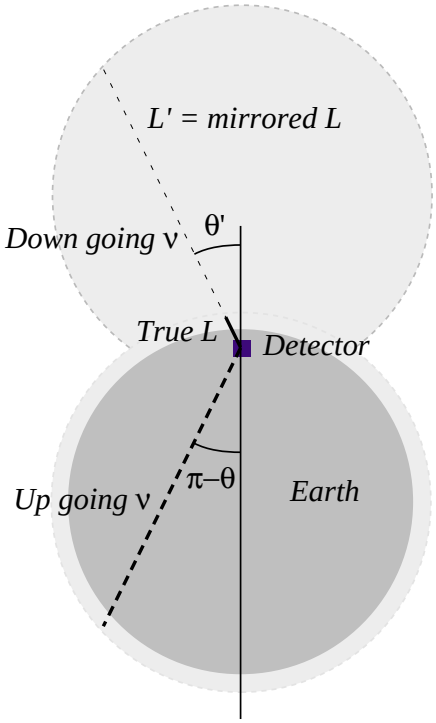

Figure 5.1: Artist's view of the mirror neutrino path length: downward going neutrinos (zenith angle $\theta < \pi/2$) are assigned the distance they would have travelled if $\theta = \pi - \theta$.

fluxes, neutrino cross sections and detector inefficiencies.

ii) this method does not work with neutrinos at angles near to the horizontal ($|\cos\theta| < 0.07$), since the path lengths corresponding to a direction and its mirror-direction are of the same order.

We also notice that if Δm^2 were larger than 10^{-2} eV^2 (Kamiokande region), upward neutrinos would be in almost complete oscillation, while the oscillation pattern would become detectable in the downward sample. In this limit, a mirror-distance $L'(\theta) = L(\pi - \theta)$ can be assigned to upward neutrinos, which can be used as a reference L/E distribution for downward neutrinos. In this case, due to the uncertain estimate of the neutrino path-length for downgoing neutrinos related to our ignorance of their production height in the atmosphere, there would be some model dependence in the determination of the oscillation parameters. Nonetheless, the observation of an oscillation pattern would still firmly test the oscillation hypothesis.

Data have been generated for several different values of oscillation parameters and processed through the MONOLITH full simulation and reconstruction programme. A unique set of selection criteria, outlined in Section 4.3.2, has been applied to all the samples of simulated data, independently of the values of oscillation parameters. These criteria have been defined to enable the selection of a pure sample of ν_μ-CC events of high resolution. In total, about 10^3 ν_μ-CC events will be selected in four years (for a 34 kt detector), with an L/E resolution of 50% FWHM over the entire L/E range.

The analysis of the resulting L/E spectra has been based on a binned maximum-likelihood procedure. Similarly to the definition of event selections, the bin boundaries of the L/E distri-

butions have been fixed without prior knowledge of the oscillation parameters. An equal bin-size on a logarithmic scale, corresponding to a constant relative L/E sampling resolution, has been adopted. It can be shown that, in order to keep sensitivity to the oscillation pattern for every possible (yet unknown) value of Δm^2, the bin-size should satisfy $\Delta \log(L/E) \leq 0.5$ [85]. As for the requirement of an L/E resolution better than 50% FWHM, the upper limit at 0.5 on the bin-size is set by the requirement that the oscillation be sampled at twice its frequency at least over the first modulation period.

The likelihood function compares the observed rates of upgoing to downgoing events as a function of L/E and is defined as:

$$\mathcal{L} = \prod_{i=1}^{N_{bins}} \frac{\mu_i^{D_i} e^{-\mu_i}}{D_i!} \left[\mu_i P_i(\Theta, \Delta m^2)\right]^{U_i} \frac{\exp\left[-\mu_i P_i(\Theta, \Delta m^2)\right]}{U_i!} \tag{5.1}$$

where the first term accounts for the Poisson probability that an expectation value of μ_i events would have produced the D_i downgoing events actually observed, while the second term gives the Poisson probability to observe U_i upgoing events when $\mu_i P_i(\Theta, \Delta m^2)$ are expected. $P_i(\Theta, \Delta m^2)$ represent the ν_μ survival probability for the *i-th* bin for given values of oscillation parameters and is parametrised as:

$$P(L/E; \Theta, \Delta m^2) = 1 - \frac{\sin^2(2\Theta)}{2}\left[1 - R(\Delta m^2, L/E)\cos(2.54\Delta m^2 L/E)\right], \tag{5.2}$$

where $R(\Delta m^2, L/E)$ folds in the experimental resolution and is taken as the Fourier transform of the resolution function. This parametrisation of the survival probability is valid under the assumption that the L/E resolution function be symmetric and that the L/E spectra of upgoing and downgoing neutrinos be (practically) flat [86]. Both these assumptions are reasonably satisfied. In particular, in the region where the first oscillation would manifest itself for any value of Δm^2 allowed by the Super-Kamiokande results, the L/E spectrum of selected events exhibits a variation of order 10% over a range where the resolution function changes by a factor 2. According to the MONOLITH simulation, and neglecting the small asymmetry in the L/E resolution function (see figure 4.5), $R(\Delta m^2, L/E)$ is best parameterised by an exponential damping term $R(\Delta m^2, L/E) = \exp(-0.25\Delta m^2 L/E)$, corresponding to a Cauchy resolution function of 50% FWHM. Studies of systematic effects related to the knowledge of the resolution function are in progress.

The evaluation of the MONOLITH sensitivity has been based on the following statistical analysis. High statistics data samples have been simulated (corresponding to 25 y of exposure) and normalised to four years. Then the likelihood function (5.1) has been maximised with respect to all the parameters: μ_i (i = 1,... N_{bins}), Δm^2 and $\sin^2(2\Theta)$. This approach very conservatively assumes no prior knowledge of the atmospheric neutrino fluxes, described by the μ_i parameters. Only the up/down symmetry of fluxes in case of no-anomalies in neutrino physics is implicitly embodied in the likelihood function.

After maximisation, the allowed confidence regions in the ($\sin^2(2\Theta)$,Δm^2) space have been evaluated by exploiting the properties of the likelihood-ratio function, defined by the quotient:

$$\lambda(\Delta m^2, \sin^2(2\Theta)) = \frac{\mathcal{L}_{max}(\hat{\mu}_i, \ldots\ \hat{\mu}_{N_{bins}}, \Delta m^2, \sin^2(2\Theta))}{\mathcal{L}_{max}(\hat{\mu}_i, \ldots\ \hat{\mu}_{N_{bins}}, \widehat{\Delta m^2}, \widehat{\sin^2(2\Theta)})}, \tag{5.3}$$

which represents the ratio of the maximum of the likelihood function within the subspace specified by fixed values of the oscillation parameters ($\sin^2(2\Theta)$, Δm^2) to the maximum of the likelihood function over the entire parameter space. The statistics $-2\log(\lambda)$ behaves asymptotically like a $\chi^2(2)$ distribution, whence the confidence regions have been determined. This

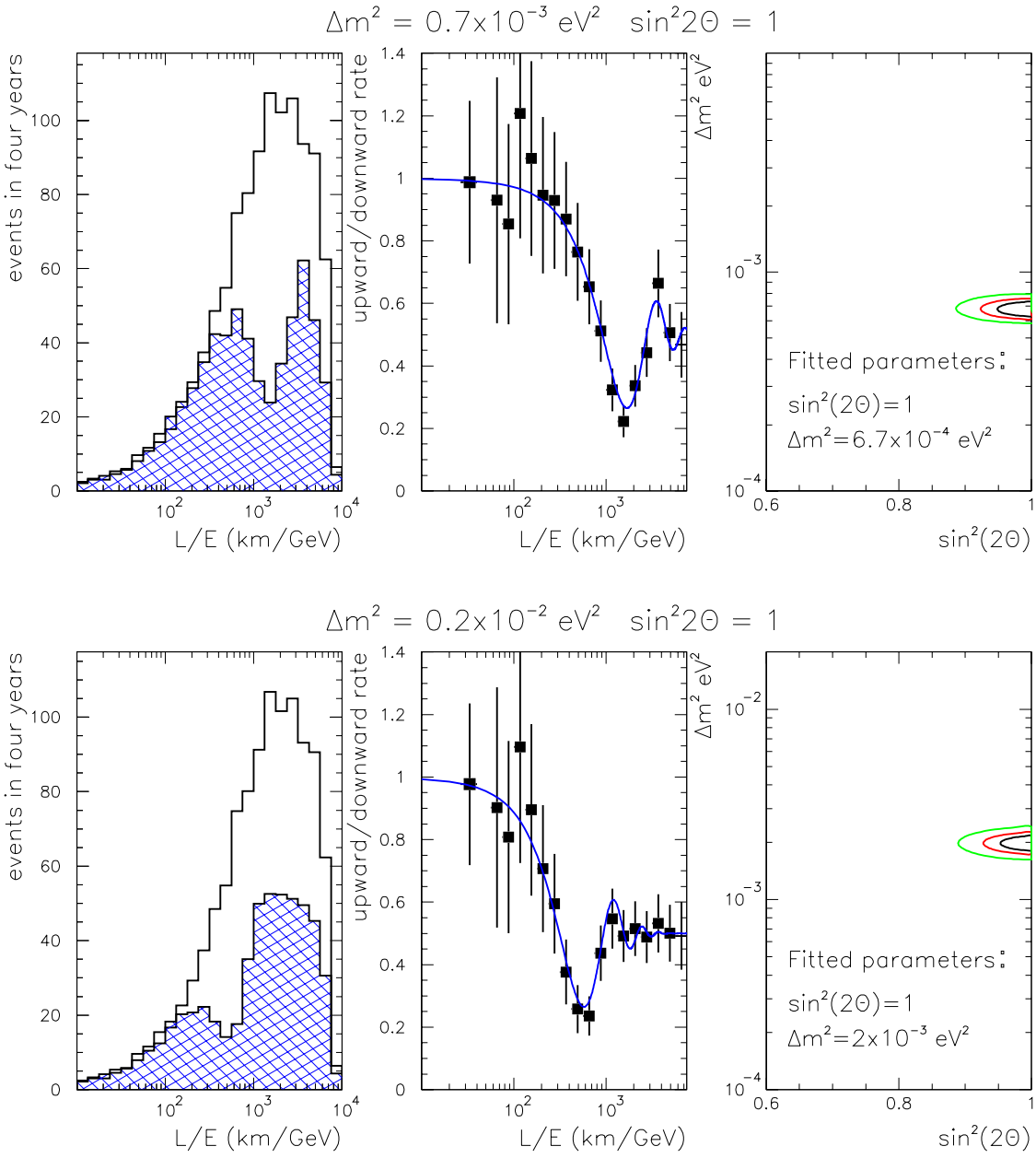

Figure 5.2: Results of the L/E analysis on a simulated sample in the presence of $\nu_\mu \to \nu_x$ oscillations, with parameters $\Delta m^2 = 7 \times 10^{-4}$ eV^2 and $\sin^2(2\Theta) = 1.0$ (top) and $\Delta m^2 = 2 \times 10^{-3}$ eV^2 and $\sin^2(2\Theta) = 1.0$. The figures show from left to right: the L/E spectrum of upward muon neutrino events (hatched area) and the L/E "mirrored" spectrum of downward muon neutrino events (open area); their ratio with the best-fit superimposed (the first point is integrated over the first six bins) and the result of the fit with the corresponding allowed regions for oscillation parameters at 68%, 90% and 99% C.L.. Simulated statistics correspond to 25 years of data taking, errors and rate normalisation entering in the best-fit procedure correspond to four years.

procedure gives results identical to the ones obtained by means of the MINOS processor of the MINUIT library [90], which performs the computation of contours of equal likelihood with respect to two (oscillation) parameters, taking into account of all the correlations with the other (N_{bins}) parameters[2].

It has been checked that the procedure adopted yields a good approximation of the exact sensitivity contours. For each value of Δm^2, 10^4 experiments of four years each have been simulated, by sampling high-statistics L/E distributions shown in the figures, and the likelihood function (5.1) has been maximised with respect to all the parameters: in 93% of the cases, the maximum-likelihood estimates of the oscillation parameters are found to fall inside the 90% C.L. contours displayed.

If some prior knowledge of the atmospheric neutrino fluxes is assumed, e.g. by letting the overall normalisation of the flux vary, while fixing the shape of the neutrino spectrum (this is equivalent to the approach adopted by Super-Kamiokande), the coverage of our estimated 90% C.L. regions increases to 97% of the simulated experiments.

The L/E distributions for upward- and downward-going neutrinos obtained with the outlined procedure are shown in Figs. 5.2 to 5.4 for Δm^2 ranging from 7×10^{-4} to 8×10^{-3} eV^2 and maximal mixing. The figures also show the discovery potential (allowed regions of the oscillation parameter space) of the experiment after four years of exposure as determined from the maximisation of the likelihood function.

For large values of Δm^2 this approach loses sensitivity to the determination of the oscillation frequency, because of the limited statistics at small L/E. At Δm^2 around 10^{-2} eV^2 oscillation starts to manifest in the downgoing sample and the Picchi & Pietropaolo's method adopted here is not optimal. Still an up/down asymmetry will be clearly visible. Moreover, for Δm^2 larger than a few 10^{-2} eV^2, upward neutrinos – at large L/E – will be in complete oscillation, while the oscillation pattern would become detectable in the downward sample. In this limit, a mirror distance $L'(\theta) = L(\pi - \theta)$ can be assigned to upward neutrinos, which can be used as a reference L/E distribution for downward neutrinos. In this case, due to the uncertain estimate of the neutrino path-length for downgoing neutrinos related to our ignorance of their production height in the atmosphere, there would be some model dependence in the determination of oscillation parameters. Nonetheless, the observation of an oscillation pattern would still firmly test the oscillation hypothesis. An example of the L/E distribution and results obtained with this analysis was given in the MONOLITH Progress Report [1].

The results of the outlined analysis are summarised in figure 5.5. The precision on oscillation parameters (allowed regions at 90% C.L.) that can be achieved in four years of exposure is compared to the regions at 90% C.L. allowed by the Kamiokande and Super-Kamiokande results. In the absence of oscillations, the arguments presented can be used to exclude a region of oscillation parameters. The exclusion limits that this experiment will be able to set after an exposure of one year at 99% C.L. or four years at 90% and 99% C.L. are also shown in the figure.

Assuming that the oscillation hypothesis is true and for maximum mixing, MONOLITH can improve by one order of magnitude the relative accuracy in the measurement of Δm^2 over the

[2]The sensitivity curves obtained in this way are very similar to the ones derived in the MONOLITH Progress Report [1] after maximisation of the "integrated" likelihood function:

$$\mathcal{L}_I(\Delta m^2, \sin^2(2\Theta)) = \int_0^\infty \mathcal{L}(\mu_1, \ldots \mu_{N_{bins}}, \Delta m^2, \sin^2(2\Theta)) d\mu_1, \ldots d\mu_{N_{bins}} \tag{5.4}$$

where the unknown parameters μ_i ($i = 1, \ldots, N_{bins}$) describing the neutrino flux are projected out by integration. Although this "integrated" likelihood is not formally correct, since its associated joint probability does not converge, it can be renormalised without loss of generality by truncating the integration at some large value of the flux.

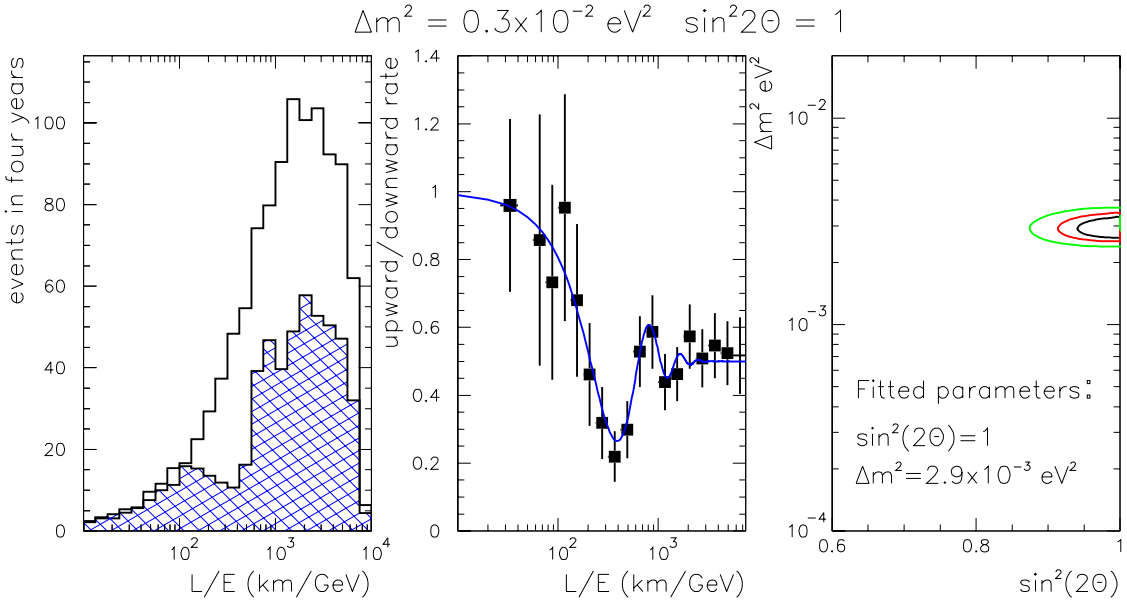

Figure 5.3: As Fig. 5.2, for $\Delta m^2 = 3 \times 10^{-3}$ eV^2 and $\sin^2(2\Theta) = 1$.

entire range of oscillation parameters indicated by the most recent Super-Kamiokande reports. From the measurement of the oscillation pattern alone, we estimate a one standard deviation accuracy at the 5-10% level with a weak dependence on Δm^2 (see also figure 5.7 and the corresponding discussion below).

5.2.2 Clearness of the oscillation pattern

The atmospheric neutrino anomaly reported by Super-Kamiokande is believed to demonstrate the existence of neutrino oscillations. Alternative explanations, in which ν_μ neutrinos disappear without giving raise to an oscillatory pattern, are still viable and consistent with Super-Kamiokande results [10, 11, 12], though.

These unconventional interpretations of Super-Kamiokande data share the feature of the absence of a first clear dip in the L/E distribution, at clear variance with the oscillation scenario. The MONOLITH experiment is designed to have sufficient resolution to detect an oscillation pattern and discriminate between these different models.

In order to make a quantitative statement, a test statistics needs to be defined. Neither the neutrino oscillation (null hypothesis) nor the unconventional models (alternative hypothesis) are simple hypotheses, since the model parameters are not (completely) fixed a priory and must be determined from the experimental observations. Therefore a Neyman-Pearson test is not applicable.

On the other hand, a likelihood-ratio test can be designed, by describing the spectral distortion to the L/E spectrum of muon neutrinos by means of a general parametric form (*comprehensive* parametric hypotheses [91]):

$$p(x; \underline{\alpha}, \underline{\beta}, \theta) = \left[(1-\theta)\ p_{H0}(x; \underline{\beta}) + \theta\ p_{H1}(x; \underline{\alpha}) \right], \tag{5.5}$$

where $x = L/E$, the parameter θ is bound between 0 and 1, $p_{H0}(x; \underline{\beta})$ and $p_{H1}(x; \underline{\alpha})$ are the probability density functions for the null hypothesis (H0) and the alternative hypothesis (H1).

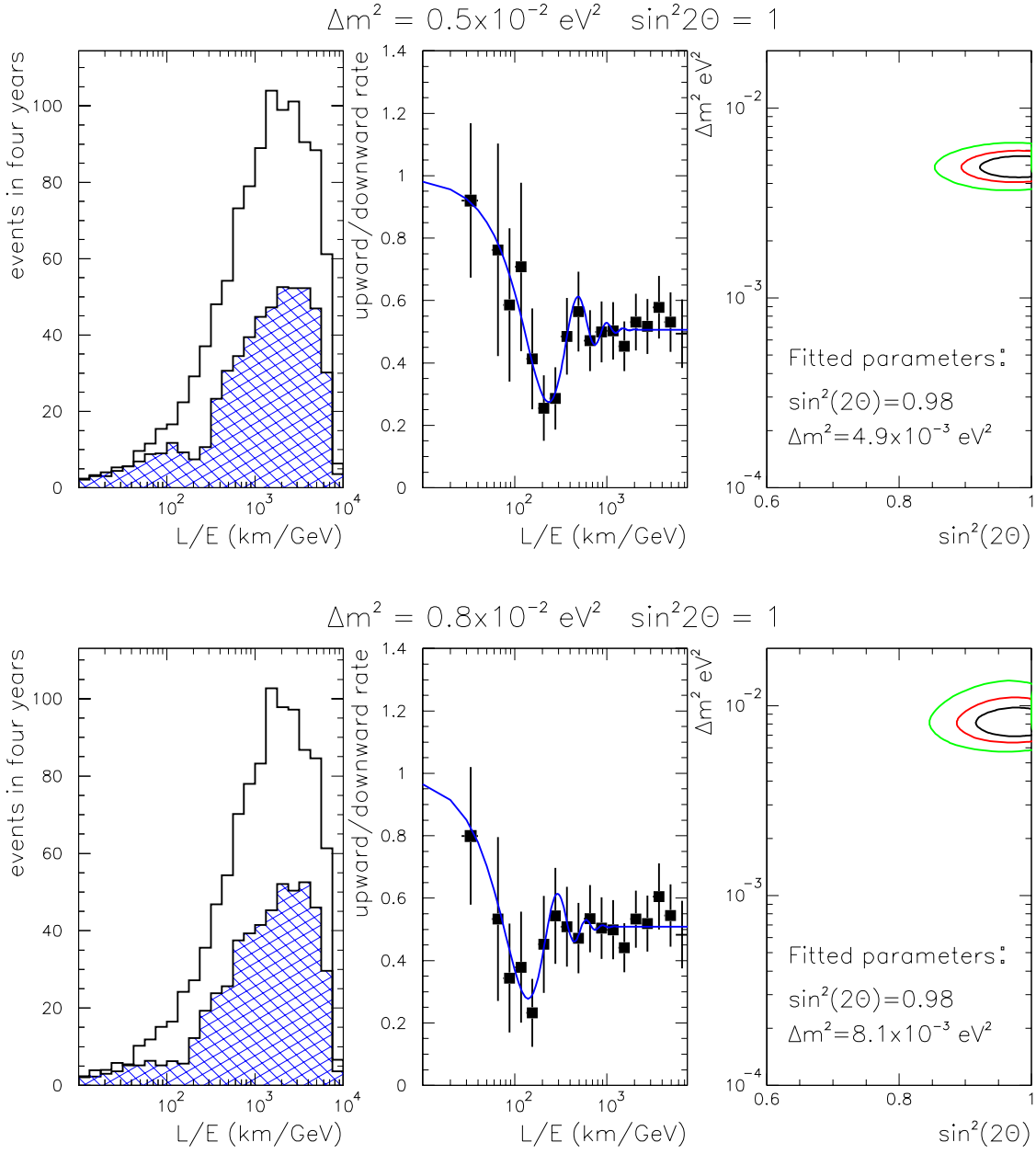

Figure 5.4: As Fig. 5.2, for $\Delta m^2 = 5 \times 10^{-3}$ eV^2 and $\sin^2(2\Theta) = 1$ (top) and $\Delta m^2 = 8 \times 10^{-3}$ eV^2 and $\sin^2(2\Theta) = 1$ (bottom).

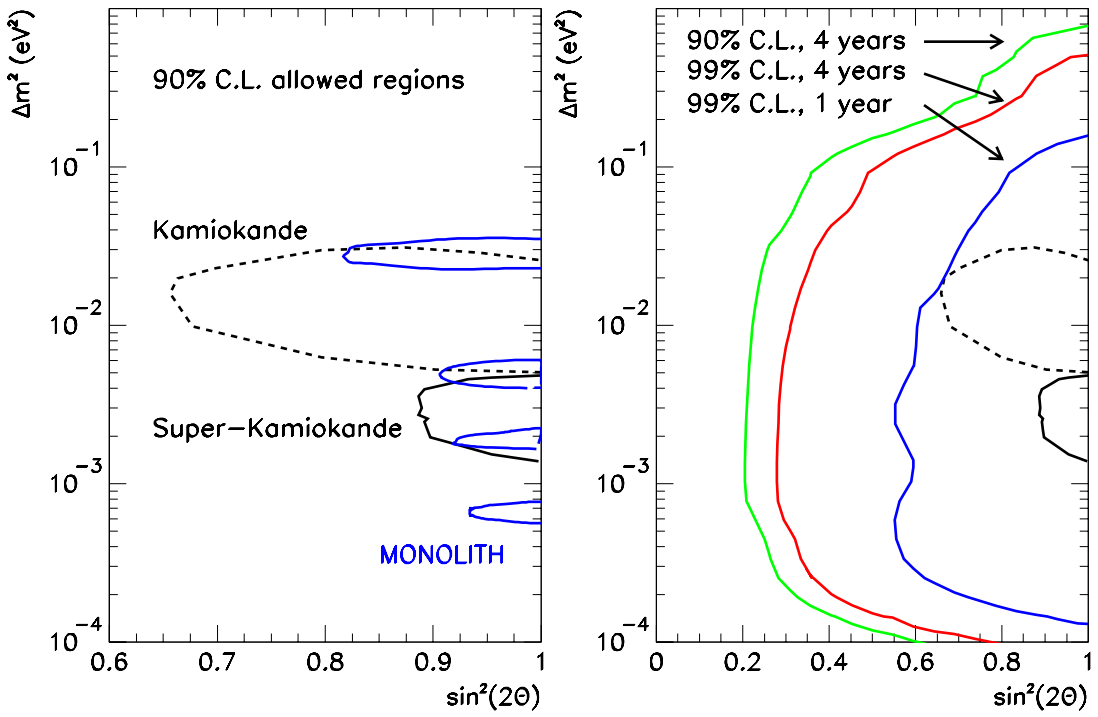

Figure 5.5: *Left*: Expected allowed regions of $\nu_\mu - \nu_\tau$ oscillation parameters for MONOLITH after four years of exposure, as obtained by the analysis described in the text: the results of the simulation for $\Delta m^2 = 0.7, 2, 5, 30 \times 10^{-3}$ eV^2 and maximal mixing are shown. *Right*: MONOLITH exclusion curves at 90% and 99% C.L. after one or 4 years of data taking assuming no oscillations. The full (dashed) black line shows the most recent results of the Super-Kamiokande [27] (Kamiokande [28]) experiment.

If either of the hypotheses is true, the parameters of equation (5.5) are restricted to lie in a subspace, defined by the constraints $\theta = 0$ (H0) or $\theta = 1$ (H1), of the total parameter space.

Given the observations x_1, x_2 ... x_n, a test statistics for either hypothesis can be defined by the quotient:

$$\lambda = \frac{\mathcal{L}_{max}(x_1, ... \; x_n; \underline{\alpha}, \underline{\beta}, \theta = 0, 1)}{\mathcal{L}_{max}(x_1, ... \; x_n; \underline{\alpha}, \underline{\beta}, \theta)}; \tag{5.6}$$

representing the ratio of the maximum of the likelihood function within the subspace specified by the restriction from either hypothesis to the maximum of the likelihood function over the entire parameter space. By construction, this ratio must be between 0 and 1, since the maximum of $\mathcal{L}$ over the subspace of either hypotheses cannot exceed the maximum over the entire space.

The ratio λ is a function of the observables and is intuitively a reasonable test statistics. If the maximum likelihood over the subspace of either hypothesis is close to the maximum likelihood over the full space ($\lambda \sim 1$), the hypothesis will have a large probability of being true. A small value of λ will indicate that the hypothesis is unlikely. The power of the test can be evaluated from the fact that in the asymptotic limit the statistics $-2\log(\lambda)$ approaches a $\chi^2(1)$ distribution.

The rejection power of the MONOLITH experiment against the alternative explanations to neutrino oscillations has been estimated by Monte Carlo techniques. In this study, the decay model of ref. [10] has been considered as alternative hypothesis to oscillation, since it allows for an easy parameterisation of the disappearance probability.

The best-fit of the decoherence model to Super-Kamiokande data [12] gives a parametric curve indistinguishable, for all practical purposes, from the one of the decay model, though analytically different. On the other hand, in the model proposed in [11], neutrinos transmogrify in a way which is not easy to parameterise analytically. The best-fits of this model to Super-Kamiokande data, however, again predict a disappearance probability rather similar in shape to the decay model and the results discussed hereafter should be still valid, to first approximation, also in that scenario. A detailed study is in progress.

In the decay model compatible with Super-Kamiokande data the survival probability is described by the parametric form:

$$p_{dec}(x, \underline{\alpha}) = \left(1 - \alpha_0 + \alpha_0 e^{-x/2\alpha_1}\right)^2 \tag{5.7}$$

where $x = L/E$ is the neutrino reduced path-length, α_0 is a mixing parameter and α_1 is the reduced decay length of the neutrino. This parametric form is only slightly affected by the experimental resolution, as the decay model does not have sharp structures.

On the contrary, the experimental resolution needs to be accounted for in case of neutrino oscillations. Following the discussion given in the previous section, equation (5.2) has been used to parameterise the survival probability for ν_μ–ν_τ oscillations (p_{osc}).

According to this discussion, a general parametric form for the survival probability of muon neutrinos is therefore given by equation (5.5), taking $p_{H0} = p_{osc}$ and $p_{H1} = p_{dec}$.

In the simulation of the experiments, the oscillation scenario with maximum ν_μ–ν_τ mixing has been assumed (null hypothesis). To test the rejection power against the alternative hypothesis at the 1% level, we have generated and analysed a large sample of experiments (10^4 for each value of Δm^2). To accomplish this, a simplified Monte Carlo simulation has been adopted: *i)* for each value of Δm^2 a high statistics (about 30 y of exposure) binned L/E spectrum has been obtained from the full simulation of the MONOLITH experiment after applying the selection criteria discussed in section 4.3.2; *ii)* from this set of reference L/E distributions, individual experiments of up to six years have been sampled according to Poisson statistics.

Δm^2 (10^{-3} eV^2)	statistics (kt·y) 95% prob. of rejection at 95% CL	statistics (kt·y) 95% prob. of rejection at 99% CL
1	34 x 1.6	34 x 2.7
3	34 x 2.4	34 x 3.3
5	34 x 3.0	34 x 4.1
8	34 x 4.1	34 x 5.6

Table 5.1: MONOLITH exposure needed to detect a "clear oscillation pattern" (see text).

Simulated data have been compared to the L/E distribution predicted for no-oscillation and tested using the log-likelihood function defined by:

$$\log \mathcal{L} = \sum_{i=1}^{N_{bins}} (n_i \log(A\mu_i) - A\mu_i - \log n_i!) - \frac{1}{2}\left(\frac{A-1}{\sigma_A}\right)^2. \tag{5.8}$$

The first term is the Poisson probability to observe n_i events when $A\mu_i$ are expected, where μ_i is given by the expected rate in the i-th bin in case of no oscillations times the survival probability over that bin, derived from eq. (5.5) and A is an overall normalisation factor. Similarly to the method adopted by the Super-Kamiokande collaboration, the second term in the likelihood is included to account for the prior knowledge on the atmospheric neutrino flux normalisation, which has been assumed to be known to 15%. No prior knowledge on model parameters has been assumed, instead.

For each simulated experiment, the likelihood function has been maximized over the entire space of parameters and over the subspaces defined by $\theta = 0$ (pure oscillation) and $\theta = 1$ (pure decay). As an example, four simulated MONOLITH experiments of 34×4 kt·y each, for $\Delta m^2 = 0.003$ eV^2 and maximum mixing, are shown in figure 5.6: the blue line is the best fit to data over the full parameter space, while the green (red) line is the best fit constrained to the subspace for H0 (H1).

The distribution of the test-statistics $-2\log(\lambda_{H0})$ obtained from the sample of simulated experiments has been used to define the critical regions at 95% C.L. and 99% C.L. of the null hypothesis. The distribution of $-2\log(\lambda_{H1})$ has been used to evaluate the probability that MONOLITH will reject the false hypothesis (decay) for a significance level on the true hypothesis of 95% and 99%. The test-statistics for the null hypothesis has been found to be consistent with the asymptotic $\chi^2(1)$ behaviour, hence the fraction of oscillation experiments giving $P(\chi^2 < -2\log(\lambda_{H1}), 1) \leq 0.05$ and $P(\chi^2 < -2\log(\lambda_{H1}), 1) \leq 0.01$ has been counted.

The results of the Monte Carlo calculation are shown in figure 5.7. MONOLITH has at least a 95% probability of rejection at 99% (95%) C.L. of the decay(-like) model up to $\Delta m^2 = 0.005(0.008)$ eV^2. The figure also show the precision on the determination of Δm^2 as obtained from the RMS dispersion of the likelihood fit on the simulated experiments assuming that the null hypothesis be true.

The "clearness of the oscillation pattern" can be (somewhat arbitrarily) defined as a 95% probability of rejection at 95% C.L. (or 99% C.L.) of the false (non-oscillation) hypothesis. The second and third columns of Table 5.1 summarise the statistics that MONOLITH needs to collect to demonstrate a "clear oscillation pattern" for the two definitions.

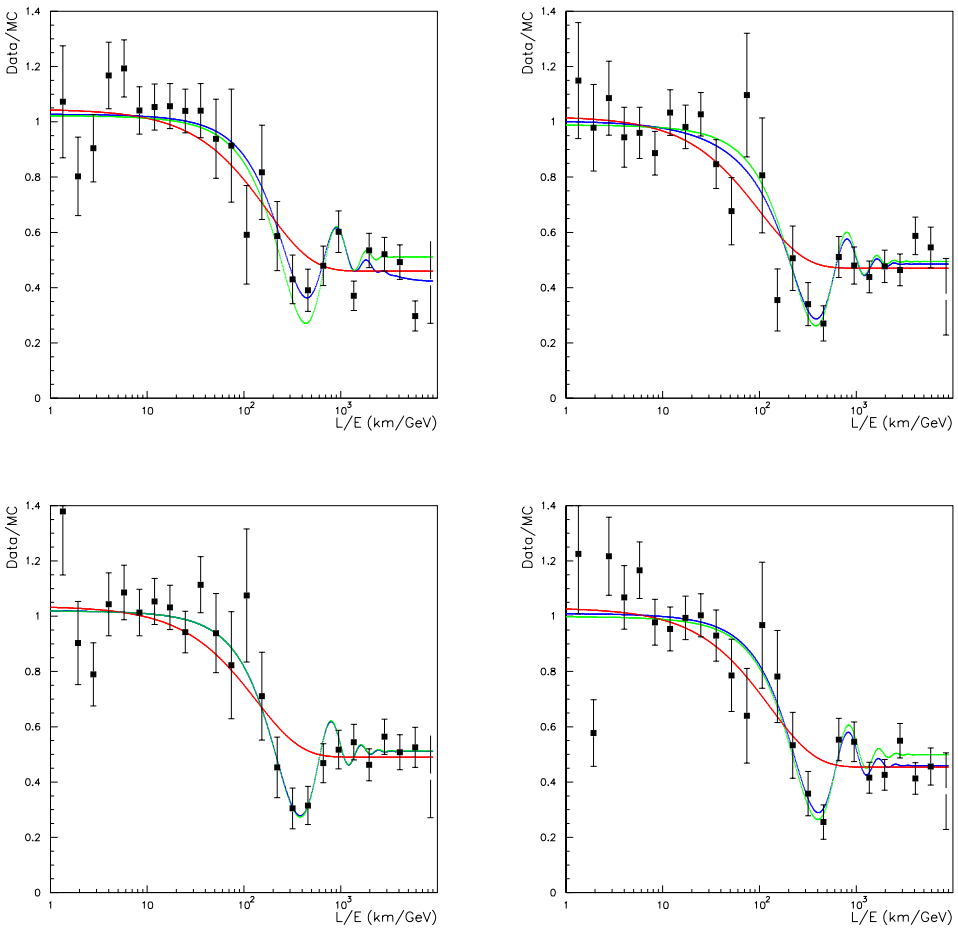

Figure 5.6: Four simulated MONOLITH experiments of 34×4 kt·y for $\Delta m^2 = 0.003$ eV^2. Experimental results are normalised to the neutrino spectrum for no oscillations. The survival probability of muon neutrinos derived from the best fit to data of the likelihood function over the full parameter space (blue), and over the subspaces for H0 (green) and H1 (red) are superimposed.

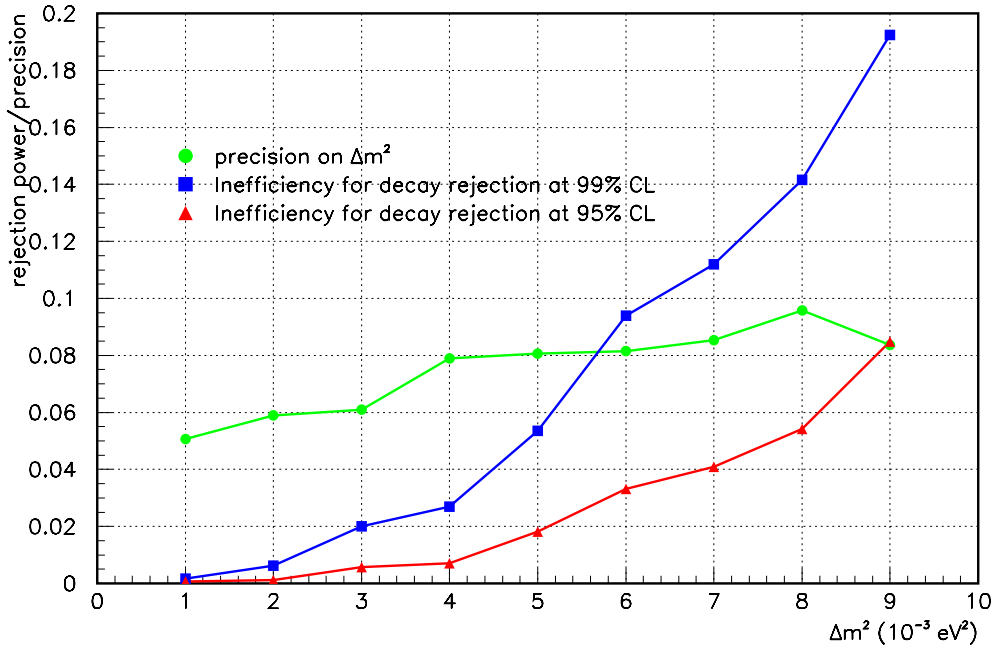

Figure 5.7: Inefficiency to decay model rejection as a function of Δm^2 for a significance level of 95% (red triangles) and 99% (blue squares) on the oscillation hypothesis. The precision on Δm^2 is also shown (see text).

5.3 Distinction of $\nu_\mu \to \nu_\tau$ and $\nu_\mu \to \nu_s$ oscillations

5.3.1 Appearance of tau neutrinos

If evidence of ν_μ disappearance is observed, for $\Delta m^2 > 3 \times 10^{-3}$ eV^2, the appearance of τ neutrino charged-current interactions can be searched for to distinguish between $\nu_\mu \to \nu_\tau$ and $\nu_\mu \to \nu_s$ oscillations. As discussed in Section 2.2.3, this method consists in measuring the upward/downward ratio of muon-less events, as a function of the visible energy. Charged-current ν_τ interactions would in fact result in an excess of muon-less events in the upward sample at high energies, due to the large τ branching ratio into muon-less channels ($BR \simeq 0.8$). Moreover, because of threshold effect on τ production, events of large visible energy must be selected, in order to enhance the relative ν_τ contribution to the muon-less event sample.

This is illustrated in Table 5.2, which shows the integrated rates of neutrino CC interactions expected for $\cos\theta < 0$ (upward neutrinos) and for $\cos\theta < -0.5$ (prior to event selections). The integrated ν_μ and ν_e NC event rates are about one third of the corresponding CC event rates. In case of oscillation into a ν_τ, the rate of NC events is conserved. On the other hand, if oscillations occur into a sterile neutrino, the rate of upgoing ν_μ-NC is approximately reduced by a factor of two.

	$E_{min}(GeV)$	ν_μ	ν_e	ν_τ		
				10^{-2} eV^2	3×10^{-3} eV^2	10^{-3} eV^2
$\cos\theta < 0$	3.	14.73	5.04	1.29	1.06	0.62
	10.	4.56	1.06	0.95	0.71	0.27
	30.	1.32	0.21	0.40	0.17	0.03
$\cos\theta < -0.5$	3.	6.38	1.61	0.54	0.53	0.43
	10.	1.78	0.25	0.40	0.39	0.21
	30.	0.51	0.04	0.18	0.13	0.02

Table 5.2: Neutrino + anti-neutrino integrated CC event rate (kt·y)$^{-1}$ for $\cos(\theta) < 0$ and $\cos(\theta) < -0.5$. For the ν_τ case, rates for maximal mixing and three different values of Δm^2 are given. Rates for ν_μ and ν_e correspond to the no oscillation hypothesis.

This method was first considered in [14], where the selection of muon-less candidates (defined as events without non-interacting tracks longer than 1 m, equivalent to a m.i.p. of 0.9 GeV) and the up/down discrimination were largely based on hand scanning. Since the statistics of these events is not large, hand scanning is affordable. Here, however, results of an automated analysis are reported.

The selection of muon-less events is based on the ratio of the visible energy to the event length and on the recognition of a penetrating track, defined as muon candidate of energy greater than 1.5 GeV (taken from simulation truth). The sample of muon-less candidates selected by these criteria has a slightly larger contamination of ν_μ-CC events than the muon-less sample of Ref. [14]. However, the comparison of visible energy and event length does not require pattern recognition, while hand scanning shows that muons of 1.5 GeV are easily visible and within the reach of further progress in pattern recognition algorithms.

In addition, in order to achieve good up/down discrimination, events with limited vertical development have been rejected by requiring that at least 5 layers be fired and that the visible energy in the event obtained from the hit multiplicity be larger than 4 GeV.

These selections have an efficiency on ν_τ interactions followed by muon-less τ decays of about 60%, while the purity of the upgoing muon-less sample, assuming perfect up/down discrimina-

tion, is about 25%. The ν_μ-CC and ν_e-CC background accounts for about 10% and 25% of the sample, while the remaining events are genuine NC interactions, which also carry useful information for the ν_τ/ν_s discrimination.

These values are integrated over the energy. However, the residual ν_μ-CC background has a soft energy spectrum, since the rejection of ν_μ-CC events with a hard muon ($E_\mu > 1.5$ GeV) is effective on high energy events (due to the flat y distribution of the CC interaction). The ν_e-CC background is mostly degraded to low visible energy, due to the coarse sampling of the detector which filters off the electro-magnetic component of the interaction. As a consequence the visible energy is mostly due to the residual hadronic component, as in the case of neutral current events.

The determination of the neutrino flight direction has been obtained by an automatic algorithm on the basis of the event topology and by taking advantage of the timing capabilities of the detector. The position of the centre of gravity of the event (as derived from the digital information) and of the earliest hits in the x and y views are determined along the z (vertical) direction, to establish whether they lay in the lowest or in the highest half of the event. The combined information of these variables is used to derive the flight direction of the neutrino. Moreover, these variables (event "vertex" and centre of gravity) provide a rough estimate of the neutrino zenith angle ($\simeq 20$ degrees FWHM), which has been used to filter events near the horizontal. These events are of little use in the measurement of the up/down asymmetry since near the horizontal the up/down confusion and the ν_e background are larger and (in the upgoing sample) the oscillation probability is smaller.

The up/down discrimination algorithm is not yet as effective as the result of hand scanning and optimisation is in progress.

After rejection of events with a reconstructed zenith angle within 15 degrees from the horizontal, for which the determination of the neutrino direction is most ambiguous, the efficiency to muon-less ν_τ interactions is reduced to around 40%. On average 85% of the ν_τ-CC events have their sense of direction correctly assigned.

Fig. 5.8 shows the result of the outlined analysis. The differential up/down asymmetry of muon-less events as a function of the visible energy, defined as

$$A(E) = \frac{U(E) - D(E)}{U(E) + D(E)}, \tag{5.9}$$

with clear meaning of symbols, is shown for maximal mixing and $\Delta m^2 = 5 \times 10^{-3}$ eV^2 and 10^{-2} eV^2 for the two alternative oscillation hypotheses (top). In the $\nu_\mu \to \nu_\tau$ case there is an excess of muon-less events with high visible energy from the bottom hemisphere due to the τ decay into muon-less channels that produce neutral current like events and, hence, a positive asymmetry; in the $\nu_\mu \to \nu_s$ case there is a lack of neutral currents from the bottom hemisphere at all visible energies, since the sterile neutrino does not interact. At low energies a negative asymmetry is observed also in the $\nu_\mu \to \nu_\tau$ case. This is due to the residual background of ν_μ-CC events at small energies which gets depleted in the upgoing sample because of oscillations.

The figure also shows (bottom) the probability density functions for the experimental outcome for the up/down asymmetry of muon-less events of visible energies above 7 GeV. Results are given for four years of data taking: the two alternative hypotheses are discriminated at 90% (95%) C.L. with a rejection power of about 1% (3%).

Figure 5.9 shows the significance (number of sigmas) of the ν_τ/ν_s separation in four years, defined as the difference between the expectation values of the asymmetry for the two hypotheses normalised to the expected error. Below 3×10^{-3} eV^2 this method loses sensitivity, since it relies on high energy neutrinos which do not oscillate enough. At larger Δm^2, the separation achieved by the present analysis is at the 2.5σ level, mainly limited by the current performance of the up/down discrimination algorithm. For an equivalent efficiency to muon-less ν_τ interactions,

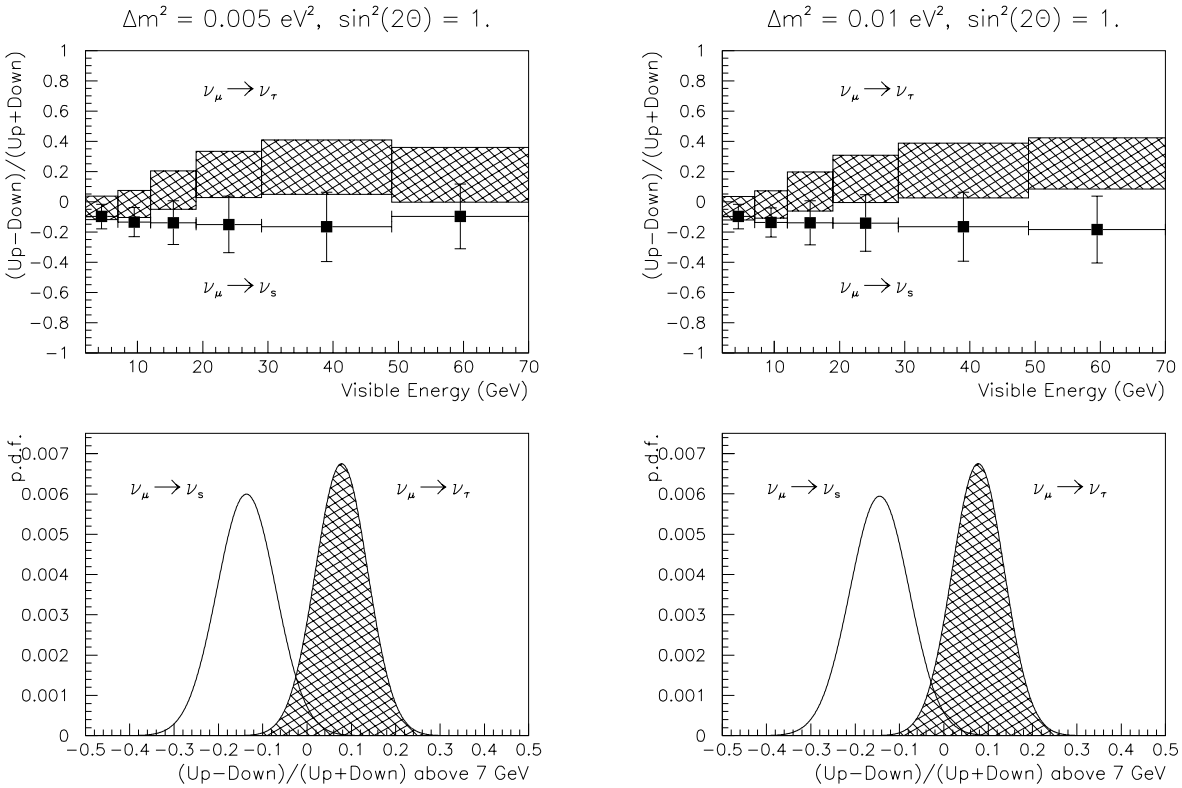

Figure 5.8: *Top:* Up/down asymmetry of muon-less events as a function of the visible energy, for maximal mixing and $\Delta m^2 = 5 \times 10^{-3}$ eV^2 (left) and $\Delta m^2 = 10^{-2}$ eV^2 (right). The expectations for $\nu_\mu \to \nu_\tau$ (hatched area) and for $\nu_\mu \to \nu_s$ oscillations (dots) are compared. Events have been generated with high statistics, error bars correspond to four years of data taking. The rightmost bin also integrates the contribution of events with reconstructed energy larger than 70 GeV. *Bottom:* Probability density function for the experimental outcome of the up/down asymmetry of events above 7 GeV after four years of data taking.

hand scanning reduces the probability of a wrong classification by more than a factor 2. As shown in the figure, if a perfect up/down discrimination is assumed, a separation of more than 3σ on the same sample of muon-less events is obtained.

5.3.2 Study of Earth-induced matter effects

To extend the discrimination capability of MONOLITH towards small values of Δm^2, another technique has been considered, based on potential matter effects affecting $\nu_\mu \to \nu_s$ oscillation inside the Earth. During the propagation through the Earth, neutrino interactions with matter can radically modify the neutrino oscillation pattern with respect to oscillations in vacuum. These effects occur for oscillations involving neutrinos having different effective potentials in matter [44]. Thus, no effect is foreseen for $\nu_\mu \to \nu_\tau$ oscillations; while in case of oscillations involving sterile neutrinos, the oscillation probability differs from the usual vacuum formula given in eq. (2.1).

In the latter case, a simple analytical expression for the oscillation probability can be derived if the propagation takes place in a uniform medium. Under this approximation, the vacuum

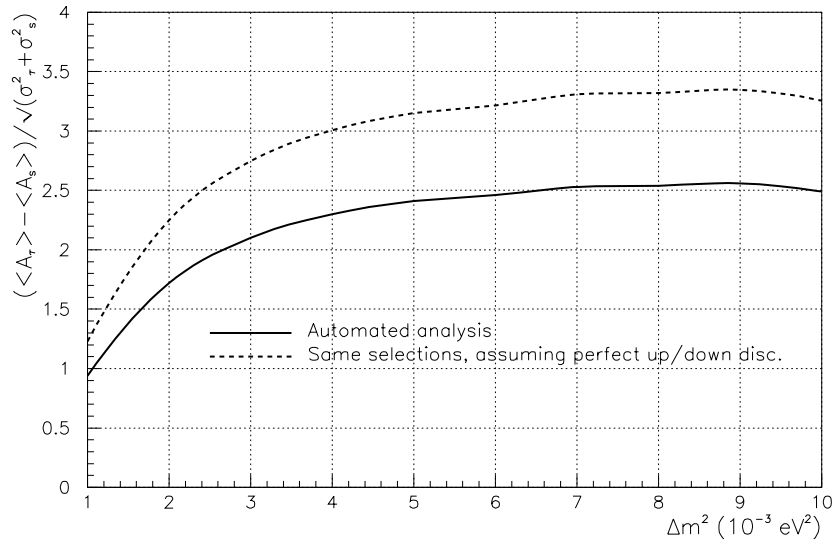

Figure 5.9: Significance of the ν_τ/ν_s separation in four years as a function of Δm^2.

oscillation probability (2.1) can be left invariant in form, by substituting the mixing angle and the oscillation length $l = 4\pi E_\nu/\Delta m^2$ with effective quantities:

$$\sin^2 2\Theta_m = \frac{\sin^2 2\Theta}{[\zeta - \cos 2\Theta]^2 + \sin^2 2\Theta} \tag{5.10}$$

$$l_m = \frac{l}{([\zeta - \cos 2\Theta]^2 + \sin^2 2\Theta)^{1/2}} \tag{5.11}$$

where $\zeta = 2E_\nu V_{\alpha\beta}/\Delta m^2$ and $V_{\alpha\beta} = V_{\mu s} = \mp\sqrt{s} G_F \frac{N_n}{2}$. In the effective potential $V_{\mu s}$, the minus (plus) sign holds for neutrinos (anti-neutrinos), G_F is the Fermi constant and N_n the neutron number density[3].

Equations (5.10) and (5.11), although strictly valid for the propagation in an uniform medium, are useful to summarise how matter effects would manifest themselves and which observables have to be considered to discriminate between $\nu_\mu \to \nu_\tau$ and $\nu_\mu \to \nu_s$ oscillations:

- Given the ζ dependence on $1/\Delta m^2$, matter effects are expected to be sizeable at small values Δm^2.
- In case matter effects are relevant, the oscillation pattern is not controlled by the L/E variable alone, but by L, E and the density of Earth crossed separately. Hence, a two-dimensional analysis in the (E, L) plane is necessary.
- Except from the special case $\sin^2 2\Theta = 1$, differences in the oscillation probabilities of neutrino and anti-neutrinos are expected. Hence, muons with different charges should be considered separately.
- The importance of Earth-induced matter effects increases with the energy, due to the ζ dependence on E_ν. Hence, up-going muons produced by ν_μ-CC interactions in the rock surrounding the apparatus, whose energy spectrum extends up to the TeV region, bring relevant information.

[3]Here $\hbar = c = 1$ is used.

A more realistic description of the propagation of neutrinos through the Earth requires that the density profile of the Earth be taken into account in the evolution equations. The Preliminary Earth Reference Model (PREM) for the Earth's density profile [92] has been used in the analysis discussed hereafter.

Earth-induced matter effects can be detected by reconstructing either ν_μ-CC interactions in the fiducial volume of MONOLITH ("internal events") or up-muons due to neutrino interactions in the surrounding rock entering the calorimeter from below or from the lateral walls ("external events").

"Internal events" have been selected according to the criteria discussed in section 4.3.2. An additional energy cut ($4 < E_\mu < 70$ GeV) has been applied in order to retain the high energy component of this sample. In case of no-oscillations, 474 upgoing "internal events" are expected in MONOLITH after an exposure of 34×4 kty. About 55% of such events are fully contained, in that the muon stops within the detector. The MONOLITH performance on fully contained and partially contained ν_μ-CC events has been discussed in section 4.3.2.

The simulation and selection of up-going muons produced by neutrino interactions outside the detector ("external events") is specific to this analysis, instead. Muons have been generated according to the energy and angular differential fluxes of ref. [45] and processed by the MONOLITH simulation and reconstruction programme. Events have been retained if the muon track was crossing at least seven layers and had a reconstructed cosine of the azimuthal angle smaller than -0.3 [4]. For "through-going" muons, it has also been required that the visible range be greater than 4 m, to keep the background of misidentified cosmic muons at a negligible level. After four years of exposure, 856 "external events" are expected in MONOLITH (377 stopping and 479 through-going muons).

The muon momentum at the impact point in MONOLITH has been reconstructed either from the visible range ("stopping external muons") or from the track curvature in the magnetic field ("through-going muons"), using the procedure discussed in section 4.2.1. From the analysis of the track curvature, the identification of the muon charge is also possible. The energy spectra of the two sub-samples together with the momentum resolution are plotted in fig.5.10. The mean momentum of the stopping muons is 7 GeV while the through-going distribution extends up to several hundred GeV ($\langle E \rangle \simeq 160$ GeV). Fig. 5.11 shows the charge efficiency in each sub-sample.

The main background source is due to cosmic ray events faking neutrino interactions. The background to "internal events" has been discussed at length in section 4.4, where we have shown how it can be kept under control. The main background to "external events" is due to through-going cosmic muons to which a wrong flight direction is assigned. If these muons enter from a dead zone of the detector, an up-going stopping muons is faked, an up- through-going muon is faked otherwise. These background events are mainly long tracks with several layers hit. The probability that a wrong flight directions is assigned to them is predicted to be correspondingly small. The contamination to the sample of stopping external muons, due to partially contained down-going neutrino interactions will not exceed the 1% level, if the time-of-flight, the hadronic activity at the muon end and the track curvature are considered. In the following, all background sources have been ignored.

The two alternative hypotheses under test (ν_μ-ν_τ versus ν_μ–ν_s) are composite since both of them depend on unknown oscillation parameters ($\sin^2 2\Theta$ and Δm^2). To simplify the statistical treatment of the data we have adopted pure χ^2 tests. Two independent test-statistics have been considered: the first one is charge-independent and compares the total event rates in the energy and zenith angle plane to the expectations; the second one measure the rate asymmetry of positive and negative muons, which is expected to appear if ν_μ–ν_s oscillation with non-maximal

[4] The angular region corresponds to the "vertical" through-going sample selected by Super-Kamiokande

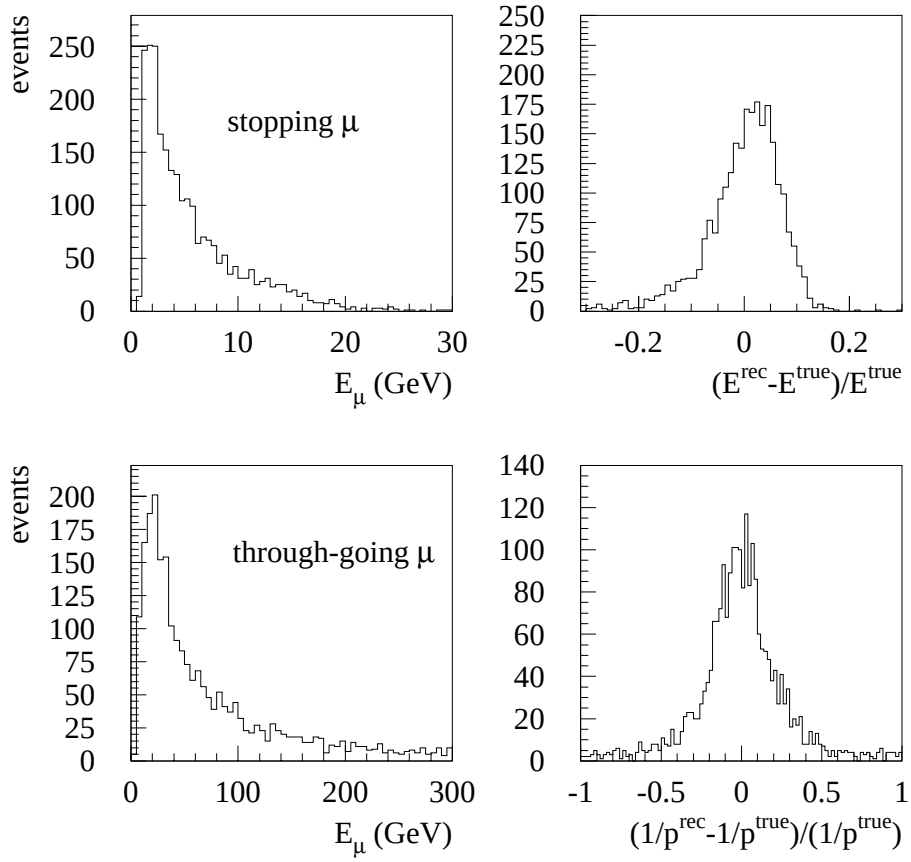

Figure 5.10: Momentum spectra and resolution for stopping and through-going external muons. The muon momentum is measured from the visible range (stopping muons) or from the track curvature in the magnetic field (through-going muons).

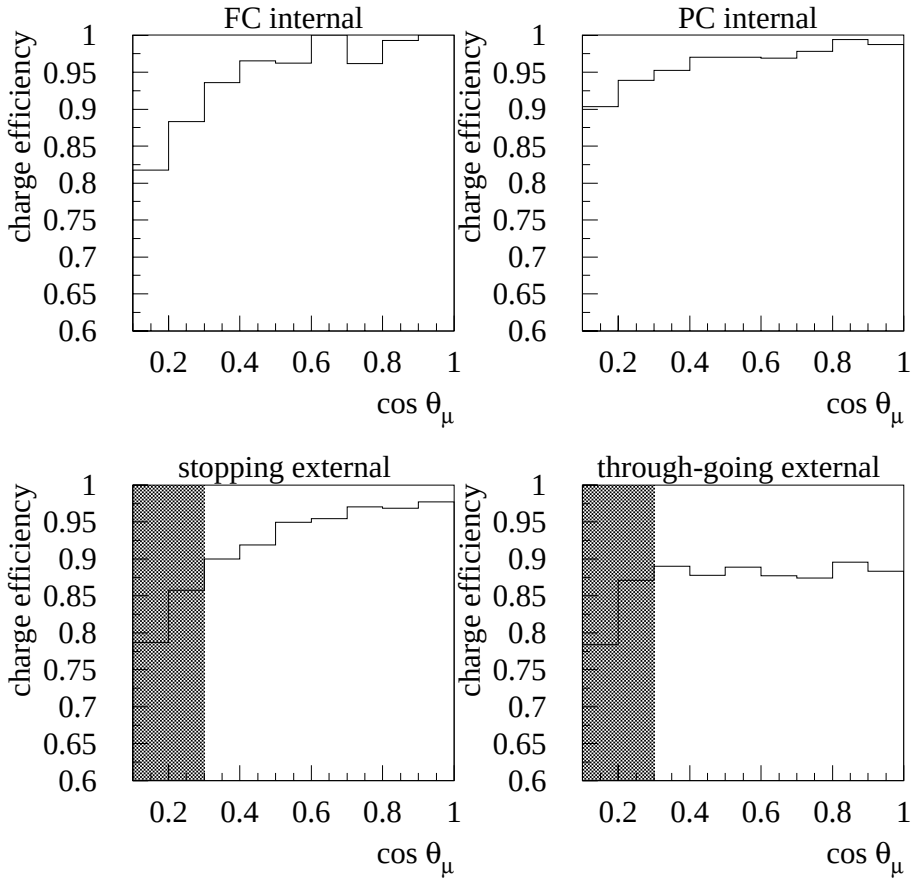

Figure 5.11: Charge identification efficiency for internal and external events. All the cuts have been applied but the angular cut in the "external events" sample. This cut rejects approximately the region in the hatched box.

mixing are present.

In the charge-independent approach, the distribution of selected events has been binned in the $(E_\mu, \cos\theta_\mu)$ plane: two energy bins ($E_{min} < E_1 < 15$ GeV and $E_2 > 15$ GeV) and five (four) angular bins for the internal (external) sample have been used. Positive and negative muons have been summed together and a χ^2-statistics has been defined which compares the observed event rates in the simulated experiments to the expectations for either hypothesis.

In the charge-dependent approach, only two energy and two angular bins have been considered both for internal and external events. A χ^2 statistics of the rate asymmetry between positive and negative muons as been defined as follows:

$$\chi^2 = \sum_{i=1}^{N_{bins}} \frac{\left[\left(\frac{N_i^{d+}}{N_i^{0+}} - \frac{N_i^{d-}}{N_i^{0-}}\right) - \left(\frac{N_i^{mc+}}{N_i^{0+}} - \frac{N_i^{mc-}}{N_i^{0-}}\right)\right]^2}{\left[\frac{N_i^{mc+}}{(N_i^{0+})^2} + \frac{N_i^{mc-}}{(N_i^{0-})^2}\right]} \tag{5.12}$$

where N_i^{d+} (N_i^{d-}) is the observed number of μ^+ (μ^-) events in the i-th bin; N_i^{0+} (N_i^{0-}) is the expected number of μ^+ (μ^-) events in the i-th bin in the occurrence of no oscillation and $N_i^{mc+} \equiv N_i^{mc+}(\sin^2 2\Theta, \Delta m^2)$ (and correspondingly N_i^{mc-}) is the expected number of μ^+ (μ^-) events in the i-th bin for given values of $\sin^2 2\Theta$ and Δm^2. Therefore, the quantity

$$\frac{N_i^{mc+}}{N_i^{0+}} - \frac{N_i^{mc-}}{N_i^{0-}}$$

is the expectation of the charge asymmetry for the hypothesis under test. Clearly, for pure ν_μ–ν_τ oscillations this asymmetry is zero for any value of $\sin^2 2\Theta$ and Δm^2.

The set of oscillation parameters for either hypothesis which minimise the χ^2 has then been determined by comparing the observed event rates in the simulated experiments to the expectations. A Monte Carlo reweighting technique has been adopted to predict the shape of the $(E_\mu, \cos\theta_\mu)$ distributions including the experimental resolution for each value of oscillation parameters and for the two alternative scenarios [93]. In general, the best-fit of the two hypotheses is achieved for different values of the oscillation parameters.

Several MONOLITH experiments of four years each have been simulated under different assumptions for the oscillation scenario to test the statistical properties of the test-statistics. In particular, it has been checked that the distribution of the test-statistics for the null hypothesis be consistent with a central χ^2-distribution and that consistent estimates of the oscillation parameters for the null hypothesis be obtained after χ^2 minimisation.

Fig. 5.12 shows the probability density function of the experimental outcome for the charge-independent test-statistics for either hypothesis in case of ν_μ–ν_τ oscillations with maximal mixing and for two values of Δm^2 (null hypothesis). As expected (see equations (5.10) and (5.11)), the separation improves at small values of Δm^2: at $2(4) \cdot 10^{-3}$ eV^2 for a 90% C.L. on the null hypothesis (ν_μ–ν_τ), there is a 0.5% (29%) probability that the alternative hypothesis be also consistent with the experimental outcome.

The dependence on Δm^2 of the discrimination capability of this analysis is summarised in fig. 5.13. Here, a ν_μ–ν_τ oscillation with $\sin^2(2\Theta) = 1$ or $\sin^2(2\Theta) = 0.9$ and Δm^2 ranging from 10^{-3} to $8 \cdot 10^{-3}$ eV^2 (see figure) has been assumed as the null hypothesis. The vertical axis of the plot represents the χ^2-probability of the expectation value of the χ^2 corresponding to the best-fit for the alternative hypothesis (ν_μ–ν_s). For each set of oscillation parameters, these expectation values have been computed from the average of fifty experiment simulations.

In summary, Earth-induced matter effects alone provide a very effective mean of separating oscillations into τ or sterile neutrinos for low values of Δm^2. For values higher than about $3 \cdot 10^{-3}$ eV^2, low energy events (mainly internal events) are of little use to distinguish between the

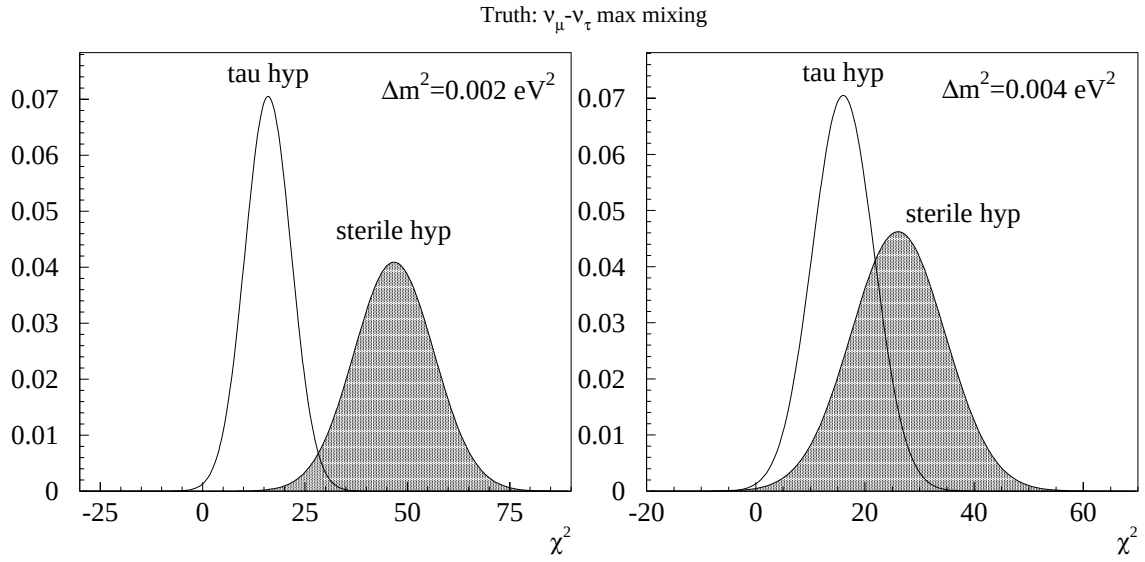

Figure 5.12: Probability density function of the experimental outcome for the charge-independent test-statistics under the null (ν_μ–ν_τ) and the alternative (ν_μ–ν_τ) hypotheses. Simulations correspond to ν_μ–ν_τ oscillations with $\Delta m^2 = 2 \cdot 10^{-3}$ eV^2 (left) and $\Delta m^2 = 4 \cdot 10^{-3}$ eV^2 (right) and maximal mixing.

two alternative hypotheses, since matter effects roughly scale as $E_\nu/\Delta m^2$. The discrimination power is deteriorated accordingly, since it relies only on the external sample.

For mixing lower than maximal, the discrimination capability of the charge-independent analysis worsens. An improved discrimination power is achieved from the study of the charge asymmetry. Results of the charge-dependent analysis are summarised in figure 5.14. Here, we have assumed that ν_μ–ν_s oscillation occur with $\sin^2 2\Theta = 0.8$ (null hypothesis). Fifty MONOLITH experiments for Δm^2 in the range $1\text{–}8 \cdot 10^{-3}$ eV^2 have been simulated. The figure shows the χ^2-probability of the expectation value of test-statistics corresponding to the best-fit for the alternative hypothesis (ν_μ–ν_τ). The results of the charge-asymmetry and the charge-independent analysis are compared. The impact of charge misidentification is also shown.

Noteworthily, the charge-asymmetry alone is more powerful than the charge-independent analysis, which would not be powerful enough to discriminate between the two hypotheses for a mixing parameter this low. The two test-statistics are independent and can be combined.

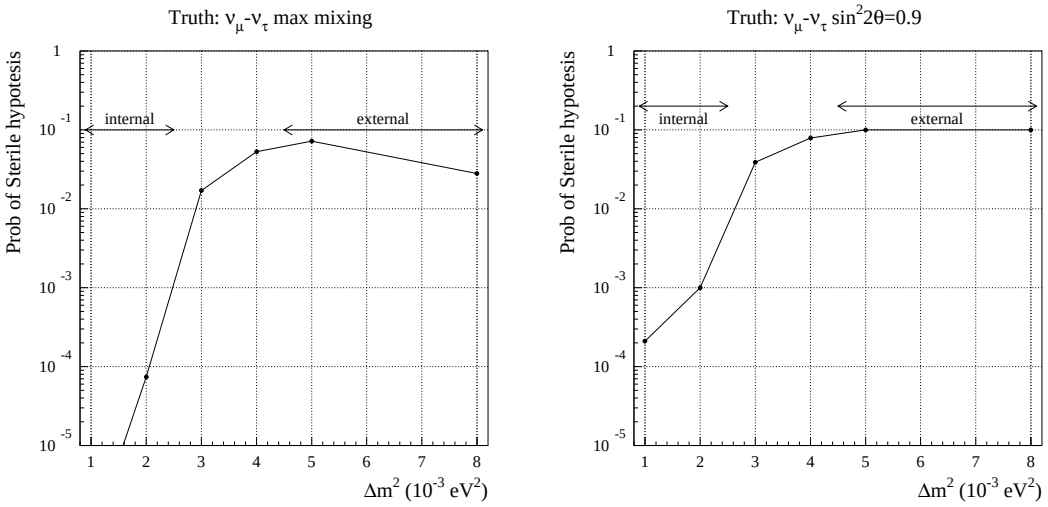

Figure 5.13: χ^2 probability of the expectation value of the χ^2, i.e. $Prob(\langle\chi^2_{sterile}\rangle)$, corresponding to the best-fit of the alternative hypothesis, when ν_μ–ν_τ with maximal mixing (left) or $\sin^2(2\Theta)$ (right) are simulated. For values of the ν_μ–ν_τ mass differences lower than $3 \cdot 10^{-3}$ eV^2 the internal events bring most of the information; for values higher than $\sim 5 \cdot 10^{-3}$ eV^2 the external events dominates.

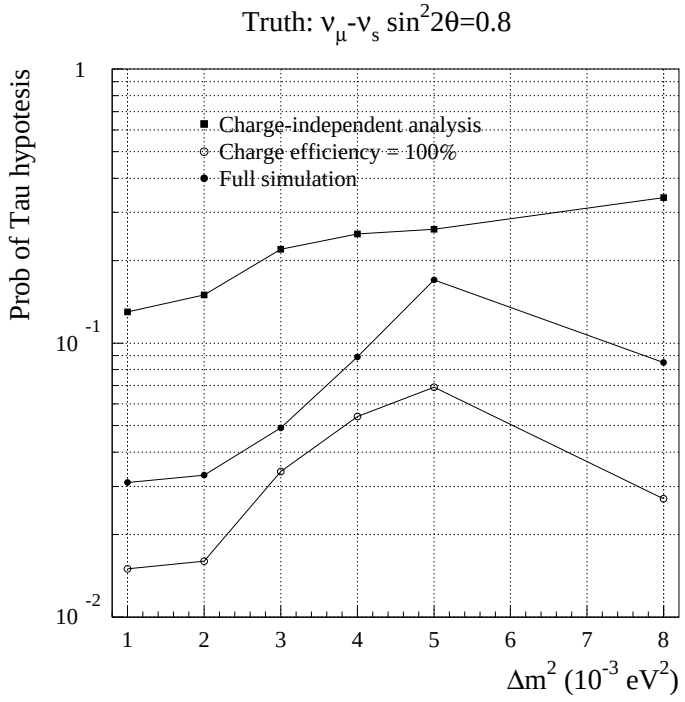

Figure 5.14: χ^2-probability of the best-fit for the alternative hypothesis (ν_μ–ν_τ), when ν_μ–ν_s oscillations with $sin^2 2\theta = 0.8$ are simulated. Full and empty circles represent the results obtained using the charge-asymmetry alone. The corresponding result obtained from the charge-independent analysis.

5.4 Summary and conclusions

By exploiting the high energy component of the atmospheric muon neutrino fluxes, this experiment has the capability to detect the oscillation pattern from the comparison of L/E spectra of upgoing and downgoing neutrinos. The outlined analysis takes advantage of the up/down symmetry of the high energy atmospheric neutrino fluxes, which makes high energy atmospheric neutrinos an ideal source for disappearance experiments.

In the apparatus considered, the determination of the neutrino energy and direction relies mostly on the muon reconstruction. By means of the measurement of ν_μ disappearance, the existence of oscillations can be (dis)proved and the parameters measured over the entire range suggested by Super-Kamiokande and Kamiokande results (see fig. 5.5). Moreover, unconventional models still consistent with Super-Kamiokande data can be discriminated by the observation of the oscillation pattern.

The comparison of rates of upward and downward muon-less events of high energy will allow to discriminate between oscillations into a sterile or a τ neutrino. A full simulation and analysis has been performed. For $\Delta m^2 \geq 3 \times 10^{-3}$ eV^2, a separation at the 3σ level is within the reach of this experiment (see Fig. 5.9). For lower values of Δm^2 the separation of the two hypotheses is marginal, since the high energy component of the atmospheric neutrino fluxes does not oscillate enough.

In this region, however, the use of Earth-induced matter effects provides an effective way to discriminate between $\nu_\tau - \nu_s$ oscillations (see section 5.3.2), thanks to the MONOLITH capability to measure muon momenta up to several hundred GeV. There is a nice complementarity between this method, most efficient for low values of Δm^2, where matter effects are important, and the one based on muon-less events, which is efficient for large values of Δm^2. The two approaches are at any rate statistically independent and the discrimination capabilities can be combined.

Moreover, we have shown that the capability of a magnetised detector to separate the ν and $\bar{\nu}$ component, from the measurement of the muon charge can be exploited. This gives an additional signature for matter effects and has been shown to be relevant for $\nu_\tau - \nu_s$ discrimination in the low-mixing angle regime ($\sin^2(2\Theta) \sim 0.8$), where the charge-independent signature might not be sufficient.

Chapter 6

Physics with the CERN to Gran Sasso neutrino beam

In addition to atmospheric neutrinos, for which it has been optimized, MONOLITH will also detect more than 100000 events (CC+NC) per year from the CERN to Gran Sasso (CNGS) neutrino beam, which is scheduled to start operations in 2005. In this chapter, we present a qualitative study of the MONOLITH performance in this beam. A full quantitative study needs a detailed understanding of the beam systematics, which is not yet completed.

Beam neutrinos arrive at an angle of 4° (upward) from the horizontal direction, almost parallel to the "long" axis of the MONOLITH detector. Despite its optimized design for atmospheric neutrinos, the MONOLITH detector in its uniformly horizontal option can reconstruct $\approx 46\%$ of the CC events with optimal energy resolution. In terms of events, this result makes MONOLITH the detector which will monitor the CNGS beam with highest statistical precision and good energy resolution ($\approx$ 41000 events/year expected to be reconstructed with energy resolution $\leq 22\%$). This huge sample can complement the MONOLITH atmospheric neutrino analysis of the L/E distribution in the region (20-200) km/GeV. The remaining part of the data is reconstructed with less precision, but can still be used for flux monitoring purposes.

To further improve the beam performance, the detector can be equipped with vertical end caps. The performance of this end-cap option is also investigated and the gain in terms of efficiency with respect to the uniform detector option is discussed.

6.1 Detector and beam simulations

The reference detector layout considered in the simulation ("uniform detector option") has been already discussed in Chapter 4 and is shown in Fig. 4.1. At variance with the baseline option considered in the MONOLITH Progress Report [1], in this layout the field lines are perpendicular to the CNGS beam direction, bending tracks out of the iron plates. This feature is very helpful for the reconstruction of events from the CNGS beam.

Charged current interaction of neutrinos from the CNGS beam have been simulated using the same generator adopted to describe atmospheric neutrino interactions [75, 76] (see section 4.3.1). The neutrino energy has been sampled from the reference CNGS beam spectrum [29]. To estimate the number of events we assumed 5×10^{19} pot/year. The input cross-section weigthed spectrum is shown in Fig. 6.1. The events have then been processed by the GEANT3 simulation of the MONOLITH detector.

As an example we show in Fig. 6.2 a 43 GeV event interaction inside MONOLITH, where the reference system is also shown: the Y-axis is along the Hall axis and parallel to the beam.

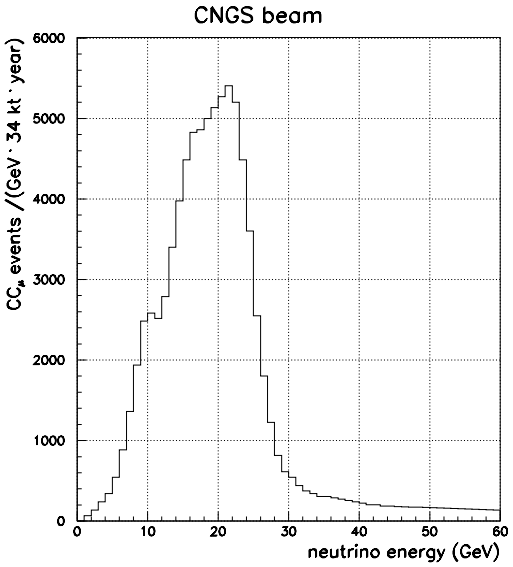

Figure 6.1: Number of charged current ν_μ interactions in MONOLITH from CNGS beam in 1 year

6.2 Reconstruction and event selection

Muons produced by ν_μ-CC interactions of CNGS beam neutrinos develop along the iron layers and may travel a sizeable distance inside them before they are bent out by the magnetic field. A precise measurement of their momentum can be obtained either from range of from track curvature, provided a good estimate of the vertex position is available. Therefore, events have been required to have at least one hadronic hit (i.e. not belonging to the muon). Taking the first y-hit as the vertex position, we obtain the vertex resolution shown in Fig. 6.3. Despite the coarse granularity of the detector, resolutions of the order of 5 cm on the vertex position is achievable on each coordinate. Small systematic errors on Y and Z, due to the beam direction (neutrinos are emerging with an angle of 4^o from the horizon) have been *a posteriori* corrected for.

For the analysis, the ν_μ-CC events have been divided in partially contained (PC) or fully contained (FC) depending if the muon track is exiting the detector or not. In Fig. 6.4 the fraction of FC events as a function of neutrino energy is shown. For the full detector (Y-length 30 m) the fraction of FC events is larger than 50% till $E_\nu \approx 35$ GeV.

As for atmospheric CC ν_μ interaction, for FC events the muon energy reconstruction is based on the range technique. Requiring at least 7 hits to belong to the muon track, the muon momentum is reconstructed with an average resolution near 8% as shown in Fig. 6.5, nearly constant with the energy. Some pathological bad reconstructed events (see tails on the distribution, at some % level) still need to be fixed.

For partially contained (PC) events with an outgoing muon track, the muon momentum has been reconstructed fitting the track curvature in the magnetic field.

Due to the fact that event directions are near the horizontal and along the Y-axis of the detector, an optimised reordering of recorded hits have been implemented. In practice, the two selected views to analyze the events are the ZY and XY ones, no more (as for atmospheric neutrino) XZ and YZ, after suitable rearranging of hits.

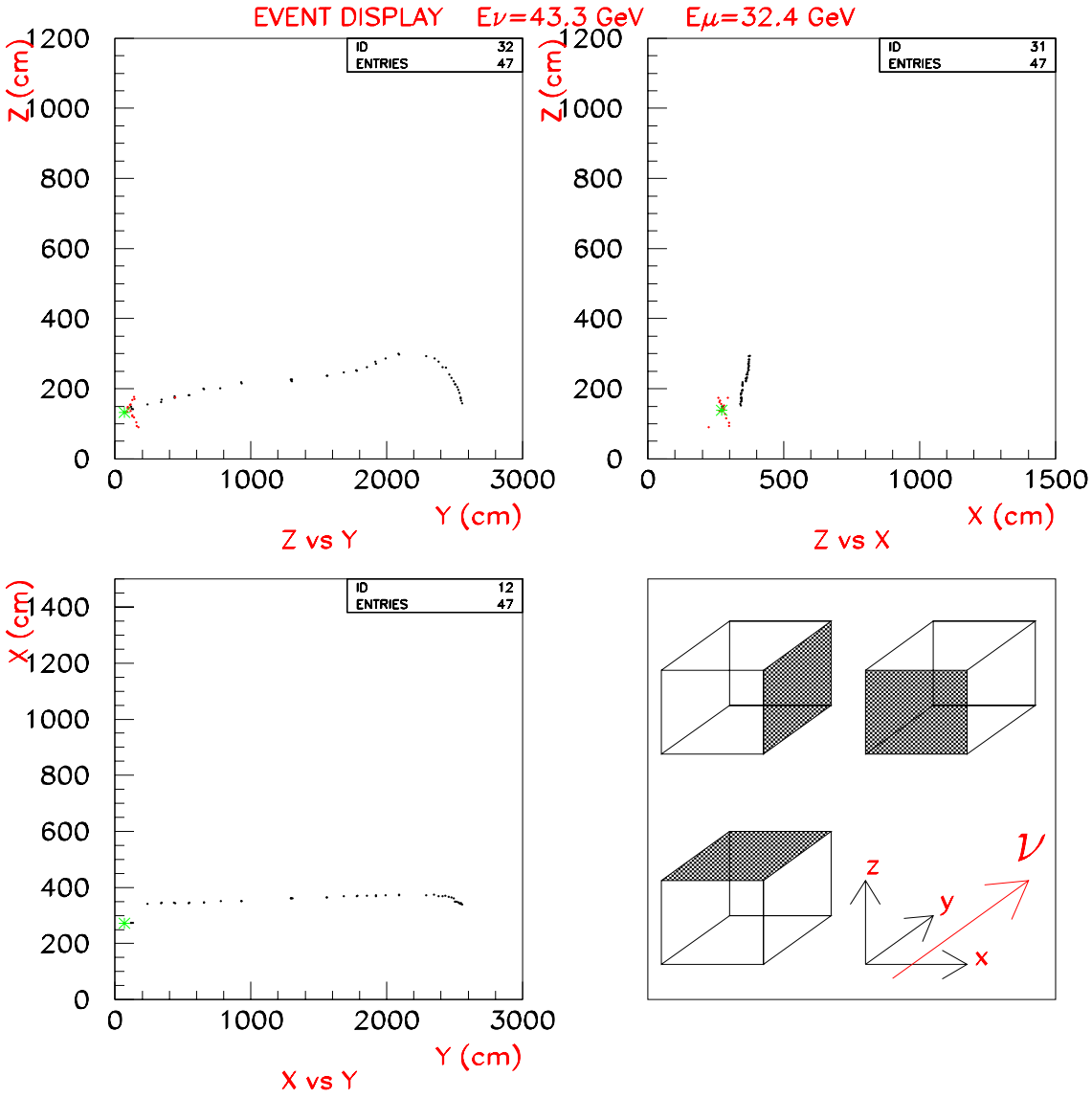

Figure 6.2: A 43.3 GeV charged current ν_μ interaction from CNGS beam inside MONOLITH.

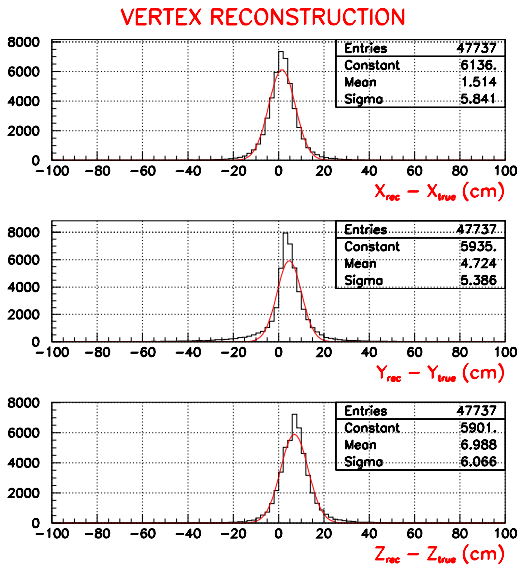

Figure 6.3: Errors on reconstructed vertex position.

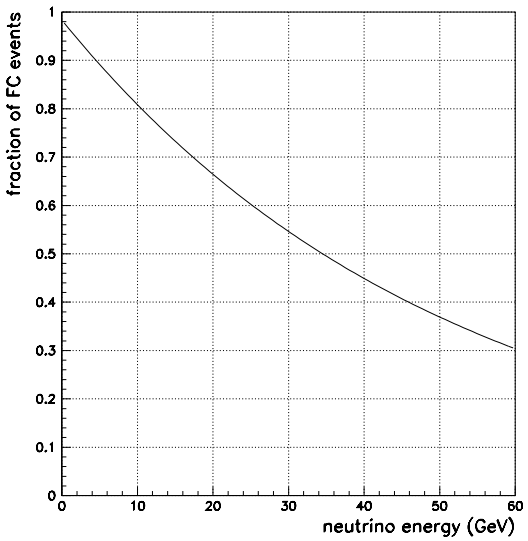

Figure 6.4: Fraction of FC charged current ν_μ interactions from CNGS beam as a function of neutrino energy.

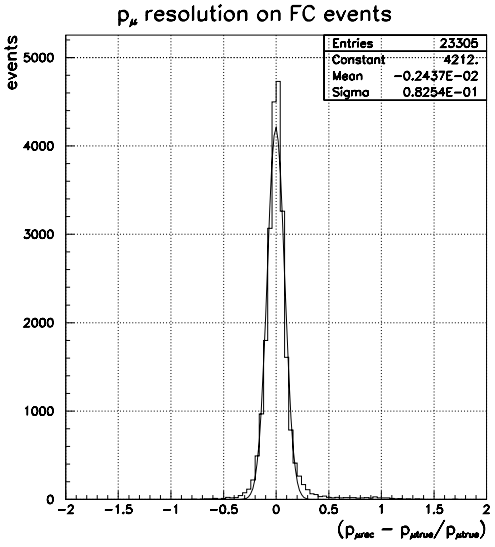

Figure 6.5: Resolution on reconstructed muon energy for FC events.

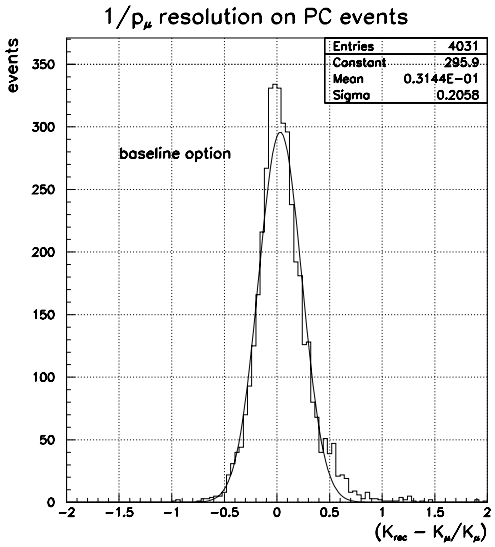

Figure 6.6: Resolution on reconstructed 1/p muon momentum for PC events.

The first stage of the reconstruction of muon momentum in the magnetic field, is to define a *candidate track*, that is a collection of hits in the two projections ordered along the y-axis. Each projection is modeled through a polinomial fit of order n, with $1 < n < 7$ depending on the number of hits in the projection. This track model is used to get the initial starting track directions dx/dy and dx/dy. These, together with the first hit x and z coordinates and a rough momentum estimate using the range, are the input to the track fit, based on a Kalman-filtering technique. Two tracking are performed on a candidate track: the first starts from the muon hit closer to the interaction point and follows the track up the last hit. The track parameters fitted at the end track point are then used as new starting values for a backtracking, which now proceeds to the muon hit closer to the vertex. The fit parameters (the two coordinates x and z, the two derivatives dx/dy and dz/dy and the signed inverse momentum K=q/P, with q = $\pm$1) are therefore provided in the innermost point, closer to the interaction vertex. The average tracking in the magnetic field and covariance error matrix propagation are done using GEANE [95]. More details are given in ref. [94].

The fitting procedure provides, for each event, an estimate of the error σ_K on the reconstructed $K = 1/p$. For PC events, we select events with a $\sigma_K/K \leq 30\%$: the resolution reached for the uniform detector option on the PC sample is shown in Fig. 6.6. No explicit request on the number of hits have been made: however we checked that for selected tracks events with less than 7 hits are less than 8%.

On the PC sample selected, the resulting muon momentum resolution in the range of interest (0.- 60 GeV) is shown in Fig. 6.12 with full points for the uniform detector option. The resolution improves with muon energy because, due to the beam orientation with respect to the main detector axis, the selection of outgoing muons of increasing energy correspond to an increasing number of hit collected and a larger integrated magnetic field by the track.

An hadronic energy reconstruction has been derived from the number of hits released by hadrons produced in neutrino interactions using MONOLITH as a digital calorimeter. A calibration curve optimised for the beam, slightly different from the one used, for atmospheric neutrino interaction has been developed. The hadronic energy resolution is found to agree with the parameterisation of the hadronic energy resolution estimated on atmospheric neutrinos

events (see section 4.2.2).

On long-baseline events the resolution on L/E will be determined by the neutrino energy resolution. As for atmospheric neutrino analysis even with a coarse resolution to hadrons, the overall L/E resolution can be controlled by selection of neutrino interactions of limited inelasticity for small neutrino energies. From the expression of the relative L/E resolution (3.2), we have

$$\frac{\sigma(L/E)^2_{beam}}{(L/E)^2} = \frac{\sigma^2_E}{E^2} \simeq \frac{\sigma^2_{E_\mu}}{E^2_\mu}(1-y)^2 + \frac{\sigma^2_{E_h}}{E^2_h}y^2 \tag{6.1}$$

where E, E_μ and E_h are the neutrino, muon and hadronic energies, $y = E_h/E$ is the inelasticity of the interaction. So, for each event selected, we have estimated E_μ, E_h and y. Using eq. (6.1), and parametrisations of $\sigma(E_\mu)$ and $\sigma(E_h)$, we evaluate the relative $\sigma(L/E)$ on an event by event basis. We select the events for the analysis requiring $\sigma^2(E) \leq k^2E^2$, where we choose $k = 0.3$ as a compromise to mantain a global neutrino energy resolution less than 22% and good selection efficiency.

Summarizing, we select a sample for the analysis using three cuts:

1. the request of an hadronic hit to fix the vertex;
2. a request of at least 7 hits for the muon track for FC events or a request of good fit of the track for PC events;
3. the above discussed cut on the expected neutrino energy resolution.

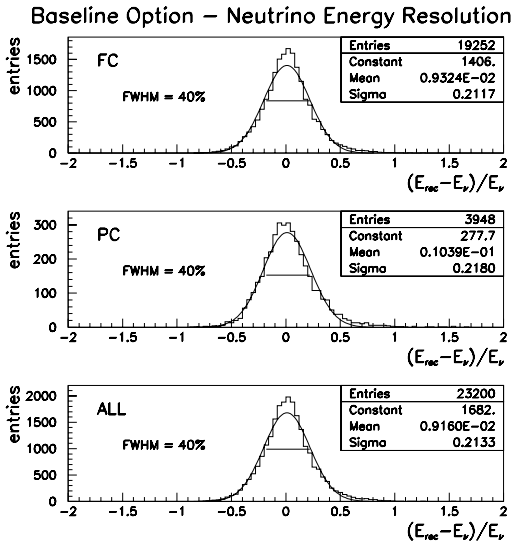

Figure 6.7: Resolution on reconstructed neutrino energy for the MONOLITH uniform detector option.

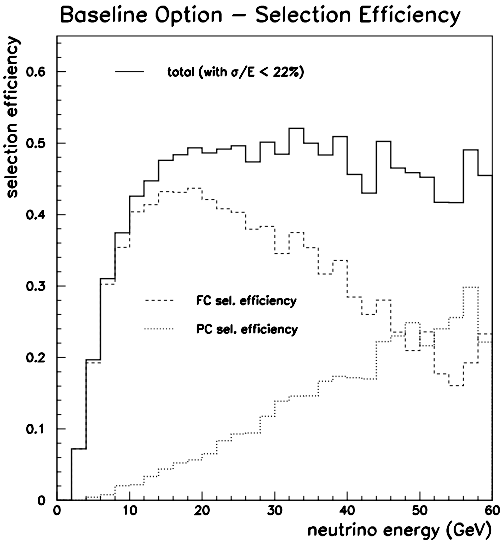

Figure 6.8: Selection efficiency for the MONOLITH uniform detector option for the discussed cuts.

6.2.1 Results for the uniform detector option

For the uniform detector option the neutrino energy resolution for PC, FC and the whole set are shown in Fig. 6.7. A neutrino energy resolution $\leq 22\%$ is achieved (an analysis of the FWHM due to the not perfect gaussian shape gives something better around 17%). The selection efficiency for the range 0-60 GeV is plotted in Fig. 6.8. It is defined as the ratio between the number of selected events and the generated one in a given bin of energy. From 16 GeV to 40 GeV nearly constant selection efficiency around 50% is obtained.

6.2.2 Results for the vertical end-caps option

We have also studied the configuration with the addition of some vertical iron planes to the MONOLITH uniform detector option to increase the efficiency on the CNGS beam.

To maintain a symmetric detector (taking into account that vertical planes can be also used successfully for atmospheric neutrinos as shown in [1]), we investigated the performance of the setup shown in Fig. 6.9. Basically the horizontal plate dimensions are reduced to (26x15) m^2 and two 2 m long end caps are added at the beginning and at the end of the Y axis, made by vertical iron plates and GSC's. Assuming the "standard" MONOLITH spacing (e.g. 8 cm of iron, 2 cm to host GSCs) every endcap gives 20 active layers. In this configuration we have exactly the same total mass of the uniform detector option. We assume also the same design of the magnetic field for the iron plate of the uniform detector option.

The resolution and efficiencies achievable with this configuration are shown in Figg. 6.10 and 6.11. Of course the main gain is due to the increased efficiency for PC events, where outgoing track are best reconstructed due to the contribution of the last 20 vertical layers.

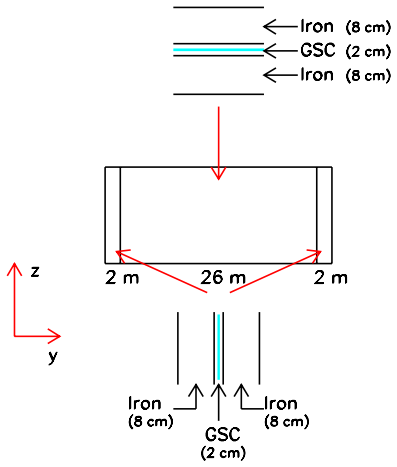

Figure 6.9: Side view of MONOLITH with the end-caps option.

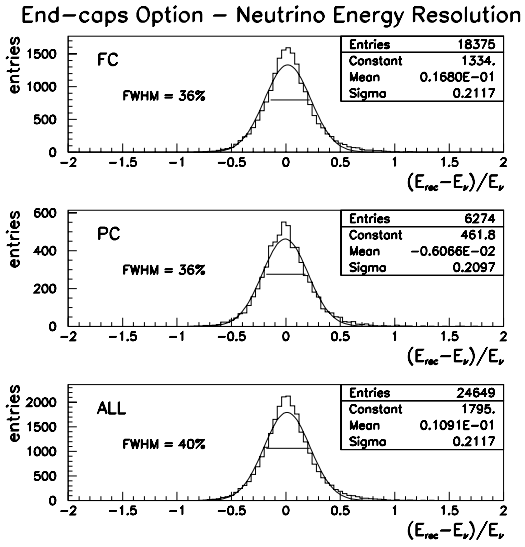

Figure 6.10: Resolution on reconstructed neutrino energy for the MONOLITH end-caps option.

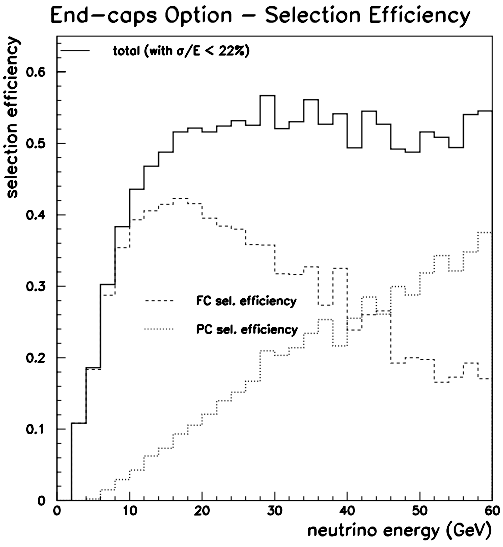

Figure 6.11: Selection efficiency for the MONOLITH end cap option for the discussed cuts.

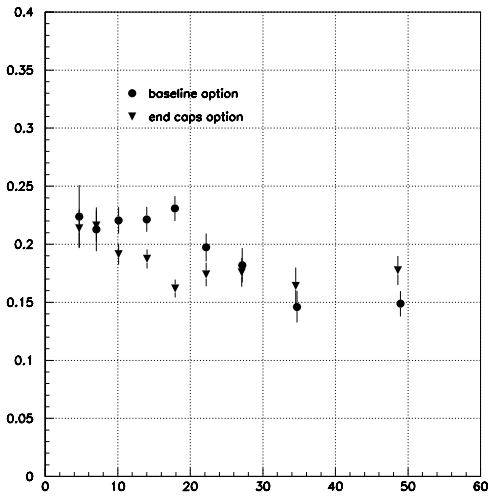

Figure 6.12: Resolution on reconstructed 1/p muon momentum as a function of muon energy for PC events in the two options.

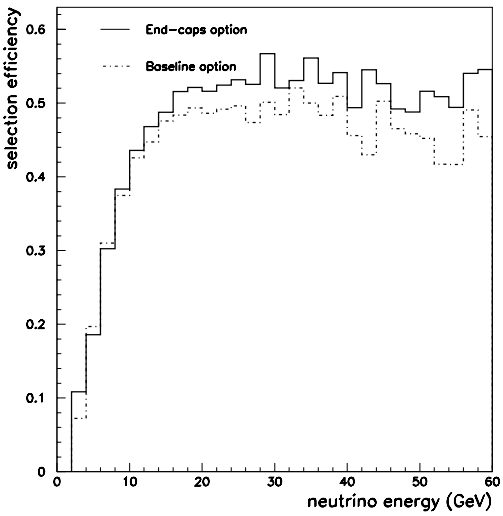

Figure 6.13: Comparison of the selection efficiency for the two options.

6.2.3 Comparison of the two set-ups

In Fig. 6.12 with full triangles the σ_K resolution is reported compared with the uniform detector option (full circles). Better resolution at smaller energies for outgoing tracks is obtained with the end caps.

In Fig. 6.13 the selection efficiency for the two setup is compared. As can be seen the vertical plates add efficiency and give a more flat behaviour at higher ($E > 40$ GeV) energies. A 10% increase of the selection efficiency with respect to the uniform detector option is obtained at 30 GeV. At higher energies (see Fig. 6.1) the beam intensity is rapidly decreasing, but we point out that this region is relevant to select an unoscillated sample of data, needed to normalize correctly the total luminosity of the beam.

6.3 Study of the oscillation pattern

In Fig. 6.14 we present the L/E distribution (no oscillation) measurable from the CNGS beam by MONOLITH in 1 year of data taking. The hatched area is the statistics that MONOLITH will collect from atmospheric neutrinos in 4 years of data taking (values of L for downgoing neutrinos have been mirrored).

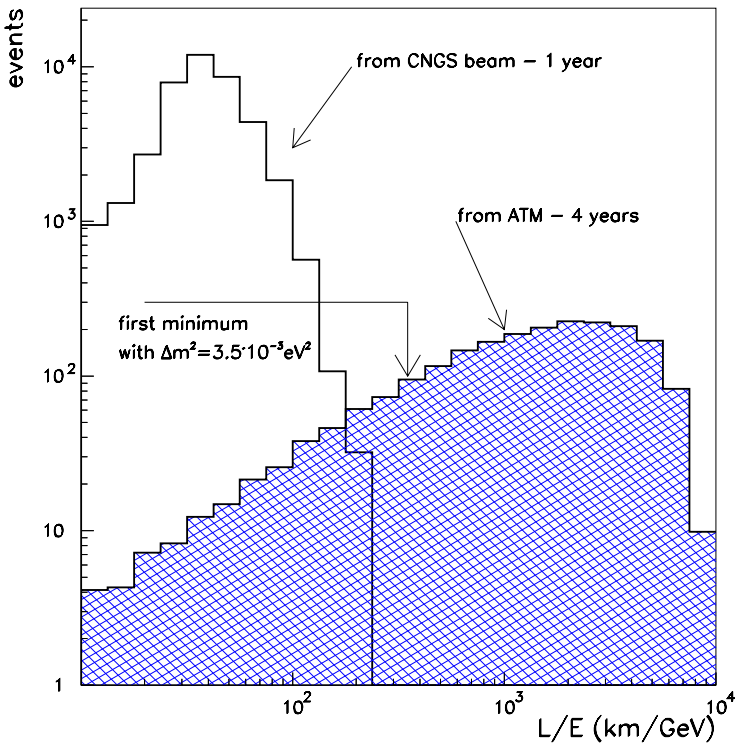

Figure 6.14: Number of events selected for the analysis by MONOLITH in 1 year of data taking from the CNGS beam. The statistics from atmospheric neutrinos is also shown.

Considering the most probable value of the first minimum of the oscillation pattern, according to current Super Kamiokande best fit, the complementarity of the two measurements becomes clear: the L/E data obtained by the CNGS beam will provide many events in the L/E region before the oscillation minimum, and can help to constrain the oscillation pattern in this region.

In Fig. 6.15 the measurable L/E distributions with respect to the expectations have been plotted for five different values of Δm^2 and maximal mixing. The survival probability convolved with the resolution function is also superimposed. To obtain the unoscillated expected distribution, after correction for the selection efficiency and the energy resolution smearing, we used the events from the CNGS beam with energy between 35 and 50 GeV, expected to be nearly completely unoscillated. The errors shown are computed assuming the *relative* beam shape and detector efficiency to be known at the 8% level. A more detailed study of the systematic error is needed to obtain quantitative fit results.

Finally, these measurements can be merged with atmospheric neutrino measurements to yield combined spectra like the one shown in fig. 2.3. This figure has been obtained from a fast simulation using a simplified detector parametrization (Appendix B). Analysis of equivalent

spectra with the full simulation is in progress.

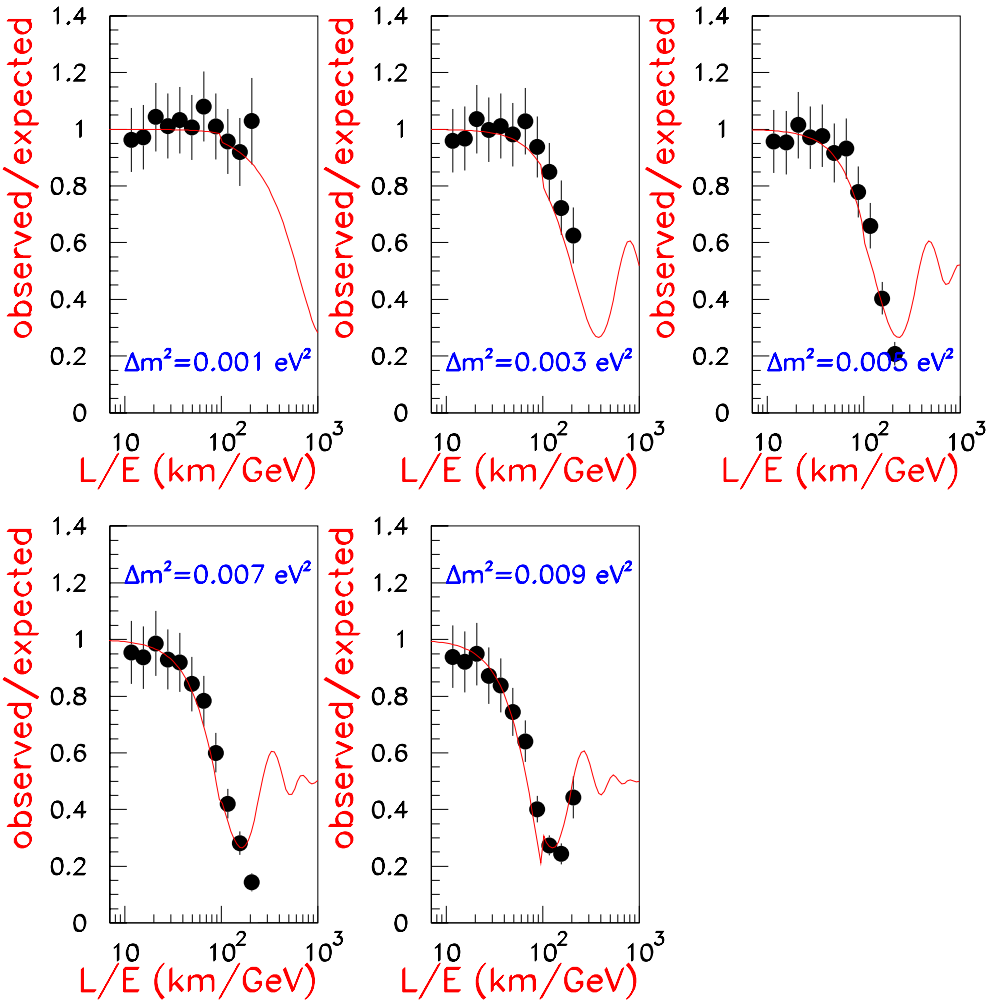

Figure 6.15: L/E distribution from the CNGS beam for five different values of Δm^2. To help following the shape, the survival probability is also superimposed.

6.4 Conclusions

- the MONOLITH experiment can act as a good quality monitor of the CNGS beam;
- despite its design being optimised for atmospheric neutrinos, even the uniform detector option will allow to collect a huge amount of events from the beam with good resolution. An addition of vertical plates can increase the selection efficiency, in particular for $E_\nu \geq 15$ GeV;
- the up/down analysis of MONOLITH from atmospheric neutrinos can be complemented by a big sample of data from the CNGS beam at small L/E to reduce statistical errors. Albeit this will make the analysis dependent on Monte Carlo and beam systematics, it will probably yield a useful complement and/or redundant consistency check for the first years of data taking;
- depending on Δm^2 and assuming a 8% systematic uncertainty in beam shape, a deficit of events as a function of L/E can be seen in 1 year of data taking. However, the systematic uncertainty due to the beam shape knowledge needs to be further investigated.

A global fit of atmospheric and beam data is under study to quantify the improvement that can be achieved. Further investigations are also needed to improve the reconstruction technique of the beam events, in particular to study the charge identification efficiency. This is relevant both to study background $\bar{\nu_\mu}$ component inside the CNGS beam and to evaluate possible capabilities of MONOLITH to identify "wrong-sign" muons inside beams from ν factories.

Chapter 7

Physics with high energy cosmic rays

As outlined in chapter 2, MONOLITH can make significant physics contributions to cosmic ray muon studies in the the multi-TeV energy range, including investigations of the cosmic ray knee, and of conventional contributions to the high energy muon spectrum. In this chapter, the measurement technique to achieve these goals is explained, and its application to these topics is discussed.

7.1 The pair meter technique for TeV muons

The size and the structure of the MONOLITH detector allow to utilise a new method of muon spectrometry in the TeV energy range. The technique is based on the energy dependence of the cross section of direct electron-positron pair production by muons. The idea of the technique was suggested in [97]. In passing through a thick layer of matter, high-energy muons produce secondary cascade showers, mainly via electron-positron pair production process. Measurements of the number and energies of these cascades allow to evaluate the muon energy.

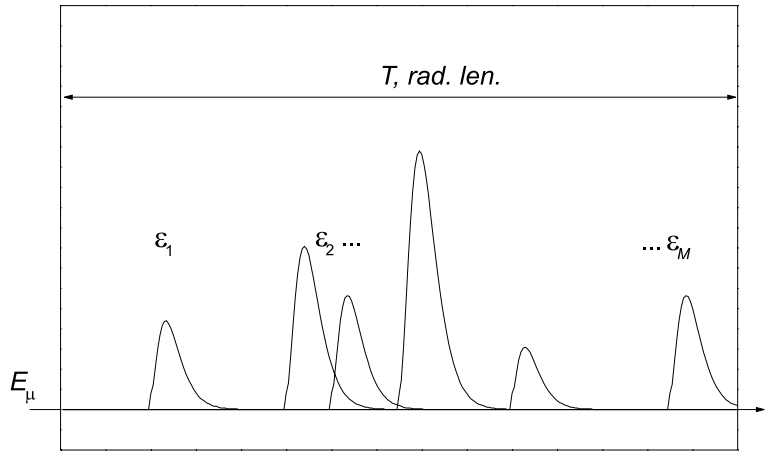

Figure 7.1: Idealised model of the pair meter. The creation of high energy electron-positron pairs leads to a series of clusters with energies ϵ_1 to ϵ_m along the track. If the path length in terms of the number of radiation lengths T is sufficiently large, the number and energy distribution of these clusters can be directly related to the muon energy.

The idealised model of the pair meter (as a layer of matter capable to detect muon interactions above a certain energy transfer threshold) is illustrated in Fig. 7.1. The quantitative

theory of the technique, a brief summary of early attempts of its realisation and the potential of its application in cosmic ray and accelerator experiments are given in [98, 99]. The most important advantage of the technique in comparison with other existing methods of muon spectrometry is the absence of an upper limit on the measurable muon energy: the energy resolution is not deteriorated with increasing particle energy. The relative energy measurement error is determined mainly by the total target thickness T expressed in radiation lengths (X_0):

$$\delta_E = \sqrt{\frac{9\pi}{28\alpha T}} \simeq \sqrt{\frac{137}{T}} \tag{7.1}$$

where $\alpha = 1/137$ is the fine structure constant. The most informative region of energy transfers from the view-point of muon energy reconstruction is $\epsilon = (10^{-3} - 10^{-2})E_\mu$. Thus, to perform measurements in the energy range $E_\mu \sim 10$ TeV and higher, it is sufficient to detect secondary electromagnetic cascades with energies $\epsilon \sim 10$ GeV. Due to the fact that the technique is based on the observation of multiple interactions of muons in the setup material, it is rather tolerant with respect to individual cascade energy measurement errors, and may be implemented with a detector of a relatively simple structure.

7.2 Application to MONOLITH

Recently, the pair meter technique has been applied for investigations of cosmic ray muons at great depth underground [100] and for horizontal muons at the surface [101]. These experiments have demonstrated the feasibility of the technique and confirmed its basic theoretical propositions. However, the small thickness of the setups (80 X_0 in the NUSEX detector and 140 X_0 in the liquid-argon spectrometer BARS) and, correspondingly, a large uncertainty in the muon energy evaluation have only allowed to estimate spectrum model parameters on a statistical basis, by means of the comparison of the observed distributions of event characteristics with the expectation.

The thickness of the target in MONOLITH (500 X_0) provides the possibility to measure individual muon energies, and hence to obtain direct measurements of the energy and angular distributions of the detected particles. Examples of simulated events for several muon energies are given in Fig. 7.2. On average, a 10 TeV muon will generate (via electron pair production) 5 cascades with energies greater than 10 GeV and about 20 cascades above 1 GeV. For a 100 TeV muon, the typical number of cascades will already be 5, 20, and 50 for cascade energy thresholds 100, 10, and 1 GeV respectively, which will allow to estimate the muon energy with about 50% accuracy (and approximately log-Gaussian distribution of errors). Such accuracy is quite sufficient for muon energy spectrum studies. Depending on the amount of rock overburden, TeV muons detected in MONOLITH will have already lost a significant fraction of their initial energy (typically about 2/3). In this regime, the *fractional* energy loss depends only on the trajectory through the rock, and is independent of the muon energy. Since the direction of the muon is well measured, it can be calculated with sufficient precision. The spectrum measured in MONOLITH can therefore be reliably converted into the surface spectrum on an event-to-event basis.

The MONOLITH detector operated as a pair meter will have several thousand (!) times larger effective acceptance than the biggest magnetic spectrometers [102, 103], the results of which are still used as a standard of high energy muon spectrum measurements.

7.3 Conclusions

The application of the pair meter technique to the MONOLITH experiment will allow the first measurement of individual cosmic ray muon energies around 100 TeV. This measurements can

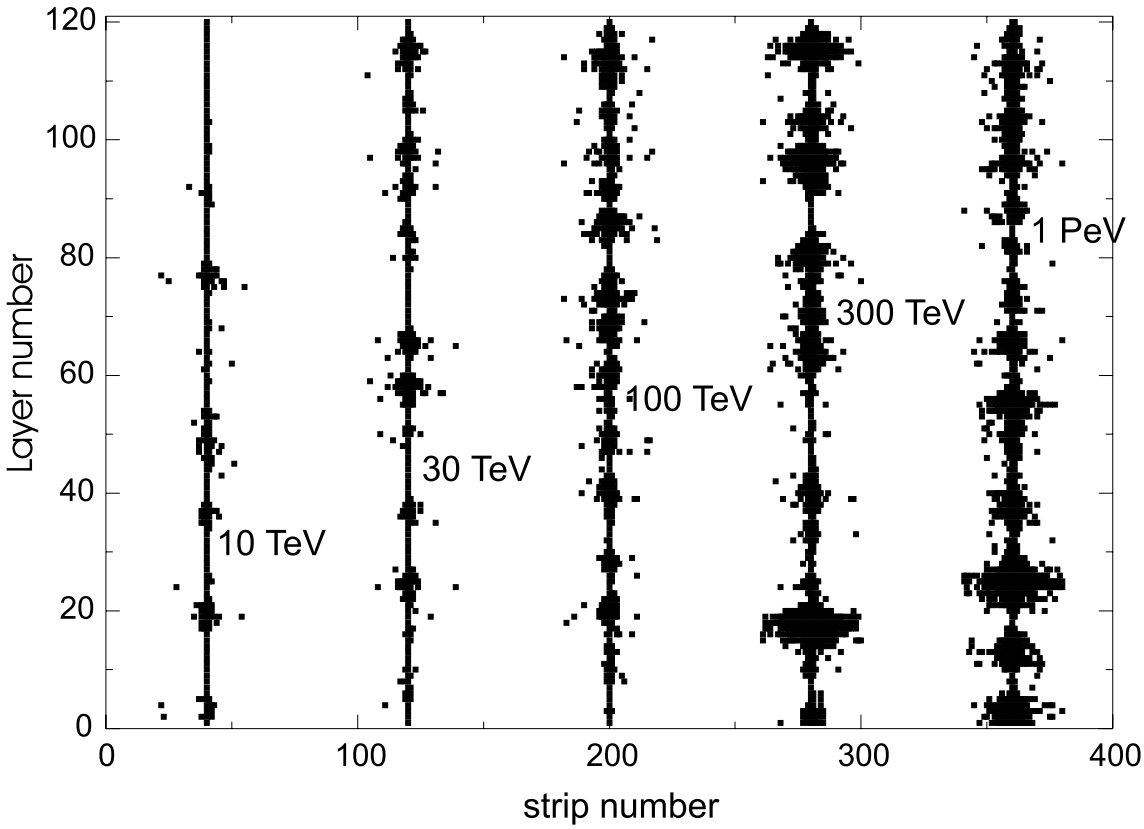

Figure 7.2: Muons with different energies in the MONOLITH digital calorimeter. 120 layers of 8 cm steel and 3 cm wide strips have been assumed in the simulation of the detector response.

be used to improve the knowledge of muon production mechanisms and of the primary cosmic ray spectrum and composition in the 100 TeV - 10 PeV region. Furthermore, it allows the search for an excess of VHE muons (> 100 TeV) which could lead, in the case of a positive outcome, to the discovery of new physical processes of muon generation in the several TeV centre-of-mass energy region. Negative results would allow to close discussions about the nature of the knee in the EAS spectrum, since only explanations related to a change of the primary spectrum change would remain.

Chapter 8

Planning and Cost

8.1 Space requirements and installation

A preliminary study of space availability in LNGS underground halls shows that a detector 30 m long, 14.5 m wide and 13 m high can be installed in hall C, in the space left free by the Borexino structures. The installation would comply with requirements for safety lanes, free access road for trucks to Borexino and full operationality of cranes. Along the length of the hall the detector would be positioned 1 m (safety lane) from the Borexino installation and would extend nearly 30 m (29.4 m) towards the main entrance of the hall. Main barracks and counting room would be installed 3.5 m above floor in the remaining space (4 m) between the detector and the entrance wall. The possibility of a lateral displacement of the main door of the hall has been considered and discussed with technical staff of LNGS. It is feasible, however it does not appear as strictly necessary, according to the present installation studies. The detector will be placed on iron foots, of appropriate size to comply with the maximum admitted specific load on floor. The access road to Borexino will be used, but not permanently occupied, during detector installation. The installation procedure will allow clearing the road on request, within a time to be defined with the LNGS Director. Trucks will be unloaded outside the hall; iron plates and materials will be carried in the hall on dedicated carriages. Storage space outside the hall, for material corresponding to two days of installation –namely: 30 plates corresponding to 135 tons weight and 20 cubic meters volume– would be helpful during installation.

The final dimensions of the detector and its characteristics will depend on some details, for instance mechanical tolerances, which are still subject to change. However, they will not result in significant variations of performances.

Installation in hall B is also feasible, although a different installation procedure and a different detector modularity have to be studied. The construction of a detector of the same mass would require about 45 m in length. Specific studies will be produced if requested by the Committee.

8.2 R&D and Engineering

There are on-going R&D on electronics and GSC. R&D studies on electronics will be completed by the end of year 2000. R&D on GSC will be devoted to extensive tests of chambers with gases compliant with safety rules. We plan to complete these tests in 2001.

Engineering studies are needed for:

- final design of mechanical structure
- final assembly procedure
- details and construction of GSCs

- gas system
- front-end electronics
- characteristics and configuration of read-out electrodes
- final design of DAQ and trigger
- external veto counters

Part of these studies are planned to start after the approval of the Proposal. Completion of engineering is foreseen one year after approval of the Proposal. A Technical Design Report is foreseen after completion of these studies.

8.3 Construction Schedule

Starting from the approval of the Proposal, we plan the following schedule

First year
Technical design of final detector structure; definition of assembly procedure; engineering of GSC and pick-up electrodes; final design of front-end electronics, STAS, HV and LV systems.

Second year
Tenders for: iron, coil, front-end electronics, HV system, LV system, STAS, GSC and strips, gas system.
Transfer of know-how to manufacturers.
Trigger and acquisition system.

Third year
Start production of iron, chamber modules, front-end electronics. Start of construction of first module. Production of HV, LV and STAS.

Fourth year
Completion and technical run of first module.
Production and installation of external veto.
Continue production of iron, chambers, and FEE.

Fifth year
Data-taking with first module.
Start construction of second module.
Continue production of iron, chambers, and FEE.

Sixth year
Completion of second module.
Data taking with full detector.

Assuming an approval in early 2001, the first module would thus be operational by end 2004, the second module in 2006.

8.4 Infrastructures and technical support required to LNGS

We expect the following infrastructures and technical support from LNGS.

In the underground laboratory

- slow controls and emergency systems to comply with safety rules
- counting room and barracks
- electric power supplies (160 kw for coil, 200 kw for electronics) and cabling, UPS
- cooling system for coil (160 kw)
- collaboration of engineers and technicians to the design of the Slow Controls (e.g. interface of detector-specific slow-controls with safety slow-controls)

In the outside laboratory

- computing support
- offices
- support from mechanical and electronic workshop
- laboratory space (to be discussed directly with the representative of the LNGS group in the process of definition of group commitments)

8.5 Compliance with safety rules

Slow Control systems specific to compliance with safety rules will be d in collaboration with technical personnel of LNGS and third parties having experience of LNGS installations and safety.

Care will be taken to use halogen-free materials only. A non-flammable and ozone-friendly gas mixture will be used (see chapter 3).

The mechanical design of the detector structure complies with anti-seismic rules of LNGS.

Certification of conformity with safety and anty-seismic rules represent a non-negligible cost (a few percent of the cost of the structure to be certified). For a correct planning of funding requests it is important to define with the LNGS Director what degree of certification, or of favorable opinion, is required: a) for approval; b) at the Technical Design Report stage.

8.6 Cost

All prices in this section are in millions of Euro.

The price of the bulk iron is subject to important variations depending on supplier and on market conditions. Suppliers were not ready to quote official prices at this stage of the project. Thus we report for bulk iron a price corresponding to a recent transaction between a Russian supplier and a German end-manufacturer. In the following, bulk iron refers to iron plates 3.660×1.800 m^2, 80 mm thick. Costs for machining of the iron plates correspond to quotations from the Italian manufacturer Tosto.

As stated in chapter 3 alternative solutions for the configuration of read-out electrodes are being considered. A complete evaluation of costs is by now available only for the solution involving the shortest strips (never exceeding 1.8 metres) and the highest number of front-end channels. Altough a full evaluation of costs (connectors and strips) for alternative solutions is not available yet, we point out that they result in a substantial reduction in the number of front-end channels, therefore their overall price should not exceed the cost reported here.

	Cost (MEuro)
Bulk iron	7.0
Seats for spacers and holes	2.9
Structure	**9.9**
Machining of edges	1.1
Coils	0.6
Magnetization	**1.7**
External manpower	1.0
Transportation	0.5
TOTAL structure and magnet	**13.1**

Table 8.1: Cost of MONOLITH structure and magnet

	Cost (MEuro)
GSC detector plates	5.20
Strip plates and cables	1.50
Front-end electronics	5.10
STAS	0.40
TDCs	0.10
HV + LV supplies and distribution	0.80
Gas system	0.60
External manpower	0.50
Tracking and Timing system	**14.20**
DAQ	**0.40**
Trigger	**0.3**
External veto	**1.2**
TOTAL detectors, trigger and acquisition	**16.10**

Table 8.2: Cost of MONOLITH detectors trigger and acquisition system

Trigger includes cost of electronics, crates and cables. External veto includes counters, supports, cables and electronics for the complete coverage of both modules. Cost of each subsystem includes the cost of the related slow controls.

Costs of infrastructures, estimated to 1.5 MEuro, and contingency, are to be added to those reported in tables 8.1 and 8.2.

Chapter 9

The collaboration

9.1 Structure

The present structure of the MONOLITH collaboration has been set up with the aim of coordinating the R&D and the work for the Proposal. It consists in an Executive Committee (MEC) formed by A. Geiser, P. Giusti, G. Mannocchi, P. Monacelli and S. Ragazzi, with S. Ragazzi as Spokesman, G. Mannocchi as Project Leader and P. Monacelli as Contact Person with LNGS. A. Geiser is Chief-Editor of Proposal. R. Nania is Assistant Project Leader. Working groups on simulation and analysis and on physics have been convened by T. Tabarelli de Fatis and F. Ronga respectively. The decision-making body of MONOLITH is the Collaboration Board (CB). It includes one representative per Institution. The Executive Committee also acts as Editorial Board for MONOLITH publications. We are working to enlarge and strengthen the Collaboration. General Meetings and CB meetings are open to Observers of interested Institutions.

9.2 Contributions to the experiment

MONOLITH is an open collaboration; important contributions from new groups are expected. In order to be open to the preferences of potential new collaborators we did not finalize medium and long-term committments of member institutions yet. A precise planning of responsibilities will be provided as soon as the collaboration reaches a stable trim, and medium-term funding is discussed with national agencies.

Chapter 10

Conclusion

We showed the feasibility of a 34 kt magnetized iron detector which is able to

- measure the neutrino oscillation pattern in atmospheric neutrinos, therefore proving the oscillation hypothesis. Auxiliary beam measurements are being studied.
- significantly improve the measurement of Δm^2 and $\sin^2 2\theta$, covering the full allowed range independent of how it might evolve in the future.
- improve the discrimination between the $\nu_\mu - \nu_\tau$ and $\nu_\mu - \nu_s$ oscillation hypotheses. Depending on the oscillation parameters, this could be achieved through the measurement of the up/down ratio of NC-like events, through the presence or absence of a distortion of the oscillation pattern as a function of energy by matter effects, or through the (non)observation of an asymmetry in the oscillation patterns for neutrinos and antineutrinos.
- with some luck, measure charge-dependent matter effects in $\nu_\mu - \nu_e$ oscillations, and therefore the sign of Δm^2, i.e. the hierarchy of the mass pattern.
- obtain the first measurement of the cosmic ray muon energy spectrum and angular distribution around 100 TeV, and significantly improve the knowledge of muon production mechanisms and the primary spectrum and composition in the 100 TeV - 10 PeV region.

Many of these measurements are unique to this detector, and therefore complementary to other planned neutrino physics programmes. They can be achieved on a relatively short timescale, at a cost which is dominated by the required detector mass. Furthermore, a detector of this kind fits into even more ambitious long-term programmes for neutrino factories.

Acknowledgements

We wish to thank G. Battistoni and P. Lipari for very useful discussions and contributions. We are especially indebted with them for providing us with a high statistics sample of atmospheric neutrino interactions at the LNGS location. We also thank F. Pietropaolo and the groups of LAPP/Annecy, LAL/Orsay and Lyon University for their invaluable contributions to earlier stages of this work.

Appendix A

The magnetization of the iron plates

Introduction

The magnetisation of the iron plates is obtained as shown schematically in Figure 4.1. This layout of the magnetic field has been preferred to other options considered in the past (see ref. [1]), since it allows for a modular construction of the detector and to have the field lines othogonal to the CNGS beam.

The magnetic fields for several different configurations have been calculated by means of the programs of the package "POISSON SUPERFISH" [104]. C10 iron has been assumed in these calculations.

The field can be shaped, adjusting the total current, the current distribution along the coil and the coil boundaries. Of course the total currents will be suitably subdivided by means of a corresponding subdivision and seriation of the copper plates carrying them.

Each MONOLITH super-module can be magnetised independently of the other. Fig. A.1 shows the field strength in the whole MONOLITH detector (two super-modules). The field has been shaped to be highly uniform in the central region and to fill the largest possible fraction of space.

As discussed in the next section, an optimal balance between cost and MONOLITH performance is achieved at field intensities in the range 1.2-1.4 T. In this proposal we have adopted a field configuration yielding a magnetic induction of 1.33 T in the uniform region, which results in an average field of 1.28 T, while the volume over which $|H|$ exceeds 1 T corresponds to around 90% of the total.

Following the considerations of Appendix A of ref. [1], we estimate a total cost of the copper for the windings is of 560 kEuro and a power consumptions of 160 kW.

An additional cost specific to magnetization of 1 MEuro is estimated for iron machining (quotation by manufacturer Tosto).

Optimisation of the field strength

In order to optimise the field strength for MONOLITH, we have considered the following parameters:

1. Efficiency to high energy muons.

   This is defined as the fraction of outgoing muons with a track length of at least 4 m, which fire at least seven layers and have an estimated relative error on the momentum determination better than 50%. This definition reflects the selections we have adopted in the analysis of CC-interactions described in Section 4.3.2. The 4 m cut guarantees a good rejection against incoming cosmic background by TOF measurement, the request on

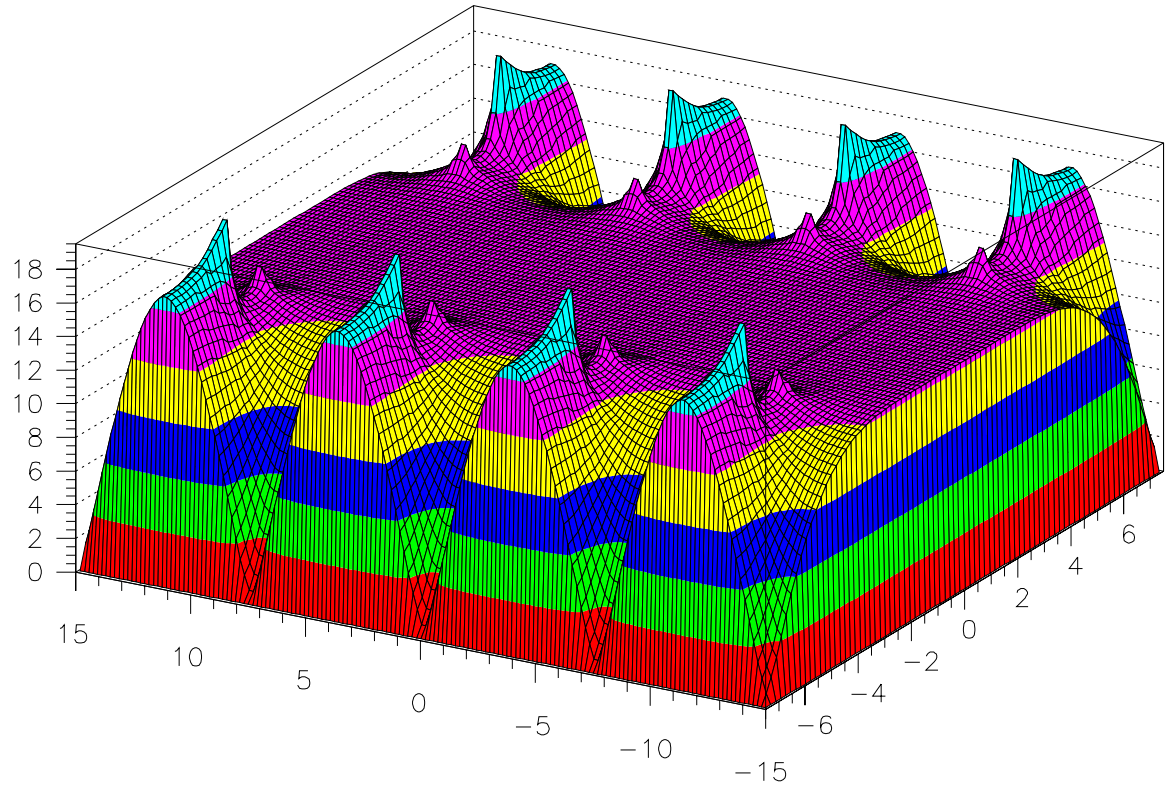

Figure A.1: YX map of the field intensity in each iron plane. The Y and X coordinates are given in meters; the magnetic induction is in kilogauss.

the muon resolution was intended to provide a good L/E resolution (no selections on the hadronic energy were made on the sample of partially contained events).

The error on the momentum has been estimated from the fitting routine. It has been verified that the pull distribution of the fit output is reasonable.

2. L/E resolution on partially contained events.

This is simply taken as the FWHM of the L/E resolution estimated from simulated events.

3. Cost and power consumption.

The study has been performed for the field configuration discussed in the previous sections. We have both used a simple parametrisation of momentum resolution in a magnetic field and results from the full simulation of the MONOLITH detector. The full simulation refers to a field of 1.33 T in the region where it is uniform (1.27 T when an average over the volume is made). Results to other field intensities have been obtained by rescaling the results at 1.3 T according to the ratio of the field intensities, which accounts for the scaling of the momentum resolution.

The two different approaches give results in substantial agreement, although the simple parametrisation (dotted line) seems slightly more optimistic, as shown in figure A.2.

It appears that at very high field both the efficiency (red line) and the L/E resolution (green line) saturates.

Indeed, there is little to be gained in efficiency by further increasing the field strength, as soon as the momentum resolution on the selected sample of muons becomes significantly better than 50%. In principle there will always be some gain by increasing the field, since the muon spectrum extends up to very high energies, however it is rapidly falling. The saturation in efficiency around 70-80% (and not around 100%) is to be ascribed to the requirement that at least seven layers be fired by the muon track.

The L/E resolution saturates between 40-50%, because at high field intensities it starts to be dominated by the resolution on the hadronic energy and on the muon direction and not by the muon momentum (unless some selection on the kinematics of the neutrino interaction is introduced, which would however reduce the overall selection efficiency).

The knee in the efficiency is at about 1 T, while in the L/E there is still a reasonable gain up to about 1.3 T, which appears to be the almost optimal field.

The blue and purple lines show the cost of the copper (in MEuro) and the power consumption (MW) as a function of the field strength, as calculated in the previous section. There are no compelling reasons to work at field intensities beyond 1.2-1.4 T, when the rapid growth of cost and consumption with the field intensity is considered and compared to the small increase in efficiency and resolution.

As discussed in section 4.3.2, the gain in acceptance at small L/E due to the magnetic field is sizeable, since it increases the MONOLITH efficiency by more than a factor two over the first semi-period of the expected oscillation signal. The cost of the magnetization, when compared to the cost of the experiment, is around 8%. The magnetization has thus an effect similar to that of doubling the total mass for 8% of the total cost.

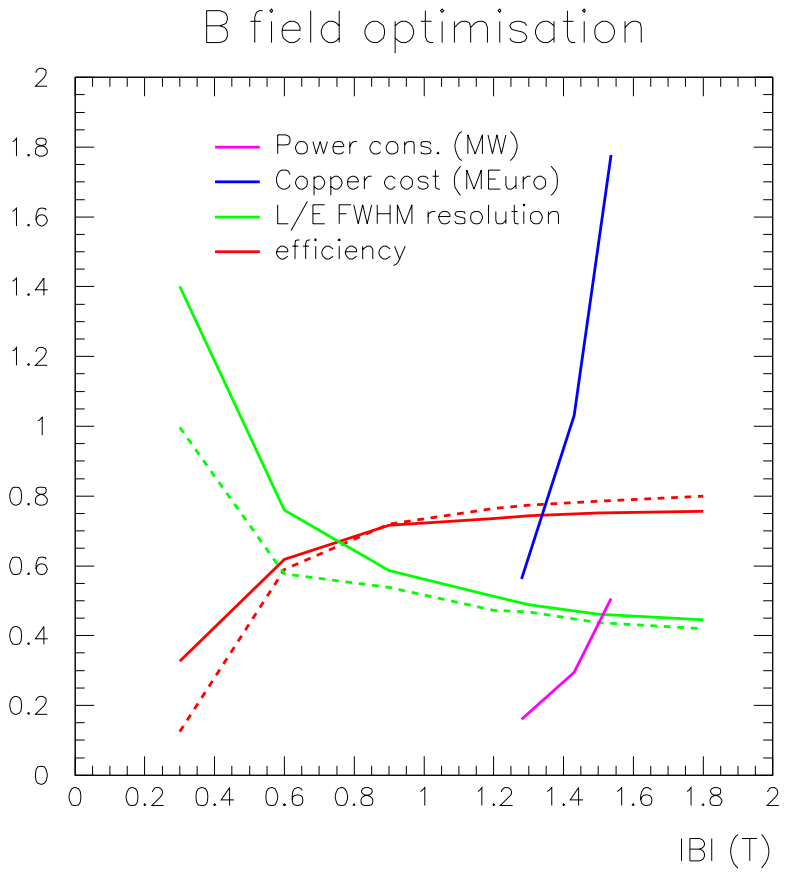

Figure A.2: L/E resolution (long falling lines) and selection efficiency (long rising lines) of ν_μ-CC events as a function of the field intensity. Dashed and continous lines refer to two different parametrisations described in the text. The power consumption (short lower line) and the cost of the copper (short upper line) are also shown.

Appendix B

A fast simulation for MONOLITH

Introduction

Unless indicated otherwise, all MONOLITH simulations presented in this document are based on a full simulation of the detector response using the GEANT package (see chapter 4). Simulations at this level are very precise, but rather demanding in CPU time. In order to be able to study certain questions with a fast feedback, a simplified fast simulation has been developed and used in parallel. It has been checked that this simulation yields results which differ only slightly from the full simulation (see fig. B.1). In a few cases where results from the full simulation were not yet available, results from the simplified simulation have been used for qualitative arguments (e.g. fig. 2.3). In this section, some details of the simplified fast simulation are described.

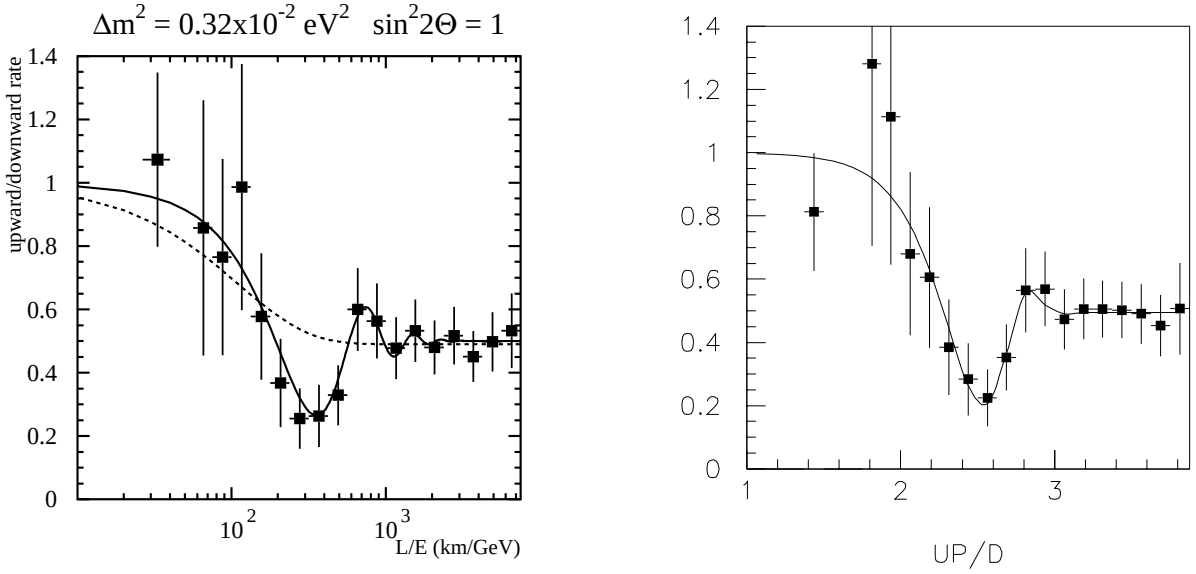

Figure B.1: *Left*: Full simulation, L/E distribution to be expected from MONOLITH for $\Delta m^2 = 3.2 \times 10^{-3}$ eV^2 (see chapter 5) compared to the best fit oscillation hypothesis (continous line), and to a parametrization corresponding to the neutrino decay model of ref. [10] (dashed line). *Right*: The same plot using the simplified fast simulation described in this section. Units are $\log_{10}$(L/E). Both plots are simulated with 20 years statistics, and error bars corresponding to 4 years.

Event generation

A simple parametrization of the main features of the Honda flux is used to generate the atmospheric neutrino flux distribution. This flux parametrization agrees with the precise flux to within a factor 2 over the full relevant angular and energy range (1 GeV - 1 TeV).

A more sophisticated parametrization of the beam flux of ref. [29] is used for CNGS beam simulations.

Only ν_μ charged current events are generated. The Bjorken x distribution is parametrized from the measured distribution at a fixed typical Q^2. A flat Bjorken y distribution is generated for neutrinos, while a distribution proportional to $(1\text{-y})^2$ is used for antineutrinos.

Detector response

The detector is described as a cube of constant average density, and constant magnetic field of 1.3 T. The event vertex is evenly distributed within this cube. Horizontal active planes with 3 cm pitch are placed every 10 cm. For the option with end caps, the first and last 2 meters of the detector are simulated with vertical active planes.

Muons are tracked as straight lines, following their initial direction. Minimum ionizing energy loss is assumed to predict the muon range. At least 7 active layers are required to be crossed to accept the event.

If the muon stops inside the detector the "measured" muon momentum is calculated from the measured range, i.e. the first and last active plane crossed. Half the distance to the next active plane is added in each case. The reconstructed momentum error is obtained from the uncertainty of the first and last point; i.e. it is assumed that the (now unknown) true vertex lies anywhere between the first recorded hit and the previous active plane (and similarly for the last point).

If the muon leaves the detector the momentum is obtained from the distance traveled in the magnetic field, accounting for the disturbance introduced by multiple scattering. To obtain the "measured" momentum, the simulated momentum is smeared (using a Gaussian in 1/p) according to the standard resolution formulae quoted for instance by the Particle Data Group. Both the magnetic field and multiple scattering terms are included, using the average density, the field strength, the reconstructed track length, and the number of hits recorded along the track. Actual bending in the magnetic field (for the number of hit calculation) and energy loss along the track are neglected.

The muon flight direction is assumed to be always correctly known, and the muon charge is assumed to be obtained from the magnetic field. A charge flip is induced if 1/p flips sign in the smearing procedure.

The "measured" hadronic energy is obtained by smearing the true hadronic energy according to the resolution function $\Delta E/E = 90\%/\sqrt{E} + 30\%$. The direction of the hadronic vector is assumed to be completely unknown.

For both muon momentum and hadronic energy, the reconstructed error is obtained by applying the reverted resolution function to the "measured" parameters.

The reconstructed neutrino flight direction is approximated by the muon direction. The reconstructed neutrino energy is obtained by summing the reconstructed muon momentum and the reconstructed hadronic energy. The distance L travelled by the neutrino is calculated from the neutrino angle assuming a production point between 5 and 20 km height in the atmosphere, and the detector positioned at sea level.

Checks

To verify the quality of this simulation many checks have been performed, including the following:

- The muon momentum resolution and the L/E resolution of the full simulation (reconstructed vs. true) is satisfactorily reproduced.
- The pull distributions (reconstructed - simulated / reconstructed error) are centered around 0 and their width is consistent with 1 (for 1/p, Ehad, Enu, and L/E).
- The expected oscillation pattern for $\Delta m^2 = 3.2 \times 10^{-3}$ eV^2, obtained with the full simulation, is correctly reproduced when the same cuts are applied (fig. B.1).

Conclusions

Although somewhat oversimplified, the fast simulation is a very useful tool to evaluate cut procedures, qualitative differences between different detector designs (variations of magnetic field, iron thickness, measurement pitch, value of magnetic field, ...) and qualitative expectations for physics results. It has been used mainly for independent checks of results already obtained by the full simulation, and to investigate further detector and physics options which were then pursued at the full simulation level. In this document, qualitative results from the fast simulation have only been used in a few cases in which the quantitative full simulation results were not yet available.

Bibliography

[1] MONOLITH Progress Report, LNGS-LOI 20/99, CERN/SPSC 99-24, August 1999.

[2] Answers of the MONOLITH collaboration to the LNGSSC questions, unpublished; http://www.mi.infn.it/ nosex/answers

[3] M. Ambrosio et al., The MONOLITH Prototype, Proceedings of the Bari RPC workshop, October 1999, ftp://netview.ba.infn.it/rpc/proceedings/gustavino.ps, submitted to Nucl. Instr. and Meth.

[4] J.N. Bahcall, P.I. Krastev, and A.Yu. Smirnov, Phys. Rev. **D 59** (1999) 046002;
N. Hata and P. Langacker, Phys. Rev. **D 56** (1997) 6107;
V. Castellani et al., Phys. Rep. **281** (1997) 309.

[5] see e.g. G.L. Fogli et al., Phys. Rev. **D 55** (1997) 4385; Phys. Rev. **D 57** (1998) 5893.

[6] Super-Kamiokande Collaboration, Y. Fukuda et al., Phys. Rev. Lett. **81** (1998) 1562;
Super-Kamiokande Collaboration, Y. Fukuda et al., Phys. Lett. **B 436** (1998) 33;
Super-Kamiokande Collaboration, Y. Fukuda et al., Phys. Lett. **B 433** (1998) 9.

[7] LSND Collaboration, C. Athanassopoulos et al., Phys. Rev. Lett. **75** (1995) 2650;
J.E. Hill, Phys. Rev. Lett. **75** (1995) 2654;
LSND Collaboration, C. Athanassopoulos et al., Phys. Rev. **C 54** (1996) 2685;
LSND Collaboration, C. Athanassopoulos et al., Phys. Rev. Lett. **77** (1996) 3082;
LSND Collaboration, C. Athanassopoulos et al., Phys. Rev. **C 58** (1998) 2489;
LSND Collaboration, C. Athanassopoulos et al., Phys. Rev. Lett. **81** (1998) 1774.

[8] see e.g. J. Primack and A. Klypin, Nucl. Phys. Proc. Suppl. **51 B** (1996) 30.

[9] see e.g. S. Pakvasa, Invited talk at 8th International Workshop on Neutrino Telescopes, Venice, Italy, 23-26 Feb 1999, hep-ph/9905426, and references therein.

[10] V. Barger et al., hep-ph/9907421;
V. Barger et al., Phys. Rev. Lett. **82** (1999) 2640.

[11] R. Barbieri et al., P. Creminelli, and A. Strumia, IFUP-TH-2000-00, hep-ph/0002199, February 2000.

[12] E. Lisi, A. Marrone, and D. Montanino, hep-ph/0002053, February 2000.

[13] G. Mannocchi et al., CERN/OPEN-98-004.

[14] A. Curioni et al., hep-ph/9805249;
M. Aglietta et al., LNGS-LOI 15/98, CERN/SPSC 98-28, SPSC/M615, Oct. 1998.

[15] NICE Letter of Intent, A. Baldini et al., LNGS-LOI 13/98 (1998);
M. Apollonio et al., CERN/SPSC 98-34, Oct. 1998.

[16] O. Yasuda, Hybrid 4-neutrino solutions to the atmospheric neutrino problem, talk at Neutrino Factory workshop NuFact'00, May 21-26, 2000.

[17] C. Albright et al., FERMILAB-FN-692, May 2000.
V. Barger et al., hep-ph/0003184, March 2000, hep-ph/0004208, April 2000.
A. Cervera et al., hep-ph/0002108, February 2000.
A. Bueno, M. Campanelli, and A. Rubbia, hep-ph/0005007, May 2000.
M. Freund, P. Huber, and M. Lindner, TUM-HEP-373/00, hep-ph/0004085, April 2000.

[18] P. Picchi and F. Pietropaolo, "Atmospheric Neutrino Oscillations Experiments", ICGF RAP. INT. 344/1997, Torino 1997, (CERN preprint SCAN–9710037).

[19] Minutes of the Joint Meeting of the CERN-SPSC and Gran Sasso Scientific Committees, CERN/SPSC 98-41

[20] CHOOZ Collaboration, M. Apollonio et al., Phys. Lett. **B 420** (1998) 397;
CHOOZ Collaboration, M. Apollonio et al., Phys. Lett. **B 466** (1999) 415.

[21] Q.Y. Liu and A.Yu. Smirnov, Nucl. Phys. **B 524** (1998) 505;
E.J. Chun, C.W. Kim, and U.W. Lee, Phys. Rev. **D 58** (1998) 093003;
A.S. Joshipura and A.Yu. Smirnov, Phys. Lett. **B 439** (1998) 103;
M. Bando and K. Yoshioka, Prog. Theor. Phys. **100** (1998) 1239;
V. Barger et al., Phys. Rev. **D 58** (1998) 093016;
E.M. Lipmanov, Phys. Lett. **B 439** (1998) 119;
J.P. Bowes and R.R. Volkas, J. Phys. **G 24** (1998) 1249;
R. Foot and R.R. Volkas, Phys. Rev. **D 52** (1995) 6595;
R. Foot, Mod. Phys. Lett. **A 9** (1994) 169;
J. Bunn, R. Foot, R.R. Volkas, Phys. Lett. **B 413** (1997) 109;
A. Geiser, Phys. Lett. **B 444** (1999) 358;
M. Kobayashi, C.S. Lim and M.M. Nojiri, Phys. Rev. Lett. **67** (1991) 1685;
C. Giunti, C.W. Kim and U.W. Lee, Phys. Rev. **D 46** (1992) 3034;
W. Krolikowski, Acta Phys. Polon. **B 30** (1999) 227;
Y. Koide and H. Fusaoka, Phys. Rev. **D 59** (1999) 053004;
Y. Koide, Phys. Rev. **D 57** (1998) 5836.

[22] KEK proposal E-362, K2K (KEK to Kamioka) neutrino oscillation experiment at KEK-PS, hep-ex/9803014.

[23] Y. Oyama (E362 (K2K) Collaboration), Proceedings of XXXV Rencontres de Moriond "Electroweak interactions and unified theories", Les Arcs, Savoie, France, March 11-18, 2000, hep-ex/0004015, and references therein.

[24] The NUMI-MINOS Project, NUMI-L-375 report (may 98); The MINOS Detectors TDR, NUMI-L-337 report (october 98 version).

[25] Soudan-2:
M. Goodman, DPF Conference, UCLA (USA), january 99,
http://www.physics.ucla.edu/dpf99/trans/2-08.pdf;
W.A. Mann, Neutrinos Telescopes, Venice (Italy), february 99,
http://axpd24.pd.infn.it/transparencies/Mann.pdf.

[26] CDHS Collaboration, F. Dydak et al., Phys. Lett. **B 134** (1984) 281;
CHARM Collaboration, F. Bergsma et al., Phys. Lett. **B 142** (1984) 103;
E776 Collaboration, L. Borodowsky et al., Phys. Rev. Lett. **68** (1992) 274;

KARMEN Collaboration, B. Zeitnitz et al., Prog. Part. Nucl. Phys.**40** (1998) 169;
Bugey Collaboration, B. Achkar et al., Nucl. Phys. **B 434** (1995) 503;
Krasnoyarsk Collaboration, G.S. Vidyakin et al., JETP Lett. **59** (1994) 237.

[27] H. Sobel (Super-Kamiokande Collaboration), Proceedings of XIX International Conference on Neutrino Physics and Astrophysics (Neutrino 2000), Sudbury, Canada, June 16-21, 2000.

[28] Kamiokande Collaboration, Y. Fukuda et al., Phys. Lett. **B 335** (1994) 237.

[29] K. Elsener (editor), CERN 98-02 and INFN/AE-98/05, May 1998;
R. Bailey et al., CERN-SL-99-034-DI, June 1999.

[30] OPERA letters of intent,
S. Shibuya et al., CERN-SPSC/97-24, SPSC/I 218, LNGS-LOI 8/97 (1997);
K. Kodama et al., CERN/SPSC 98-25, SPSC/M612, LNGS-LOI 8/97, Add. 1.

[31] CHORUS Collaboration, E. Eskut et al., Phys. Lett. **B 424** (1998) 202;
CHORUS Collaboration, E. Eskut et al., Phys. Lett. **B 434** (1998) 205.

[32] ICARUS Collaboration, P. Benetti et al., Nucl. Instr. Methods **A 327** (1993) 327; **A 332** (1993) 332; P. Cennini et al., Nucl. Instr. Methods **A 333** (1993) 567;
A 345 (1994) 230; **A 355** (1995) 355;
ICARUS-CERN-Milano Collaboration, CERN/SPSLC 96-58, SPSLC/P 304, December 1996.

[33] NOMAD Collaboration, J. Altegoer et al., Phys. Lett. **B 431** (1998) 219;
NOMAD Collaboration, P. Astier et al., Phys. Lett. **B 453** (1999) 169.

[34] K. Winter et al., *Expression of Interest to participate in the Study, Construction and Use of a Neutrino Facility at the Gran Sasso Laboratory*, CERN/SPSC 98-36; SPSC-M623.

[35] S. Wojcicki, Proceedings of Neutrino '98, Takayama, Japan, June 4-9, 1998.

[36] Particle Data Group, Eur. Phys. Journ. **C 3** (1998) 1.

[37] R. Foot, R.R. Volkas, and O. Yasuda, Phys. Rev. **D58** (1998) 013006;
M.C. Gonzalez-Garcia et al., Nucl. Phys. **B 543** (1999) 3.

[38] C. Giunti, Hybrid 4-neutrino solutions to the solar neutrino problem, talk at Neutrino Factory workshop NuFact'00, May 21-26, 2000.

[39] S.M. Bilenky et al., hep-ph/9906251.

[40] A. Geiser, Eur. Phys. J. **C 7** (1999) 437.

[41] C. Walter (Super-Kamiokande Collaboration) Proceedings of EPS '99, Tampere, Finland, 15-21 July 1999.

[42] F. Vissani and A. Yu. Smirnov, Phys. Lett. B432 (1998) 376.

[43] J.W. Flanagan, J.G. Learned, and S. Pakvasa, Phys. Rev. **D 57** (1998) 2649;
J.G. Learned, S. Pakvasa, and J.L. Stone, Phys. Lett. **B 435** (1998) 131.

[44] L. Wolfenstein, Phys. Rev. **D 17** (1978) 2369; Phys. Rev. **D 20** (1979) 2634.

[45] P. Lipari and L. Lusignoli, Phys. Rev. D, 58 (1998) 073005.

[46] F. Ronga for the MACRO Collaboration, hep-ex/9905025.

[47] S.P. Mikheyev and A.Y. Smirnov, Sov. J. Nucl. Phys. **42** (1985) 913; Nuovo Cimento **9C** (1986) 17.

[48] Q.Y. Liu, S.P. Mikheyev, and A.Y. Smirnov, Phys. Lett. **B 440** (1998) 319;
M.V. Chizhov, S.T. Petcov, SISSA-28-99-EP and hep-ph/9903424.

[49] A. Geiser, Future Atmospheric Neutrino Detectors, Proceedings of XIX International Conference on Neutrino Physics and Astrophysics (Neutrino 2000), Sudbury, Canada, June 16-21, 2000.

[50] P.F. Harrison, D.H. Perkins, and W.G. Scott, Phys. Lett. **B 458** (1999) 79;
and W.G. Scott, private communication

[51] G. Collazuol et al., presented at NOW98 workshop, Amsterdam, 7-9 September 1998, CERN OPEN-98-032.

[52] D. Cline and D. Neuffer, AIP Conf. Proc. **68** (1980) 846; reproduced in AIP Conf. Proc. **352** (1996) 10;
S. Geer, Phys. Rev. **D 57** (1998) 6989; Erratum-ibid. D 59 (1999) 039903.

[53] J.J. Gomez-Cadenas and A. Cervera-Villanueva, talks given at ν-Fact '99, Lyon, 5-9 July 1999.

[54] A. De Rujula, M.B. Gavela and P. Hernandez, Nucl. Phys. **B 547** (1999) 21.

[55] V. Barger, S. Geer and K. Whisnant, hep-ph/9906487.

[56] S.I. Nikolsky, Nucl. Phys. B (Proc.Suppl.) **39A** (1995) 228.

[57] A.A. Petrukhin, talk at the XIth Rencontres de Blois "Frontiers of Matter", Blois, France, June 28-July 3, 1999, and preprint MEPhI, No.006-99, 1999.

[58] T.Matano et al. Proc. Int. Conf. on Cosmic Rays, London, v.2 (1965) 1045.

[59] N.P.Il'ina et al. Proc 24th ICRC, Roma, v.1 (1995) 524.

[60] M.Ambrosio et al. Phys. Rev. **D 56** (1997) 1407, 1418.

[61] G. Bencivenni et al., Nucl. Instr. and Method **A 300** (1991) 572.

[62] G. Bencivenni et al., Nucl. Instr. and Method **A 315** (1992) 507.

[63] M. De Deo et al., LNGS -95/39, June 1995.

[64] G. Bencivenni et al., Nucl. Instr. and Method **A 345** (1994) 456.

[65] G. Bencivenni et al., Nucl. Instr. and Method **A 332** (1993) 368.

[66] C. Gustavino et al., INFN/TC-99/14,Nucl. Instr. and Method. accepted

[67] K. Abe et al.,"Glass RPC Module for Belle Endcap KL/mu Detector", Proc. of IV Int.Workshop on Resistive Plate Chamber and Related Detectors, Napoli, Oct 15-16 1997. Ed. Sergio Ratti, Riccardo de Asmundis.
A. Abashian et al.,Nucl. Instr. and Meth. **A 449** (2000) 112-124.
K. Abe et al. Nucl. Instr. and Meth. **A** (2000), accepted.

[68] C.Gustavino et al., *Proc. of 8th Pisa Meeting on Advanced Detectors*, La Biodola, Isola d'Elba, 2000, in press; *Nucl. Instr. and Meth*,accepted.

[69] A.Candela et al,"Behaviour of the Y-coordinate read out system for the MACRO Attico", MACRO int.MEMO 14/29.

[70] M.D'Incecco et al:"Description of the Charge and Time card for Glass RPC detectors", MONOLITH 004/00, unpublished.

[71] S.Blo, G.Lamperti, 3M Italia S.p.A. Via S.Bovio 3, Segrate (MI), Italy. E-mails:sblo1@mmm.com, glamperti1@mmm.com.

[72] I216/P311 Proposal, M. Guler at al., CERN-SPSC/99-26, SPSC/P311, August 1999.

[73] GEANT Detector Description and Simulation Tools, CERN Program Library, Long Writeup W5013.

[74] V. Agrawal, T.K. Gaisser, P. Lipari and T. Stanev, Phys. Rev. **D 53** (1996) 1314.

[75] M. Gluck, E. Reya and A. Vogt, Z. Phys. **C 67** (1995) 433.

[76] P. Lipari, M. Lusignoli and F. Sartogo, Phys. Rev. Lett. **74** (1995) 4384.

[77] T.K. Gaisser and T. Stanev, astro/ph-9708146.

[78] J. Thomas, A. Para and D. Tovee, NuMI-L-301

[79] M. Honda et al., Phys. ReV **D52** (1995) 4985.

[80] G. Battistoni et al., Astroparticle Phys. **12**, 315 (2000).

[81] Y. Tserkonvyak at al., hep-ph/9907450.

[82] P. Lipari, hep-ph/0002282.

[83] P. Lipari, T. K. Gaisser and T. Stanev, Phys. Rev. **D 58** (1998) 073003.

[84] G. Battistoni and P. Lipari, hep-ph/9807475.

[85] A. Curioni and T. Tabarelli de Fatis, *Geometrical sampling of L/E distributions*, NOSEX-003/98, unpublished.

[86] T. Tabarelli de Fatis, *Oscillations and experimental resolution*, NOSEX-002/98, unpublished.

[87] The MACRO collaboration, Phys. Lett. **B249** (1990) 149.

[88] The LVD collaboration, Phys. Rev. **D58** (1998) 092005

[89] P. Antonioli et al., Astroparticle Phys. **7** (1997) 357.

[90] MINUIT, Function Minimization and Error Analysis, CERN Program Library Long Writeup D506.

[91] See for example: W.T. Eadje et al., *Statistical Methods in Experimental Physics*, North-Holland Publishing Company, 1971, p. 243

[92] P. Jain, J. P. Ralston and G. M. Frichter, hep-ph 9902206, to appear in Astroparticle Phys.

[93] F. Ronga and F. Terranova, *The use of Earth-induced matter effects to discriminate between ν_μ-ν_τ and ν_μ-ν_s oscillations in MONOLITH*, MONOLITH-003/00, unpublished.

[94] P. Antonioli et al., *First Study of MONOLITH performance on CNGS beam*, MONOLITH 05/2000, unpublished

[95] V. Innocente et al., "GEANE : average tracking and error propagation package" in Proceedings of Workshop on detector and event simulation in high energy physics : Monte Carlo '91 Amsterdam, Netherlands ; 8 - 12 Apr 1991, edited by K. Bos and B. van Eijl, NIKHEF, Amsterdam, (1991) 58-78.

[96] CCFR Collaboration, K.S. McFarland et al., Eur. Phys. J. **C 1** (1998) 509;
CCFR Collaboration, C.G. Arroyo et al., Phys. Rev. Lett. **72** (1994) 3452;
CCFR Collaboration, P.G. Reutens et al., Z. Phys. **C 45** (1990) 539;
CDHS Collaboration, A. Blondel et al., Z. Phys. **C 45** (1990) 361;
CHARM Collaboration, J.V. Allaby et al., Z. Phys. **C 36** (1987) 611.

[97] I.S. Alekseev, G.T. Zatsepin. Proc. Int. Conf. on Cosmic Rays, Moscow, v.1 (1960) 324.

[98] R.P. Kokoulin, A.A. Petrukhin, Nucl. Instr. and Meth. **A 263** (1988) 468.

[99] R.P. Kokoulin, A.A. Petrukhin, Sov. Journ. Part. and Nucl. **21** (1990) 332.

[100] C. Castagnoli et al. Astroparticle Phys. **6** (1997) 187.

[101] R.P. Kokoulin et al. Proc. 26th ICRC, Salt Lake City, v.2 (1999) 28.

[102] O.C. Allkofer et al., Nucl. Phys. **B 259** (1985) 1.

[103] S. Matsuno et al., Phys. Rev. **D 29** (1984) 1.

[104] J. H. Billen, L. M. Young, *POISSON SUPERFISH*, LA-UR-96-1834, Los Alamos National Laboratory, Revised November 14, 1998.